Division of Pharmaceutical Chemistry and Technology
Faculty of Pharmacy
University of Helsinki
Finland

Porous Silicon-Based On-Demand Nanohybrids for Biomedical Applications

by

Zehua Liu

DOCTORAL DISSERTATION

To be presented for public examination with the permission of the Faculty of Pharmacy of the University of Helsinki, in Sali 235, Infokeskus, on the 19th of July, 2019 at 12 o'clock

Helsinki 2019

Supervisors

Associate Professor Hélder A. Santos
Drug Research Program
Division of Pharmaceutical Chemistry and Technology
Faculty of Pharmacy
University of Helsinki
Finland

Associate Professor Hongbo Zhang
Department of Pharmaceutical Sciences Laboratory
Faculty of Science and Engineering
Åbo Akademi University
Finland

Professor Jouni Hirvonen
Drug Research Program
Division of Pharmaceutical Chemistry and Technology
Faculty of Pharmacy
University of Helsinki
Finland

Reviewers

Professor Molly Stevens
Department of Materials
Imperial College of London
U.K.

Professor Ji-Ho Park
Department of Bio and Brain Engineering
Korea Advanced Institute of Science and Technology
Republic of Korea

Opponent

Associate Professor Ester Segal
Department of Biotechnology and Food Engineering
Technion - Israel Institute of Technology
Israel

Faculty of Pharmacy, Doctoral Programme in Drug Research (DPDR)

ISBN 978-951-51-5290-9 (Paperback), 978-951-51-5291-6 (PDF)
ISSN 2342-3161 (Print), 2342-317X (Online)

Helsinki University Printing House
Helsinki 2019

The Faculty of Pharmacy uses the Urkund system (plagiarism recognition) to examine all doctoral dissertations.

Abstract

Considerable efforts have been made to fabricate nano-sized drug delivery systems (DDS) with unique and advanced features in comparison to conventional DDS. Yet, challenges still lay ahead requesting for more controllable, even on-demand drug release profiles from the DDS. Moreover, the emerging concept of personalized treatment further urges the combining of therapy and imaging regimes into a single nanocarrier.

Among all the nanomaterials studied so far, porous silicon (PSi) draws increasing interest for constructing DDS due to its good biocompatibility, non-immunogenicity, large pore size/surface area and easily changeable surface properties. Herein, the aim of this thesis was to explore PSi-based DDS for multiple biomedical applications, which were designed and synthesized with specific on-demand features. Moreover, simultaneous incorporation of imaging modalities and drugs enables real-time visualization of drug release and/or cellular/tissue level disease condition, which are expected to be beneficial for personalized treatment regime.

First, the potential of PSi nanoparticles for hydrophilic drug loading and on-demand release were evaluated by adapting a dynamic non-covalent bonding method. Different ligands were synthesized and applied for modifying the PSi, and the hydrophilic anti-cancer drug doxorubicin (DOX) was sequentially loaded into the fabricated DDS for pH-responsive release profiles. Meanwhile, the fluorescence spectrum of DOX can be dynamically shifted or quenched, depending on the loading and releasing process, thus facilitating the *in situ* visualization of the drug releasing process.

For hydrophobic drugs, a physical encapsulation method was applied to seal the pores of the PSi by a polymeric matrix. Microfluidic-assisted nanoprecipitation method was applied to synthesize batches of nanohybrids with identical PSi-core/polymer-shell structures, and the release behavior was feasibly tailored by the degradation behavior of the outer polymeric matrix. The first trial was set to fabricate a core/shell nanohybrid, with PSi and gold nanoparticles co-encapsulated in a pH-responsive polymer to simultaneously deliver hydrophobic drug and increase the computed tomography signal for acute liver failure theranostics. The newly established single-step co-encapsulation of different particles endowed a system with multi-functionalities, and the polymeric shell precisely tailored the drug release behavior in a pH-dependent manner. Similarly, an acid/oxidation dual-responsive polymer was designed and further applied in encapsulating atorvastatin-loaded PSi nanoparticles. The meticulously designed system not only obtained a dynamic drug release behavior, but also showed an orchestrated cascade that facilitated bio-mimetic diabetic wound healing.

To better elucidate the biocompatibility of PSi for DDS fabrication, the biological effects and immunogenicity of different PSi nanoparticles were evaluated at pre-existing lesion sites, which provided insights for further applications of PSi in DDS fabrication.

In conclusion, multiple PSi-based nanohybrids with different on-demand responses were fabricated and applied as DDSs for different diseases. The newly developed nanosystems tailored drug release and obtained multiple modalities, ranging from real-time bio-imaging to bio-mimetic/bio-response alteration, as such, represent promising platforms for future therapy regimes.

Acknowledgement

This study has been performed at the Division of Pharmaceutical Chemistry and Technology, Faculty of Pharmacy, University of Helsinki, during the years 2015–2019. This adventure will be an infinite gift in my life, and I want to thank all the people along by my side in this journey.

First and foremost, I would like to express my deepest gratitude to Prof. Hélder A. Santos, a man who is already beyond a supervisor to me, a man who taught me the meaning of pursuing eternal knowledge, a man who ignited my passion, a man who enlightened me to find opportunity from uncertainty and a man who was, and will always be my mentor in my life.

I am extremely grateful to my supervisor, Prof. Jouni Hirvonen, for giving me the opportunity to perform my doctoral studies in this excellent group. Your supervision, patience, and positive attitude towards research have made Finland a warm place.

I also send my most sincere gratitude to Prof. Hongbo Zhang, whose profound thoughts ripens my ideas into systematic projects. His guidance was not from words but from his striving, his humility and unyielding spirit in daily life. As my co-supervisor, he treated me and called me as a brother, but still, he is a mentor to me cause we don`t follow titles, we follow the shining souls.

I would also like to express my greatest gratitude to Prof. Xianming Deng, a scientist, an intelligentsia, a selfless researcher, a noble leader and a real gentleman. Your instructions and guidance deepened my thoughts and will always display their golden value in my future.

I am very grateful to all my co-authors for their invaluable scientific contributions and fruitful discussions. I would especially like to thank M.Sc Yunzhan Li, Dr. Wei Li, Dr. Agnė Janonienė, Dr. Ermei Mäkilä, M.Sc. Patricia Figueiredo, Dr. Dongfei Liu, Dr. Li Li, M.Sc. Wenhua Lian, Prof. Jari Yli-Kauhaluoma, Prof. Marianna Kemell, Prof. Vilma Petrikaite, Prof. Jarno Salonen for their collaborations.

Xinyuan Wang, Yunzhan Li and Lei Deng, my buddies, my mates, my brothers. You are thousands miles away from me, but I know you will always be there for me.

I would also like to thank Professor Molly Stevens and Professor Ji-Ho Park, who reviewed this work and presented constructive comments and suggestions for how to improve the dissertation.

I am very grateful to my opponent, Pro. Ester Segal, who kindly accepted our invitation to save my defense from uncertainty. I am really looking forward to the discussion.

Financial support from the Chinese Scholarship Council is acknowledged.

I want to say to my mom and my sister, I love you. Forgive me as I never said that to you, but you know how much I love you, and whatever comes, I will always love you. Time changed, life changed, but my love to you will never change.

Finally, and most importantly, I would like to dedicate this dissertation to my wife. You are like a shining star that guides my life through the dark unknown, you endow a meaning to my life, and your support can burst with the gold of the dawn in my hardest time, and make everything worth it. Your smile, your encouragement, your whisper, your grace, make all these years like a colorful dream, cause when I wake up, I know you will be there, by my side.

Let me not shame thee, father, and may thy soul rest in peace.

Contents

List of original publications

This dissertation is based on the following publications, which are referred to in the text by their respective roman numerals (**I**–**V**):

I **Liu Z.**, Balasubramanian V., Bhat C., Vahermo M., Mäkilä M., Kemell M., Fontana F., Janoniene A., Petrikaite V., Salonen J., Yli-Kauhaluoma J., Hirvonen J., Zhang H., Santos H.A., 2017. Quercetin-based modified porous silicon nanoparticles for enhanced inhibition of doxorubicin-resistant cancer cells. *Advanced Healthcare Materials*, 6: 1601009-1601019.

II Janoniene A., **Liu Z.**, Baranauskiene L., Mäkilä E., Ma M., Salonen J., Hirvonen J., Zhang H., Petrikaite V., Santos H.A., 2017. A versatile carbonic anhydrase IX targeting ligand functionalized porous silicon nanoplatform for dual hypoxia cancer therapy and imaging. *ACS Applied Materials & Interfaces*, 9: 13976-13987.

III **Liu Z.**, Li Y., Li W., Xiao C., Liu D., Dong C., Zhang M., Mäkilä E., Kemell M., Salonen J., Hirvonen J., Zhang H., Zhou D., Deng X., Santos H.A., 2018. Multifunctional nanohybrid based on porous silicon nanoparticles, gold nanoparticles, and acetalated dextran for liver regeneration and acute liver failure theranostics. *Advanced Materials*, 30: 1703393-1703402.

IV **Liu Z.**, Li Y., Li W., Lian W., Kemell M., Hietala S., Figueiredo P., Li L., Mäkilä E., Ma M., Salonen J., Hirvonen J., Liu D., Zhang H., Deng X., Santos H.A., 2019. Close-loop dynamic nanohybrids on collagen-ark with in-situ gelling transformation capability for bio-mimetically stage specific diabetic wound healing. *Materials Horizons*, 6: 385-393.

V Li Y., **Liu Z.**, Li L., Lian W., He Y., Khalil E., Mäkilä E., Zhang W., Torrieri G., Liu X., Su J., Xiu Y., Fontana F., Airaksinen A., Salonen J., Hirvonen J., Liu W., Zhang H., Santos H.A., Deng X., Specific immunogenicity of porous silicon nanoparticles in pathological conditions is primed by protein corona composition. Submitted

 In publication **II**, **IV**, the first two authors contributed equally to the work. In publication **III, V**, the first three authors contributed equally to the work.

Abbreviations

AcDEX	Acetalated dextran
ALF	Acute liver failure
ALI	Acute liver inflammation
ALT	Alanine aminotransferase
AmQu	3-aminopropoxy-linked quercetin
APAP	Acetaminophen
APC	Antigen presenting cells
APTES	(3-Aminopropyl)-triethoxysilane
AST	Aspartate aminotransferase
AST/ALT	Ratio between AST and ALT
ATR	Attenuated total reflectance
ATO	Atorvastatin
Boc	t-Butyloxy carbonyl
BSA	Bovine serum albumin
CA	Carbonic anhydrases
CCL-2	Chemokine (C-C motif) ligand 2
CDI	N,N'-Carbonyldiimidazole
CF	Free ATO, DFO and GOx embedded in collagen patch
CFD	Computational fluidic dynamics
CP	Blank PSi@POD embedded in collagen patch
CT	Computed tomography
CXCR-1	Chemokine (C-X-C motif) receptor 1
DAu	Spermine AcDEX gold nanoparticles
DAVID	Database for annotation, visualization and integrated discovery
DCFH-DA	Dichlorodihydrofluorescein diacetate
DDS	Drug delivery systems
DFO	Deferoxamine
DLS	Dynamic light scattering
DMEM	Dulbecco's modified Eagle's medium
DMF	N,N-dimethylformamide
DMSO	Dimethyl sulfoxide
DOX	Doxorubicin
DOX@FAP	DOX loaded in FAP
DOX/MCF-7^{R}	DOX-resistance human breast cancer cell line MCF-7
DOX@VD-PSi	DOX loaded VD-PSi
DPSi	Spermine AcDEX modified PSi nanoparticles
DPSi/DAu@AcDEX	PSi/Au co-encapsulated in AcDEX matrix
EDC	N-(3-dimethylaminopropyl)-N'-ethylcarbodiimide hydrochloride
EDX	Energy dispersive X-ray spectroscopy
ELISA	Enzyme-linked immunosorbent assay

FAP	Fe^{3+}-AmQu-UnTHCPSi
FBS	Fetal bovine serum
FRET	Fluorescence resonance energy transfer
FTIR	Fourier transform infrared spectroscopy
GO	Gene ontology
GOx	Glucose oxidase
GSH	Glutathione
HBSS	Hank's balanced salt solution
HEPES	4-(2-hydroxyethyl)-1-piperazineethanesulfonic acid
Hif-1α	Hypoxia induced factor–1α
HU	Hounsfield unit
H&E	Hematoxylin-eosin
IκBα	NF-κB inhibitor α
iTRAQ	Isobaric tags for relative and absolute quantification
LPS	Lipopolysaccaride
MOB	Mps-one binder protein
MPS	Monocyte phagocytic system
MP–AES	Microwave plasma–atomic emission spectrometer
MP@DPSi/DAu@AcDEX	XMU-MP-1 loaded PSi/Au co-encapsulated in AcDEX matrix
MST	Mammalian sterile 20-like kinase
MVD	Microvessel density
NADPH	Nicotinamide adenine dinucleotide phosphate
NF-κB	Nuclear factor κB
NHS	N-hydroxysuccinimide
NPs	Nanoparticles
ODEX	Oxidized dextran
PA	ATO/GOx loaded PSi@POD embedded in collagen patch
PAD	ATO/DFO/GOx loaded PSi@POD embedded in collagen patch
PAE	Phenylboronic acid ester
PBA	Phenylboronic acid
PBS	Phosphate-buffered saline
PDMS	Polydimethylsiloxane
Pe	Peclet number
PEG	Polyethylene glycol
PET	Positron emission computed tomography
PLGA	Poly(lactic-co-glycolic acid)
POD	4-(Hydroxymethyl)-phenylboronic acid pinacol ester modified ODEX
PSi	Porous silicon
PSi@POD	PSi-encapsulated POD nanohybrids
qPCR	Real-time quantitative polymerase chain reaction
QSSQ	Disulfide-bridged quercetin
Re	Reynolds number

ROS	Reactive oxygen species
SDS-PAGE	Sodium dodecyl sulfate polyacrylamide gel electrophoresis
SEM	Scanning electron microscopy
SIN-1	3-Morpholinosydnonimine
STZ	Streptozotocin
TCPSi (TC)	Thermally carbonized porous silicon
THCPSi	Thermally hydrocarbonized porous silicon
TOPSi (TO)	Thermally oxidized porous silicon
TEM	Transmission electron microscopy
TNF-α	Tumor necrosis factor-α
TUNEL	Transferase-mediated deoxyuridine triphosphate-biotin nick end labelling
UnTHCPSi (Un)	Undecylenic acid functionalized THCPSi
VEGF	Vascular endothelial growth factor
VD11-4-2	2-(Cyclooctylamino)-3,5,6-trifluoro-4-[(2-hydroxyethyl)thio]benzenesulfonamide
VD-PSi	VD11-4-2 modified PSi nanoparticles
WBC	White blood cells
XMU-MP-1	2,4-((5,10-Dimethyl-6-oxo-6,10-dihydro-5H-pyrimido[5,4-b] thieno[3,2-e][1,4]diazepin-2-yl)amino)benzenesulfonamide
YAP	Yes-asscioated protein
ζ-potential	Zeta-potential

1 Introduction

Meticulously engineered drug delivery systems (DDS) are pivotal for the targeted delivery and/or controlled release of therapeutic agents.[1] Comparing to new pharmaceutical agents development, the combination of a "smart" delivery system with tailored spatiotemporal release behavior is equally indispensable to the development of new pharmaceutical agents, and has been pursued vigorously for the past decades.[2, 3] The application of biomaterials to fabricate DDS is ubiquitous in the practice of medicine, yet the intrinsic limits of conventional DDS, such as unregulated drug bio-distribution, detained hydrophobic drug diffusion/release and unfavourable release profile,[4, 5] prompt the development of new generation DDS for more effective and safer treatments.

Nanoparticles (NPs) based DDS have emerged as suitable drug delivery vehicles for overcoming pharmacokinetic limitations associated with conventional drug formulations by showing advantageous in solubilizing hydrophobic therapeutic cargos and further enhancing their diffusion behavior, and prolonging the circulation lifetimes of drugs in the bloodstream.[5-7] Due to the large surface-to-volume ratio, nanoparticles can be feasibly surface-modified with proper ligands to obtain multi-functionalities. Therefore, the concept of "one particle performs multiple functions" can be concurrently achieved.[8, 9] In addition, unique nano-scale size endows the DDS with the ability to increases the DDS accumulation at specific sites, such as tumor or inflammation spots, while promoting intracellular penetration.[10-12]

Among the biomaterials studied so far, porous silicon (PSi) NPs have attracted increasing attention for potential biomedical applications, especially as advanced DDSs.[13, 14] Their pore size (~10 nm) makes PSi very flexible in loading different kind of cargos, ranging from small molecule drugs, proteins, peptides, RNA to other NPs.[15, 16] The versatile surface chemistry and high surface area (up to 1000 m^2/g) enables PSi to be feasibly surface functionalized for multiple purposes. Moreover, PSi has good biocompatibility and biodegradability; it is degraded into non-toxic orthosilicic acid *in vivo*, and the degradation rate can be feasibly tuned by altering the overall size, porosity, pore size and surface functionalization.[17, 18] All these features render PSi NPs a perfect candidate for fabricating DDSs.

However, due to the freely accessible pores of PSi, the loaded drugs can be disrupted by body fluids, leading to burst release and/or inactivation of the loaded cargos.[19, 20] Moreover, despite previous investigations, precise control of drug release at localized sites of interest remains a critical challenge.[21-23] Proper methods should be considered to fabricate PSi-based DDS that can recapitulate the heterogenous native microenvironment and further release drug(s) at desired sites to increase therapeutic efficacy.

Spurred by recent progress in materials chemistry, one alternative that is gaining attention in DDS construction involves on-demand processes.[24, 25] On-demand, or stimuli-responsive drug delivery systems can recognize their surrounding microenvironments, further undertake structural or functional alteration, mimic the responsiveness of living organisms or release the loaded cargo in the lesion sites.[9, 26, 27] Yet, different strategies should be prudently selected for drugs with different physiochemical properties and different biomedical applications.

For hydrophilic drugs, a facile method to effectively control the release kinetics is by chemical conjugation, whereas the inherent defects of covalent bonding, ranging from organic solvents introduction, deactivation of the cargos, to unfavourable selectivity of the reaction site, may perturb the envisioned design.[28, 29] Next-generation DDS fabrication is based on the introduction of cleavable motifs by reversible non-covalent interaction that exploits metal chelation, coordination, hydrogen bond, π–π stacking, hydrophobic interaction and/or Van der Waals interactions.[30-35] The cleavable moieties can be triggered by specific stimuli, therefore achieving the preferred release performance.

For hydrophobic drugs, the interaction between PSi with the hydrophobic surface may render the drugs to reside in the pores of PSi,[36] while the following surface encapsulation can effectively seal the pores to prevent uncontrollable release and payload inactivation when interacting with body fluids.[37] Therefore, the judicious choice of encapsulating materials is one of the key preconditions for successful construction of DDS, and is highly implicated with different biomedical applications, thus needing further investigation. Meanwhile, an advanced encapsulating methodology is another pivotal factor impinging on successful and efficient DDS fabrication. Microfluidics has had a revolutionary impact on a wide range of applications, such as colloidal particle fabrication, chemical synthesis, tissue engineering and biological simulation/analysis.[38-41] The specific benefits of microfluidic-assisted encapsulation arise from fluid flow manipulation, which confers to the control over shape, size, geometry, the loading of different cargos, and release profiles of the DDS in a tailored manner.[42, 43] Therefore, this platform can be leveraged to create a series of advanced DDS, such as single, double and higher-ordered emulsions, microcapsules, NPs/nanohybrids and other colloidal DDS.[44, 45] As such, microfluidics platform provides a diverse toolbox that can help address unmet biomedical needs.

Upon such consideration, in this dissertation, we focused on the fabrication and characterization of multiple therapeutics loaded PSi-based DDS with on-demand control over the drug release, and evaluating their different biomedical applications. Both hydrophilic and hydrophobic drugs were applied in the studies and different strategies were utilized, corresponding to the physiochemical properties of the loaded cargos. Stimuli responsive dynamic non-covalent bonds were leveraged for controlling the release of hydrophilic drugs, which were endowed by the design and/or application of different ligands. For hydrophobic drugs, microfluidic-assisted nano-encapsulation was carried out to fabricate PSi-based nanohybrids (drug loaded PSi as core and functional polymer matrix as shell) to avoid the premature release of payloads, allowing the on-demand release of the cargos at desired times and sites. Multi-functionalities, such as drug release tracking or bio-imaging, were synchronously achieved to further explore the cutting-edge functions of nanotechnology. Most importantly, the biocompatibility and immunogenicity of PSi under pathological condition were investigated to better evaluate the biosafety of the DDS, offering significant insights for further clinical translation.

2 Review of the literature

2.1 Multifunctional on-demand DDS

Advanced NPs-based DDS have drawn tremendous attentions in recent years. The interest was initiated by the enhanced accumulation of NPs at specific sites, such as tumors or inflamed tissues.[46-48] In addition, the intrinsic nature of nano-sized carriers can solve some of the refractory drawbacks of conventional DDS, such as enhancing the pharmaceutical properties of the drugs, *e.g.* stability, solubility and longevity, while providing simultaneous imaging or diagnosing capabilities and real-time visualization of drug delivery sites.[49-52] However, despite the development of a broad range of NPs, including liposomes, polymer NPs, micelles, dendrimers, origami DNA, drug crystals and inorganic NPs, the overall picture of the further applications of NPs-based DDS is still blurred by many challenges inherently linked to the complexity of disease pathophysiology and a series of physiological barriers.[53-56] Consequently, the difficulty in controlling drug release from NPs further motivates the rational design and architecture fabrication of nanomedicine to overcome the challenges.[57, 58]

A fundamental goal for nanomedicine is to prevent the payloads from any passive leakage in the delivery process, but also to readily unload the cargos in a controlled manner once arriving at the target sites.[27] To achieve this spatiotemporal controlled release, on-demand or stimuli-responsive NPs have been proposed for various therapeutic cargos.[59, 60] These dynamic NPs are capable of recognizing, adapting and responding to a variety of stimuli, followed by morphology transformation or degradation of the NPs to induce the release of drugs.

Furthermore, to explore the multi-functionalities of the on-demand DDS, one cannot discard the possibility of simultaneously applying the DDS for imaging or diagnosis.[61, 62] The prudent choice of loaded cargo or surface modification may provide theranostic applications, including bio-imaging facilitated diagnosis, cellular imaging, and real-time drug release monitoring.

2.1.1 On-demand DDS for controlled release

Two categories of stimuli triggered drug release profiles can be briefly divided depending on the stimuli source. Endogenous stimuli triggered on-demand DDS refers to trigger by abnormal or unique physiochemical microenvironments at the target sites,[63-65] whereas exogenous stimuli triggered on-demand DDS leverages externally applied stimuli, such as light, temperature, magnetic field and/or ultrasound to initiate the dynamic transformation of the NPs.[64, 66] In the interest of brevity, this thesis does not included exogenous stimuli triggered on-demand DDS. Instead, the focus is on design strategies and exploiting the subtle environmental changes associated with pathological situations.

Aberrant physiological characters within the diseased tissue or specific cells are ubiquitous, and can therefore be exploited to fabricate on-demand DDS. Implementation of a viable system is vastly dependent on the judicious choice of applied stimuli and methodologies, which are implicated with different biomedical applications and

physiological properties of the loaded drugs. The following sections will briefly review the commonly used on-demand NPs constructions and their potential biomedical applications.

2.1.1.1 pH-Responsive DDS

pH variation widely exists throughout the human body (**Figure 1**). This phenomenon is observed on the organ level (*e.g.*, altered pH-values in gastrointestinal tract and vaginal cavity), tissue level (*e.g.*, decreased pH-values within the extracellular matrix (ECM) of the tumor) and cellular level (*e.g.*, acidic environments within endosomal/lysosomal system). As such, pH may play a salient role in the on-demand DDS design.

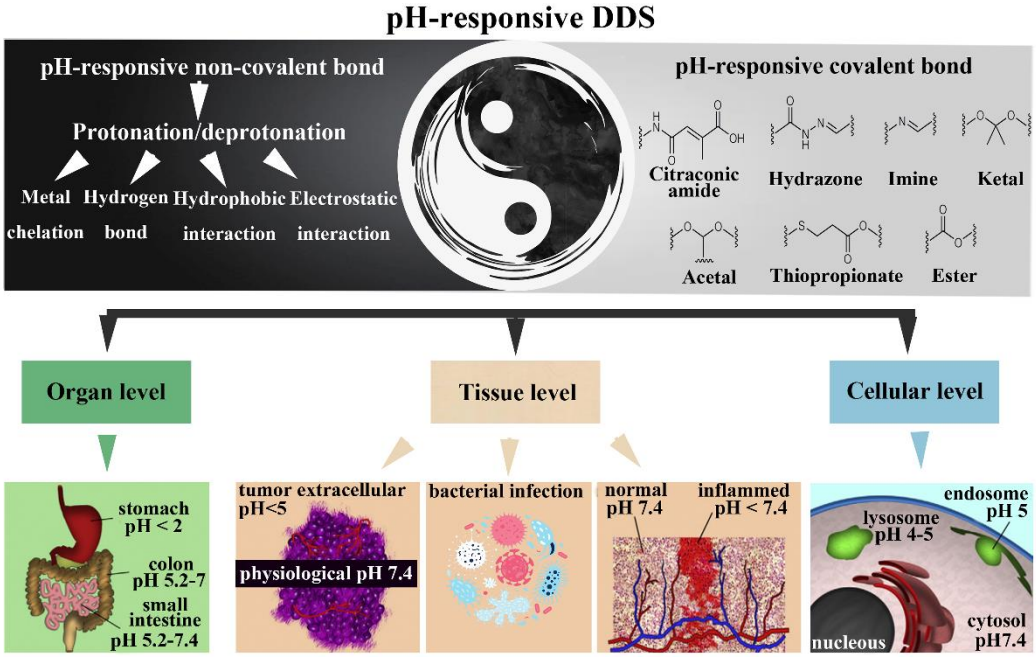

Figure 1. *Schematic representation of two strategies applied for fabricating pH-responsive DDS and corresponding potential biomedical applications in different diseases. Figure adapted and reprinted with permission from Ref.* [67].

One vigorously pursued area for acidic-sensitive DDS is cancer therapy. One of the hallmarks for tumor extracellular microenvironment is the overall decrease in pH-value compared to healthy tissue.[68] Tumor acidosis is generally related to hypoxia as a result of irregular angiogenesis induced poor perfusion.[69] This shifts the metabolic behavior of the cells from aerobic oxidation to glycolysis, generating a plethora of lactate. Simultaneously, the up-regulated expression of hypoxia inducible factor 1α (Hif-1α) can favor the passive release of lactate out of the cells, with the efflux of H^+, thus enhancing the acidification of the extracellular milieu.[70] The acidosis phenomenon is further exacerbated by the overexpression of carbonic anhydrases (CA) families, in particular extracellularly located CA IX, which hydrate CO_2 through the action of CA IX to generate H^+ and HCO_3^- and vented to the extracellular environment, further exacerbating the acidosis phenomenon.[71]

Acidic-responsive on demand DDS can also be applied in anti-bacteria therapy. Bacterial infection is one of the most refractory complications for tissue engineering. With

the impetus to study bacterial metabolism, acidosis is becoming increasingly recognized as a unique feature of bacterial infection, as bacterial growth will generate acidic products, such as carbonic acid and lactic acid, during respiration and fermentation, yielding an acidic microenvironment.[72, 73]

The pH-responsive strategy can be applied at cellular levels as an intracellular specific drug delivery platform. A well-established phenomenon is the acidic condition within the endosomal/lysosomal system.[74] Depending on the particle size and surface treatment of the DDS, it may enter the cells via different pathways, including phagocytosis, macropinocytosis, caveolin-mediated, clathrin-mediated and receptor-mediated endocytosis.[75] For nano-scale DDS, the dominant route for intracellular transport is cellular endocytosis, which initiates with the formation of early endosomes and ends up in lysosomes with acidic pH-values (pH 4–6).[76] Therefore, an acidic-sensitive platform may enable the endocytosis responsive drug release and substantially help in obtaining potential cellular imaging capabilities.

In spite of the multiple biological applications, the strategies or materials applied to fabricate pH-responsive DDS can be briefly divided into two categories. One is by employing pH-responsive non-covalent bonding, which can be dynamically disrupted by protonation or deionization under acidic environment, for example by introducing pH-responsive metal chelation or coordination bonds. Metal ions often exist as electron-deficient cations, and hence, are attracted to electron-rich molecules, such as proteins, DNA or other active pharmaceutical agents. Under physiological conditions, a deprotonated chelation center, which usually contains oxygen or nitrogen, can be generated with high charge density, therefore effectively coordinating with the metal, whereas the proton is displaced at lower pH-values, yielding an acid-triggered release.[77-79] For example, doxorubicin (DOX), a widely used chemotherapeutic agent for cancer therapy, is vastly presented as a DOX-iron (III) complex in biological systems.[80] Due to the alkaline nature of DOX with a pKa around 7.6–8.3, it will show a detained protonation level at physiological conditions, steadily coordinated with iron, whereas this chelation can be broken under acidic conditions due to the protonation of DOX.[81, 82] Upon such considerations, Liu *et al*. constructed an iron silicate based nanosystem through a silica template sacrificing method. The newly constructed NPs with enriched ferric ions on the surface could efficiently coordinate DOX, further achieving a pH-responsive release profile.[83, 84] In addition to coordination bonds, this protonation/deprotonation mechanism can also be feasibly transferred to hydrogen bonds or hydrophobic interactions. For example, chitosan, a widely used pH-sensitive polymer, can dissolve under acidic conditions due to the protonation of the amine groups, while it can precipitate and encapsulate multiple drugs at pH-values higher than 6.5 because of the hydrogen bonding between the hydroxyl and uncharged amine groups.[67, 85] Acidic pH-induced protonation brings forth a hydrophobic–hydrophilic phase transition for cationic polymers.[86, 87] Wu *et al*. prepared a poly[2-(diisopropylamino)ethyl methacrylate] (PDPA) containing amphiphilic block copolymer with a pK_a ~6.2. The block copolymer self-assembled into nano-micelles with a hydrophobic PDPA core for tight encapsulation of hydrophobic drugs via hydrophobic interaction. This bonding interaction was interrupted upon exposure to an acidic environment due to the protonation of PDPA block, transforming the copolymer amphiphilicity to double hydrophilicity.[88] Similarly, the protonation/deprotonation process

may also alter the surface charge of the colloidal particles, and the reversible charge can induce drug release via disturbing the electrostatic interactions.[89, 90] Overall, the aforementioned strategies leverage non-covalent bond disruption as a result of pH variation induced protonation/deprotonation and initiate the drug release at the desired site.

The second strategy to fabricating pH-responsive DDS is by utilizing acid-liable covalent bonds. So far, the most commonly used acid-liable covalent bonds include citraconic amide,[91] imine or benzoic-imine,[92] hydrazone,[93] ketal/ acetal and/or cyclic acetal[94] and ortho ester.[95] Drugs can either directly conjugate on the polymer backbone or side chains through labile bonds, or be encapsulated inside the carriers, which incorporating the corresponding bonds. The choice of the bond or materials is largely dependent on the requirement for drug release behavior. For example, hydrolysis of hydrazone or acetal is rather fast. Therefore the drug can be completely released within hours to a few days, whereas cleavage of imine or ester linkages are usually slow, which is beneficial for continuous and prolonged release. For example, Liu *et al*. encapsulated drug loaded porous silicon (PSi) NPs with acetalated dextran (AcDEX), where upon exposure to an acidic environment, the acetal bonds were hydrolyzed, rendering the hydrophobic AcDEX to degrade into hydrophilic dextran. Therefore, nearly 100% of the loaded drug (methotrexate) was burst-released within 5 h at pH 5.[96] Hu *et al*. reported a smart aminoglycoside DDS that conjugated antibiotics via the imine bond to demonstrate a pH-responsive on-demand drug delivery system. Below a pH-value of 5.0 (simulating the bacterial infection environment), more than 80% of antibiotics were released within 3 days.[92] The design of the materials should also be optimized depending on the biological conditions. Hydrazone has been extensively explored as a pH-responsive biomaterial. However, the hydrazone linkages with methyl on the nitrogen can only be hydrolized under a pH-value of 5, suggesting its potential application for intracellular drug delivery; hydrolysis of hydrazone linkages with acetaldehyde innitrogen readily occurs at pH 6, indicating its sensitivity towards the extracellular tumor environment.[97]

2.1.1.2 Oxidation-responsive DDS

Reactive oxygen species (ROS) often contain, or can be converted to contain, one or more unpaired electrons, and are therefore highly reactive and essential for biological functions by reacting with or modifying biological molecules, including DNA, proteins and lipids.[98] Examples of radical ROS include superoxide, nitric oxide, hydroxyl radicals, hydrogen peroxide and peroxynitrate. ROS may generate from the outer environment, such as oxidants from tobacco smoke or radiation; nonetheless, they are also endogenously generated from the activation of inflammatory cells by using predominantly nicotinamide adenine dinucleotide phosphate (NADPH) oxidases.[99] There is a delicate balance between the positive role of ROS (such as preventing pathogen infection, stimulating re-epithelialization and facilitating extracellular matrix remodeling)[100] and their deleterious effects under pathological conditions. However, chronic inflammation with long term exacerbation of NADPH oxidase activation may lead to excessive production of ROS, which further accelerates inflammation and oxidative stress.[101] Former clinical studies suggest that diseases involving long-term prognosis, such as cancer,[98] rheumatoid arthritis,[99]

diabetic wounds,[101] or steatohepatitis,[102] maintain highly oxidizing environments, which may lead to impaired treatment efficacy.

Upon such considerations, fabricating on-demand DDS that could respond to exorbitant ROS conditions has immense potential in biomedical DDS development. **Table 1** briefly summarizes commonly used ROS-sensitive moieties. One method is by introducing ROS cleavable moieties in the DDS. For example, phenylboronic acid ester (PAE) containing polymers have shown susceptibility towards H_2O_2. Gracia-Lux *et al*. catalyzed dimethylphenylboronic acid ester with benzylic bromination. The yielded compound was further functionalized as monomers to initiate step growth polymerization. As a result, the produced polymer showed a clear degradation at 1 mM H_2O_2 with 80% release of the loaded model dye within 20 h. However, the polymer has a relatively high polymer dispersity index (1.9), resulting in an overall low yielding degree. Meanwhile the absence of extra functional groups may further impinge on its biomedical applications.[103] Broaders *et al*., directly modified a natural polysaccharide dextran with PAE to obtain a H_2O_2 responsive polymer.[104] The newly synthesized polymer was prepared via a simple and facile method, and presented similar H_2O_2 sensitivities with full degradation at 1 mM H_2O_2. Nonetheless, the applied H_2O_2 concentration was a rather high dose and not biologically relevant Meanwhile, the oxidation was only initiated by H_2O_2 but not by other ROS, bringing forth further sensitivity concerns when considering *in vivo* applications. The sparing solubility of PAE-based polymers in various solvents further constrains the production of other formulations, and therefore a more deliberately designed system should be further conceived.

Another commonly used mechanism for fabricating ROS-responsive DDS is inducing a solubility change under ROS irritation. This method typically uses sulfur (II) containing materials, particularly hydrophobic sulfide moieties that can be oxidized to hydrophilic sulfoxides and sulfones.[105] The first demonstration of polyalkylene sulfide-based DDS were polymersomes formed by the triblock copolymer polyethylene glycol (PEG)-polypropylene sulfide (PPS)-PEG, which undertook a phase conversion of vesicles into micellar lyotropic aggregates at 0.03% of H_2O_2 (v/v), and showed a clear morphology change at 3% or higher H_2O_2 (v/v).[106] This inspired the formation of various sulfide containing polymers for ROS-sensitive DDS.[107, 108] The effective ROS concentration for the vehicle disruption, however, ranged from 1–10% H_2O_2 or 0.1–10 mM of 3-morpholinosydnonimine.[109-112] Given the scarcity of extracellular ROS, they were more often applied as a carrier for vaccines due to the higher oxidative content within immune cells.[113, 114] Despite the marginally robust incitement ROS concentration *in vivo*, one cannot deny the significance of such DDS complementing the useful array of pH-sensitive or other stimuli-responsive materials. Yet, to further explore versatility, the design and synthesis of a new ROS-responsive DDS should focus either on constructing biomaterials with higher sensitivity or engineering the DDS with a cascade ROS amplification capability, therefore reducing the required ROS concentration.[115, 116]

Table 1. Brief summary of the oxidation-responsive motifs and their oxidation mechanisms.

Responsive moieties	Chemical structure	Degradation mechanism	Ref.

Phenylboronic ester	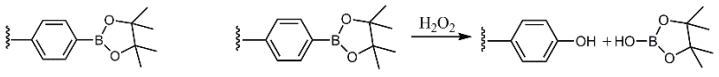	103, 104, 117, 118
Alkyl sulfide	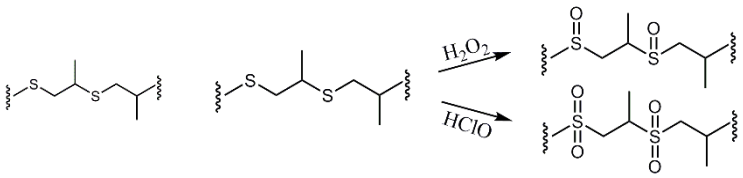	110, 111, 119
Disulfide or diselenide	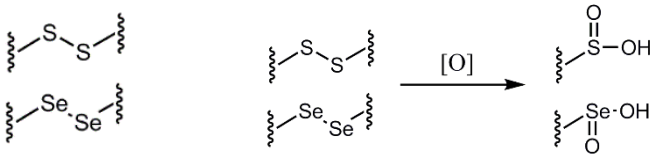	119-122
Thiolketal	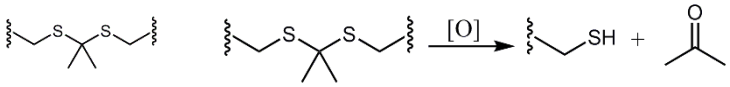	123-125
Peroxalate	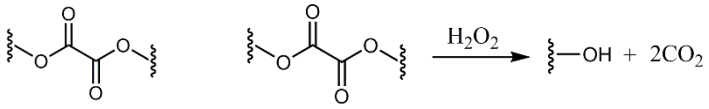	126-128

2.1.1.3 Glucose-responsive DDS

High glucose levels are a pivotal factor of diabetes and may shed light on the DDS construction for diabetes and its corresponding complications.[129] As a key energy supplier, a DDS that can both respond to glucose and also effectively consume glucose may further function as a starving-agent for some wasting diseases, such as cancer (**Figure 2**).[130] Several glucose sensing moieties or compounds were evaluated for biomedical applications. Phenylboronic acid (PBA) is one commonly used synthetic moiety for constructing glucose responsive on-demand DDS.[131] The inherent mechanism behind PBA facilitated glucose sensing is that PBA can be ionized with a hydroxide ion under aqueous conditions, and can therefore steadily react with 1,2- and 1,3-diols, such as glucose, allowing boronate ester formation. However, boronic esters have a pK_a slightly lower than that of free boronic acids. As such, the binding of diols with boronic acids can shift the equilibrium from the neutral species to anionic boronate esters, resulting in solubility changes from hydrophobic to hydrophilic, and electrostatic interaction alterations.[132] Langer *et al*. demonstrated a strategy for the chemical modification of insulin with a PBA containing aliphatic domain.[133] The incorporation of the aliphatic domain can effectively enhance the longevity comparing to the native insulin, whereas the sequential inclusion of PBA modulated the insulin exposure through alteration of hydrophobicity and electrostatic interactions upon glucose binding. The new system enabled rapid reversal of blood glucose in a diabetic mouse model, following glucose challenge over 13 h, over a clinically used long-acting insulin derivative, showing great promise for sustained insulin release.

Apart from synthetic moieties, natural glucose sensing proteins have also been explored for developing glucose responsive DDS. One example is integrating concanavalin A (ConA) in the DDS along with glycosylated insulin, which can effectively recognize and bind with

glucose.[134] Based on this, Kim *et al*. encapsulated both ConA and glycosylated insulin in a polymeric membrane that was permeable to glucose but not to ConA; the competitive binding between the glycosylated insulin and glucose achieved a glucose-responsive insulin release.[135]

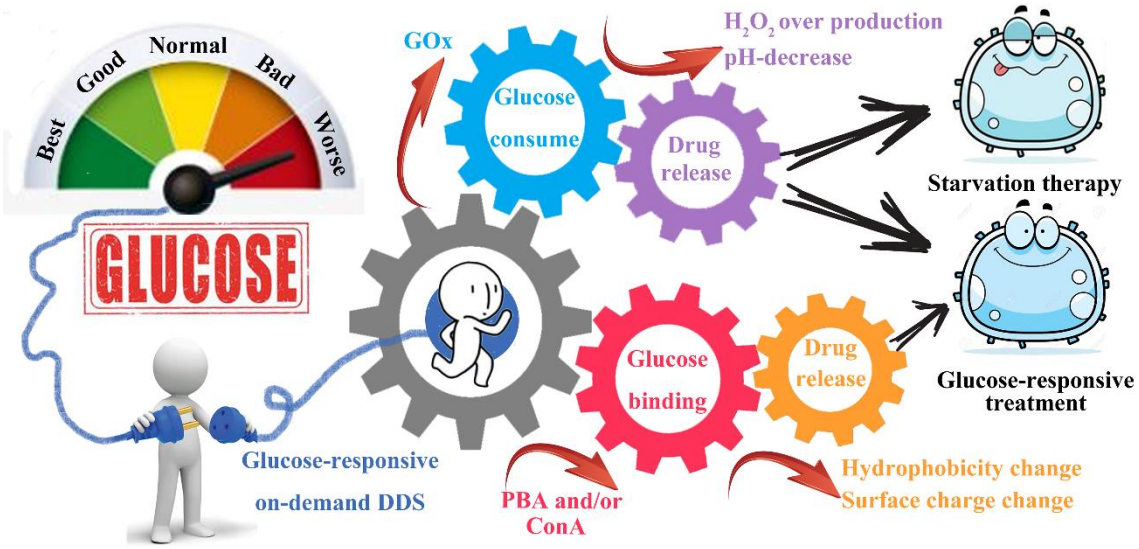

Figure 2. *Schematic illustration of two major strategies applied for constructing glucose-responsive on-demand DDS, either by applying glucose binding moieties, such as PBA or ConA to alter the physiochemical properties of the DDS to induce the drug release, or by applying GOx to oxidize glucose to produce H_2O_2 and gluconic acid, further initiating the following cascade.*

Over recent years, glucose oxidase (GOx) has attracted increasing interest in the biomedical field due to its inherent biocompatibility, non-toxicity, and unique catalysis against D-glucose.[136] GOx efficiently catalyzes the oxidization of glucose into gluconic acid and hydrogen peroxide (H_2O_2) and due to this unique feature, a multi-modal on-demand DDS was achieved by incorporating of GOx with pH-responsive or ROS-responsive DDS. Gu *et al*. recently reported a microneedle patch that integrated insulin loaded H_2O_2-responsive NPs with GOx.[117, 137, 138] By virtue of the generated H_2O_2 from GOx, the insulin-loaded NPs disassembled and subsequently released the preloaded insulin. *In vivo* studies showed a three-fold longer effective time in maintaining normoglycemia comparing to the native insulin counterpart.[117] The inspiring results indicated the potential success of applying GOx in other diabetes complications. However, corresponding formulation design and manipulation should be further considered, for GOx-containing bulk hydrogel usually exhibits insensitive response to glucose,[139] whereas GOx-containing membranes suffer from low mechanical strength, which can result in premature leakage of the drug.[140] A viable design should be further purposed according to specific disease condition and formulation requirements.

2.1.2 On-demand DDS for imaging

Imaging based techniques provide simple and powerful approaches to examine organ/tissue pathological changes, cellular trafficking of the DDS, or microenvironment variations of the targeting tissues or cells.[141] However, imaging or real-time imaging with high resolution remains a critical challenge. With the advent of cutting-edge nanotechnology, NPs serving as contrasting/imaging agents vastly promote this imaging possibility and efficacy. Integrating on-demand DDS with contrasting/imaging agents may provide a multipurpose system that has the ability to elucidate subtle, real-time changes within targeted sites, while simultaneously delivering the therapeutic.

2.1.2.1 On-demand DDS facilitated cellular imaging

Sensors that perform time-resolved measurements of intracellular metabolite levels are in great demand, as they can be used in biomedical diagnostics and to monitor biological processes, thus enhancing our general understanding of subtle biological changes. Fluorescence imaging allows direct, non-invasive yet effective monitoring of cellular behavior in real time. Compared to free dye, fluorescence sensors based on nanoscale biomaterials can reduce photo-bleaching,[142] prolong cellular retention and enhance local fluorophore intensity.[143, 144] Furthermore, sensors with the ability to alter fluorophore features under specific biological conditions, known as on-demand sensors, can monitor dynamic intracellular changes. This feature has particular significance for DDS evaluation, as it provides a valuable tool to visualize intracellular drug release or confirm the proposed formulation design, and hence, can preliminary evaluate the DDS design feasibility and performance.

Briefly, two types of fluorescence characteristic changes can be applied. The first strategy relies on fluorophores' intensity change in response to different stimuli. For example, quercetin, a natural anti-cancer flavonoid, is described to have the capability to exert such a function.[145] Quercetin shows a clear fluorescent feature, however, due to the anthocyanidins ring structure within quercetin, when they are compacted or conjugated with another fluorescent compound, or quercetin itself, both the fluorescence signals can be effectively quenched through an electron transfer mechanism.[146-148] Based on this, Wu *et al*. developed glutathione (GSH) sensitive NPs DDS based on quercetin.[34] Two quercetin molecules were connected via a disulfide bond, which was cleaved upon contact with GSH. Then disulphide-bridged quercetin (QSSQ) was self-assembled into NPs via a precipitation method. Both the newly formed NPs and free QSSQ did not show significant fluorescence (**Figure 3A**). Facilitated by this feature, they observed both real-time GSH-dependent drug release, and also screened the GSH overexpression cancer cells, providing a useful tool for evaluating the metabolism of different tumors and facilitating a personalized treatment (**Figure 3B,C**).

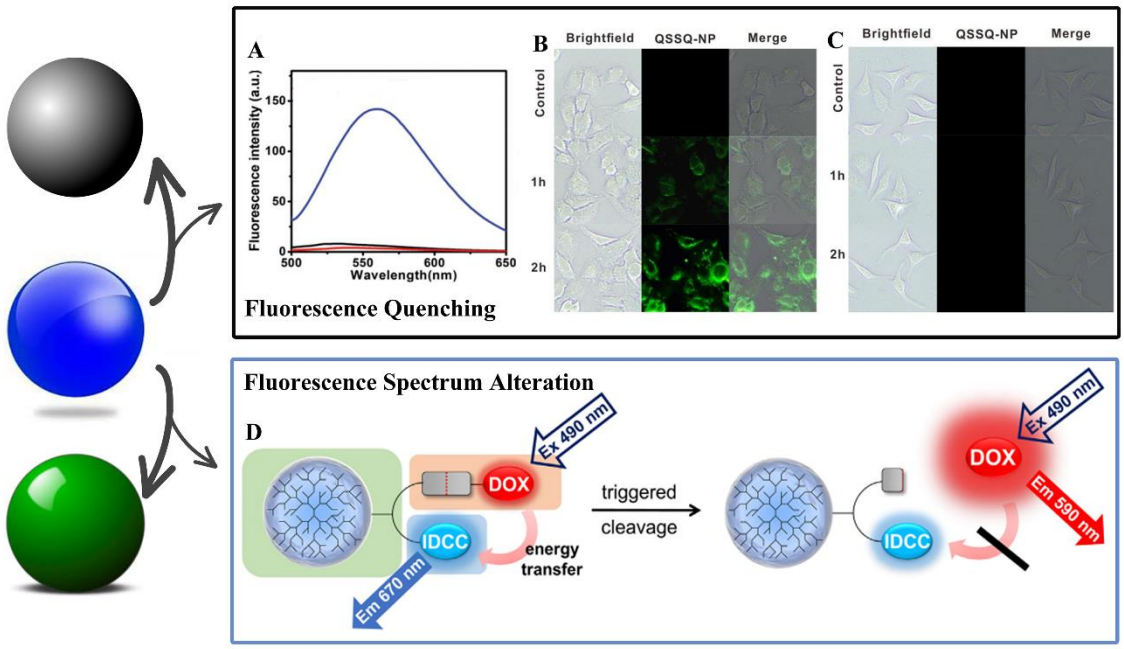

Figure 3. *Fluorescence based on-demand imaging can be briefly divided into fluorescence quenching or fluorescence spectrum changes. (A) Emission spectra for free quercetin (blue line), QSSQ (black line) and QSSQ NPs (red line). Excitation wavelength: 485 nm. (B) The on-demand fluorescence quenching can be applied to monitor the drug release. (C) Screen of the GSH expression level for different cancer cell lines. (D) Schematic representation of the FRET design and mode of action of the system, including excitation (Ex.) and emission (Em.) wavelengths. Figures A-C are reprinted with the permission from Ref.* [34]*. Figure D is reprinted with the permission from Ref.* [149]*.*

The second strategy relies on the fluorophores' spectral shift in response to different stimuli. Implementation of this phenomenon can be achieved by applying the fluorescence resonance energy transfer (FRET) effect. FRET is the physical process by which energy is transferred from the emission light of one chromophore (donor) to another chromophore (acceptor).[150, 151] The FRET efficiency is dependent upon the distance between donor and acceptor molecules (r): $E_{FRET} = 1/\left[1 + \left(\frac{r}{R_0}\right)^6\right]$, where R_0 is the characteristic distance at 50% FRET efficiency.[152] Because the efficiency is reduced with the sixth power of r, the FRET efficiency steeply drops off once the distance between the two fluorescent molecules exceeds R_0. Due to this property, FRET can be feasibly applied to monitoring the release of the drugs, especially drugs with distinct fluorescent spectrum such as DOX, from the DDS.[153, 154] Nagel *et al.* constructed a DOX (donor) loaded pH-responsive DDS with different acid-labile bonds, and further conjugated the fluorophore indodicarbocyanine (acceptor dye) in close proximity to DOX to fabricate a FRET complex.[149] The newly constructed system can observe the DOX release through real time spectral changes and evaluate the sensitivities of different acid-liable bonds, providing basic knowledge for further DDS design (**Figure 3D**).

2.1.2.2 On-demand DDS facilitated bio-imaging diagnosis

The accumulation of NPs at desired sites may further endow the sites with distinct features when comparing to surrounding tissue, and may therefore function as contrasting agents for bio-imaging facilitated diagnosis.[155] For example, iron oxide-based NPs can be applied to magnetic resonance imaging (MRI) due to its paramagnetic or superparamagnetic property;[156] the unique physical and optical properties, such as strong X-ray attenuation, photothermal capability and enhanced surface resonance emission of gold nanoparticles (Au NPs) have led to various schemes for developing Au NPs as a contrast-enhancing agent for computed tomography (CT) imaging, photoacoustic imaging and Raman imaging.[157-159] However, *in vivo* performance of bare NPs as a contrasting agent is usually unsatisfactory. This is mainly due to the heterogeneous biological environment, which usually brings contradictions for NPs design, ranging from size and surface charge to surface modification (**Figure 4**).[53, 160] For example, the optimal NP size may shift during the NP transporting process. Several studies have demonstrated the feasibility of applying CT imaging to track monocyte recruitment to tissue plaques using Au NPs; however, too small NPs (< 5 nm) suffer from rapid clearance by renal filtration, leading to low plaque accumulation, and they also tend to show limited monocyte phagocytic system (MPS) uptake, resulting in an unsatisfied lesion tracking ability.[161, 162] Larger NPs (> 150 nm), despite their favourable MPS uptake and contrasting ability, can hardly be excreted from the body and show higher cellular toxicity.[163] Another example comes from the surface modification, Au NPs modified with PEG can enhance their stability and longevity, thus have higher chance to reach to lesion sites, whereas the PEG modification can hinder the tissue penetration and renal clearance of Au NPs, as such affecting imaging efficiency and biocompatibility.[164, 165] On-demand strategy aims to recapitulate the specific environment and change their properties accordingly, and thus may also be incorporated in the fabricated contrasting agent.

Upon such considerations, various on-demand NPs are constructed and applied to enhancing imaging capabilities. Three major disciplines are widely applied, including size alteration, surface charge reversion and surface ligand activation/cleavage.[160] The manipulation of size can widely impact the bio-distribution and bio-behavior further affecting the imaging efficiency, which has been rigorously explored. Mao *et al*. crosslinked small Au NPs (15 nm) to form larger Au clusters (190 nm) via matrix metalloproteinase (MMP)-2 cleavable and pH-responsive hydrazone bonds.[166] The Au clusters were decomposed back to Au NPs within the tumor microenvironment due to the overexpression of MMP-2 and acidic environment, and thus showed enhanced tumor penetration and contrasting ability in CT imaging. Stimuli-responsive size alteration-induced imaging modalities can also facilitate bio-imaging. For example, Lu *et al.* explored pH-responsive iron oxide NPs for MRI imaging.[167] Ultrasmall iron oxide NPs (< 4 nm) demonstrated enhanced T1 MRI contrast, providing positive contrast (bright signal) on the T1-weighted MR images, while larger iron oxide NPs provided negative contrast (dark signal) on the T2-weighted MR images. The modification of ultrasmall iron oxide NPs with i-Motif DNA, which exhibited a pH-triggered structural change, caused aggregation of the iron oxide NPs at neutral pH, generating a dark signal, while at the tumor site the aggregates decomposed back to ultrasmall iron oxide NPs, generating bright signals. This double-enhancing phenomenon can dramatically increase MRI resolution. However, most methods involve a

chemical conjugation and reaction, which may bring further obstacles for chemical reagents' removal and quality control Therefore it is preferred to establish an alternative physical method to accomplish the envisioned design.

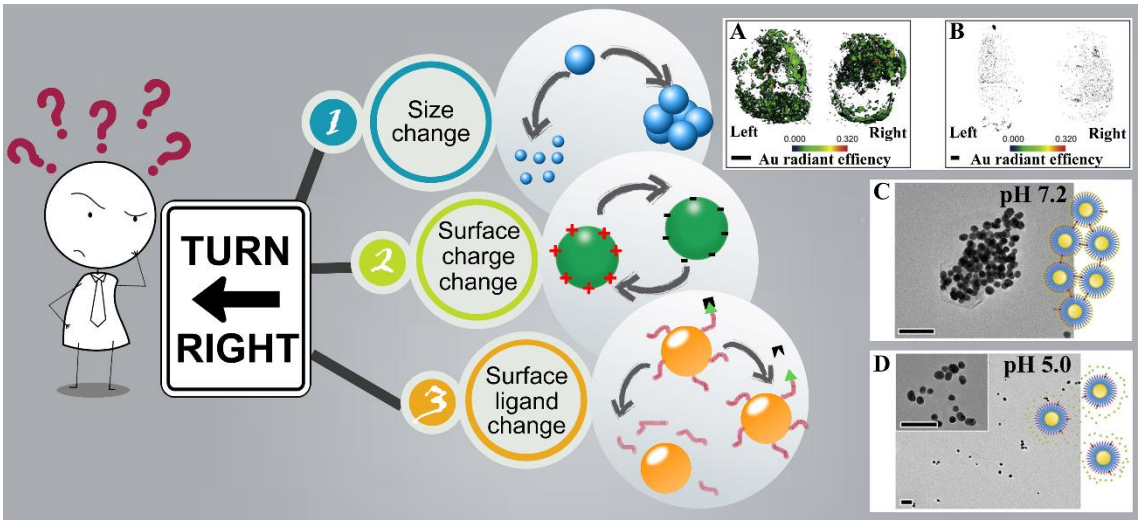

Figure 4. *Heterogeneous in vivo microenvironment may bring contradiction for NPs design. On-demand strategy can endow the system with changeable particle sizes, switchable surface charges and activatable/cleavable surfaces, enhancing the imaging capability. (A) pH-responsive Au NPs with changeable size showed enhanced CT imaging capability comparing to (B) plain Au NPs. (C) and (D) TEM images illustrated the pH responsive size change of Au NPs via chemical conjugation. Figures are reprinted with the permission from Ref.* [166].

2.2 Advanced materials for DDS fabrication

The previous sections briefly discussed the design principles for fabricating advanced DDS. This section will focus on the selection and modification of specific biomaterials to fulfill the envisioned designs. Two types of biomaterials, inorganic (PSi NPs) and organic (dextran-based polymer) materials are mainly studied in this thesis and will be separately discussed here.

2.2.1 Porous silicon (PSi)

PSi was accidentally discovered by the Uhlirs at Bell Labs in 1956, when they were searching for a technique to shape the surface of silicon.[168] However, it was not until the late 1980s that the scientific community pursued further interest in PSi, when Dr. Canham revealed that PSi could emit light if subjected to electrochemical and chemical dissolution due to the quantum confinement effects.[169] Along with the increasing investigations for PSi-based optoelectronic devices, in 1995, Dr. Canham further tested its potential biocompatibility with promising results,[170] and he later evaluated PSi as a DDS for the anti-cancer drug cisplatin.[171] As a sequence, a new era was opened for the biomedical applications of PSi. The present-day applications of PSi range from bio-imaging, DDS

fabrication, sensors and battery anodes for energy storage.[13, 17, 172, 173] Herein, we focus on the biological applications of PSi.

2.2.1.1 Biocompatibility and immunomodulatory effect of PSi

Biocompatibility is a fundamental material characteristic required for biomedical applications. Freshly etched PSi with a hydride surface (Si-H) is not fully biocompatible due to its high reducibility and the sequential singlet oxygen ($^1O_2$) generation as a result of photo-oxidation.[174, 175] Surface stabilization of PSi can vastly promote the biocompatibility of PSi,[175] and mainly three types of surface stabilizations have been investigated for the past few decades, namely oxidation, carbonization and hydrosilylation (**Figure 5**).[13] Different surface chemistry can inevitably alter the PSi surface charge, hydrophobicity, degradation rate and biological molecule binding pattern, rendering different interactions between PSi and biological systems.

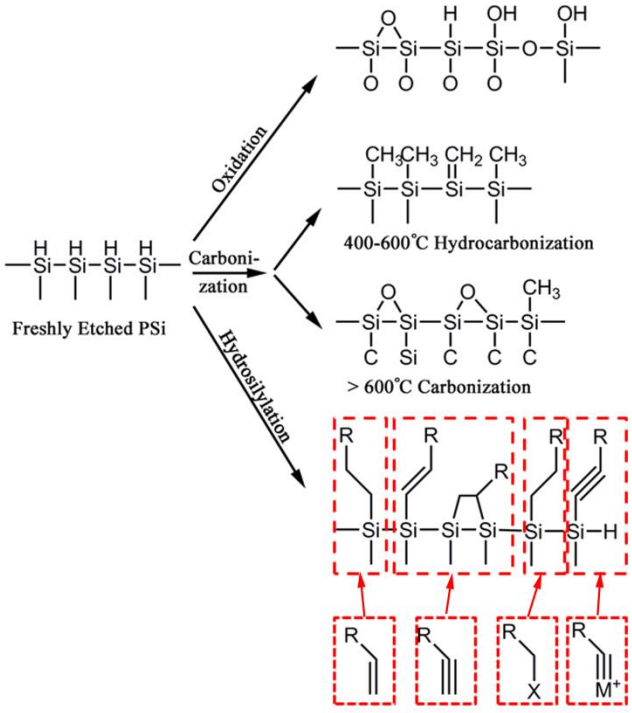

Figure 5. *Basic graphic illustration of primary surface modifications for freshly etched PSi. Copyright © (2018) John Wiley & Sons, Inc., reprinted with permission from Ref. [13].*

One criterion used to evaluate the biocompatibility of PSi is immunogenicity. Understanding the inflammation response of PSi with different surface properties is essential for discerning which type of PSi should be administrated to elicit a desired biological response. One of the first thorough trials to evaluate the immunogenicity of PSi was conducted by Ainsile *et al.*,[176] where human blood-derived monocytes were seeded on PSi plates with different topography. Ten key inflammation-related cytokines (interleukin (IL)-1α and β, IL-12, IL-6α, tumor necrosis factor (TNF)-α, interferon (IFN)-α and γ,

macrophage inflammatory protein (MIP)-1α and β, IL-10 and IL-6) and ROS levels were evaluated, respectively. Despite fluctuating cytokines expression with topographically different PSi plates, the PSi plate with a nanoporous surface structure showed an overall reduced cellular ROS response compared to that with a polystyrene culturing plate. This phenomenon could be potently explained by the further work developed by Artzi *et al*.[177] Within this study, the degradation kinetics of PSi microparticles with a hydrosilylation surface was investigated. Surprisingly, the authors found that among all the factors (pH, serum, and ROS), ROS concentration exhibited the most important role in determining the degradation rate of PSi, which was due to the reductive nature of PSi back bonds. *In vivo* studies further confirmed the elevated PSi degradation rate at a lesion site (tumor) compared with healthy tissue. Other reports utilized silicon magnesium nanohybrids to create a reductive environment due to the silicon hydride production.[178, 179] Considering the critical effect of ROS in inflammation regulation, the ROS scavenge effect of PSi may have further effects on modulating the inflammation.

As a result of its heterologous nature, PSi can also directly interact with immune cells, rendering immuno-stimulative/suppressive effects. Shahbazi *et al*. investigated the immunomodulatory effect of PSi NPs with different surface chemistries.[180] Antigen presenting cells (APCs) were used as model cells due to their ability to recognize foreign entities and induce immune response via T cell activation by expressing cognate ligands (CD80/CD86), and/or releasing cytokines and chemokines to shift inflammation direction. Results showed that thermally oxidized PSi (TOPSi) can significantly promote the maturation of APCs, which was confirmed by enhanced CD80/CD86 expression and elevated pro-inflammatory cytokines excretion. However, thermally carbonized PSi (TCPSi) and undecylenic acid functionalized thermally hydrocarbonized PSi (UnTHCPSi) showed sparing immuno-stimulation effects, and even inhibited the activation of type 2 T helper cells (Th2) to different extents. Similarly, surface oxidized discoidal PSi microparticles, despite the altered size and shape compared to spherical PSi NPs, also stimulated the secretion of pro-inflammatory IL-1β from murine bone marrow-derived dendritic cells (BMDCs) in a time and dose-dependent manner.[181] Xia *et al.* further explained the mechanism of this phenomenon as the phagocytosis of PSi might activate Toll-like receptor sole adapter molecule (TRIF)-dependent signaling, which elicit type I interferon (IFN-I) response in BMDCs.[182] Despite the thorough investigations of the immune activation processes from surface oxidized PSi, there are only a few papers which can properly explain the varied immunogenicity of PSi with different surface chemistries.

The complexity of the immune system confers a formidable challenge to elucidate the effect of a sole factor on immunogenicity. Indeed, previous studies suggested that particle-induced immune response can be affected by, *e.g.* particle size, shape and surface properties.[183-185] Nonetheless, recent studies have suggested that there is a key factor that may bridge these factors together. The original NPs' surface properties will be immediately redefined upon being injected into the body due to the protein corona formation, which can further prime the immune response of particles. Different protein corona formation can regulate the NP/cellular interactions, thus altering the toxicity, targeting ability, bio-distribution and immunogenicity of the NPs.[186-188] Tenzer *et al*. analyzed time- and NP-dependent protein corona formation, which shed light on the pathophysiological behavior of different NPs.[189] A more specific study was developed by Mo *et al*., who found a

decreased immune response from two types of black phosphorous NPs with reduced size.[190] The composition of protein corona was further separated and analyzed via mass spectrometry, and the results revealed that only 12.5% of overlapping proteins existed in the protein corona composition, and the difference in the protein binding pattern directly dictated the immune response. For PSi, Wang *et al*. previously demonstrated that thermally hydrocarbonized PSi (THCPSi) with a dextran coating could reduce immune protein (fibrinogen and immunoglobulin G) adsorption compared to bare THCPSi, thus further restraining the immuno-stimulation.[191] However, the direct *in vivo* immunogenicity comparison of PSi with different surface properties still remains a less investigated topic. Moreover, previous studies usually investigated the immunogenicity of NPs on healthy animal models, whereas in real cases, particulate DDS will be preferably accumulated in lesion sites, and the immuno-modulatory effect of NPs under pre-existing inflammation conditions may affect the pathological progression, determining the final treatment efficiency. Yet, only few studies have been conducted so far taking into consideration these issues.[192]

2.2.1.2 PSi for controlled drug release

Due to the porous structure of PSi, it can be applied for loading various kind of cargos, including small molecule drugs, peptides, proteins, DNA, siRNA and even other NPs. However, bare PSi shows some inherent drawbacks for DDS fabrication, and therefore need further modification. The most common problem is generated by its freely accessible pores (~10 nm), which may result in uncontrollable release, and even inactivation of the cargos due to the disruptive effect from body fluids when PSi is applied *in vivo*. Different methods have been designed and applied to solve this problem. The simplest and most convenient method is adjusting the PSi surface properties to facilitate drug loading and release. Hydrophobic interactions can refine the crystalline structure of the drugs and facilitate hydrophobic drug loading. Therefore fresh PSi was thermally carbonized to form hydrophobic surfaces, which were further applied for loading the hydrophobic anti-cancer drug sorafenib.[193] Due to the strong hydrophobic interactions, sorafenib cannot be released from TCPSi in 4-(2-hydroxyethyl)-1-piperazineethanesulfonic acid (HEPES) buffer at different pH-values, suggesting its potential for long term storage. However, when 10% of fetal bovine serum (FBS) was added in the releasing medium, more than 90% of sorafenib was released within 1 h, suggesting the limitation of this method when applied *in vivo*. In addition, the physical loading method generally lacks reproducibility and suffers from loading efficiency. Thus, advanced methods should be further proposed.[23, 193]

Wang *et al*. leveraged a covalent chemical conjugation method to achieve controlled release kinetics from PSi. Amine-terminated thermally carbonized PSi was reacted with the anti-cancer drug methotrexate to form an imide bond. A conjugation/loading degree of ~0.4% was achieved and a controlled release profile was observed for up to 96 h.[194] Despite the prolonged release time, mass spectrometry results suggested that the released compound was 3-aminopropylesilicic acid conjugated methotrexate, due to the decomposition of PSi. Hence, this method induces the concern that changing the chemical structure of the compound might disturb the activity of the drug. Thus, an alternative method utilizing dynamic non-covalent bonding should be further purposed and investigated.

In addition to chemical bonding, physical pore blocking is another commonly applied strategy to fulfill the controlled release goal. PSi with hydrosilylation modification undertakes moderate degradation within aqueous solution, which will generate orthosilicic acid. The degradation product can form *in situ* into a Ca_2SiO_4 precipitate in a high calcium ion (II) containing medium. The self-limiting precipitation occurs primarily at the PSi surface, which consequently forms a shell around the structure. Kang *et al*. applied this method to encapsulate siRNA and a distinctive sustained release profile (> 5 h) was achieved. Organic materials can also be applied for PSi encapsulation. THCPSi encapsulated in a solid lipid matrix showed an elevated stability and prolonged drug release, where the model drug furosemide showed a sustained release behavior for over 10 h.[37] Outer shell materials can also induce a responsive release profile. For example, the enteric coating material hypromellose acetate succinate encapsulated e insulin-loaded PSi, and the produced nanohybrids protected the insulin from the stomach's acidic environment, while releasing the PSi in the intestinal tract.[195] Compared to chemical conjugation, physical encapsulation has more increased versatility and feasibility, yet a more robust method with high throughput production should be proposed.

2.2.2 Dextran based polymers

Biodegradable polymeric materials have several inherent advantages, such as flexibility, ductility and processability, and thus they have been widely investigated for biomedical applications.[196] Compared to synthetic polymers, natural polymers are overall more biocompatible and biodegradable. Nonetheless there is also a limitation in the performance of natural polymers in comparison to synthetic polymers, in regards to mechanical properties, thermal stability, shaping efficiency, and stimuli-responsivity.[197, 198] Subsequent chemical modification may provide natural polymer derivatives some tailored chemical functions and structure, and substantially fulfill the unmet requirements mentioned above, thus drawing increasing practical interest for further research.[199] Dextran, a natural polysaccharide with a linear backbone of α-linked d-glucopyranosyl repeating units, is one of the few FDA approved natural polymers with favourable aqueous solubility. It can also be biodegraded with the assistance from fibroblasts and macrophages without causing obvious immuno-responses (**Figure 6**).[200] The abundant hydroxyl groups within the dextran units provide feasible reaction sites for chemical modifications, further providing dextran-based polymers the capability to acquire selectively tailored molecular assemblies and interfaces, rendering them more suitable for different biomedical applications.

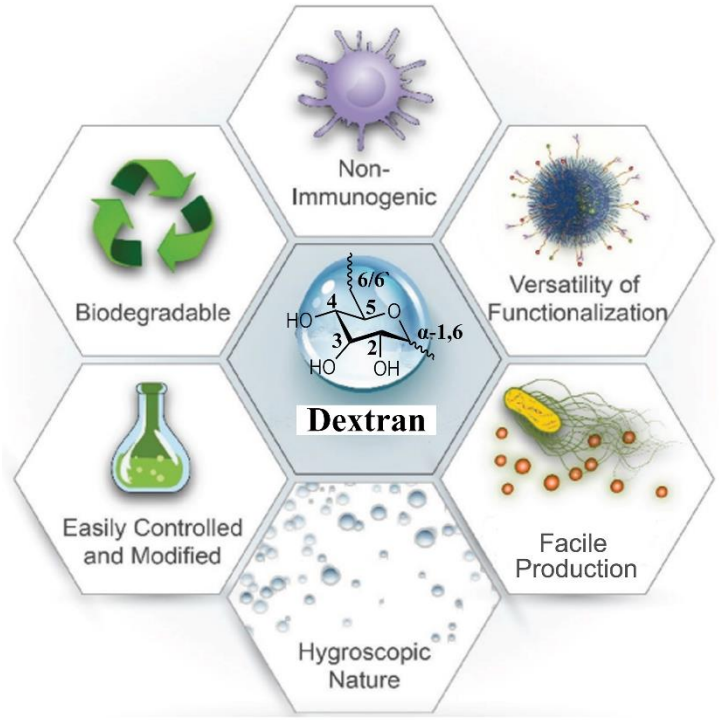

Figure 6. *Advantages of dextran for biomedical applications. Adapted and reprinted with the permission from Ref. [199].*

One of the first attempts to chemically modify dextran was with periodate induced oxidation, where vicinal diols were attacked by a periodate ion and induced carbon bond breaking.[201] Typical dextran oxidation happens between carbons C3-C4 within the α-1,6 residues. The attacked C-C bond breaks and yields two aldehyde groups, and the oxidation degree can be tuned by altering the periodate concentration.[202] This simple procedure functionalizes the dextran chain with extra aldehyde groups, which are mainly characterized by their highly reactive nature towards N-nucleophiles, such as amines, hydrazines or carbazates to form into pH-sensitive (imine) bonds. These oxidized dextran (ODEX) can function as a cross-linker to form hydrogels with amine-containing polymers, such as chitosan or collagen.[203-205] Compared to other commonly used cross-linkers, such as glutaraldehyde or genipin, ODEX showed better biocompatibility and a non-inferior crosslinking efficiency to enhance the durability and mechanical property of the yielded hydrogel.[203] Moreover, an amine-containing drug can be concurrently encapsulated in the hydrogel to achieve an acid-liable release profile. This pH-responsive release may be beneficial for further, specific biomedical applications, such as tissue engineering or cancer therapy.[92, 206]

Due to the excellent aqueous solubility of dextran, micellization or colloidal preparation of dextran into NPs is challenging.[207] By grafting hydrophobic functional pendent groups on the dextran hydroxyl, one can alter the polymer solubility to facilitate colloidal NPs production, and also develop stimuli-responsive polymeric materials based on the chemical properties of the pendent groups.[26] One example comes from the acetalation of dextran to yield the pH-responsive AcDEX. The preparation of AcDEX was first reported by Bachelder *et al*., where 2-methoxypropene was used to modify dextran.[94] Sufficient

hydroxyl substitution by ketal/acetal groups makes AcDEX insoluble in water, but soluble in multiple organic solvents. This hydrophobicity alteration allows AcDEX NPs synthesis via facile methods, such as emulsion or precipitation. Attributed to the acid-liable nature of acetal/ketal bonds, AcDEX will undertake fast degradation under pH 6, generating water-soluble dextran, methanol, and acetone as degradation product. This pH-responsive degradation makes it a perfect candidate for constructing a series of pH-responsive on-demand DDS. The structure changes or degradation of the modified hydrophobic pendants on the hydroxyl groups can also result in different on-demand behavior. Broaders *et al.* conjugated phenylboronic acid ester (PAE) onto dextran to yield an oxidation responsive polymer (Oxi-DEX). Due to the sensitivity of PAE towards H_2O_2, Oxi-DEX degraded back to water-soluble DEX and borate upon the addition of H_2O_2, and is thus capable of being applied to the fabrication of oxidation-responsive on-demand DDS.[208] Despite the successful application in constructing DDS for vaccine delivery, this polymer can only respond to H_2O_2, but not to other ROS species, and the effective degradation can only be initiated at relatively high H_2O_2 concentration (1 mM), which is barely achieved within the extracellular environment.[115, 131] In addition, boronic acid may form a transient crosslink with vicinal diols in dextran, and thus restrain the solubility of Oxi-DEX in most of the solutions. The addition of methanol can partially resolve the solubility impediments, but it may induce methanolysis, which might be detrimental for the NPs fabrication.

Overall, despite the obvious advantages of applying dextran as a precursor backbone polymer, an elaborative pendent choice should be further considered to achieve the envisioned design for fabricating the functional polymers.

2.3 Microfluidics for NPs preparation

As mentioned above, the on-demand strategy brought up the proof of concept to fabricate corresponding DDS for responsive/controlled release of loaded drugs, as well as synchronously exerting extra functions, such as cellular imaging, drug release monitoring and bio-imaging facilitated theranostics. However, the envisioned design needs cutting-edge techniques to accomplish the NPs fabrication. In recent years, the concept “Lab on a Chip” dramatically accelerated the development of miniaturized systems for healthcare related applications.[209] As a fundamental regime, microfluidics, a technology characterized by the engineered manipulation of fluids at the submillimeter scale, has become a revolutionary alternative method in the biomedical field.[210] It has been widely applied in 3D cell cultures, single cell analysis, cell/molecule isolation and purification, body fluidic stream simulation, organ on chip, micro/nano-fibers production and micro/nano-particles production.[38, 41, 211] From a pharmaceutical point of view, certain advantageous properties of applying microfluidics technology to fabricate micro/nano-sized particles, such as rapid and controllable processing with favourable reproducibility, have made it an attractive candidate to replace traditional approaches for producing NPs or microparticles. The following sections will briefly discuss recent technologies that applied microfluidics to fabricate advanced DDS, and the potential formation mechanisms.

2.3.1 Microfluidic-assisted production of NPs

The initial and most widely applied particulate synthesis via microfluidics is for microparticles production. However, the focus here will be mainly on NPs' fabrication. NPs are conventionally synthesized by batch type reactors, where the scarcity of batch-to-batch reproducibility for bulk-method is usually a refractory obstacle for quality-control. **Figure 7A-C** briefly illustrates the basic method for microfluidic-assisted NPs production. Using microfluidics, the continuous synthesis of NPs was found to obtain better reproducibility and controllability compared to batch-type bulk synthesis methods.[212] This is mainly due to the unique fluid dynamics in microfluidic systems.

Most of the bottom-up NPs formation undertakes two phases, a nucleation phase and growth phase.[213-215] Theoretically, the NPs precursor (fully dissolved lipid or polymers for organic NPs and ions or ions/ligand complex for inorganic NPs) will be evenly distributed within a homogenized solution. Upon the addition of an initiator (anti-solvents for organic NPs and reacting agent for inorganic NPs), the precipitation or reaction is initiated and forms into NPs (**Figure 7D**). The successful synthesis of monodisperse NPs is critically dependent on the complete separation of the nucleation and growth stages, which requires precise control over the concentration of reagents, reaction temperature and reaction time.[213] However, in most cases, the reaction or precipitation usually happens in a heterogeneous environment due to the detained mass or heat transfer, leading to uneven mixing, local temperature fluctuations and uncontrolled reaction times,[216] thus resulting in relatively high polydispersity and batch-to-batch variation. For example, the most commonly used method for fabricating polymeric NPs is anti-solvent induced precipitation or self-assembly. The counterbalance between the time scale for thorough mixing of the anti-solvent (t_{mix}) and the time scale for polymer nucleation (t_{nul}) directly determines the successful construction of the NPs. Only when $t_{mix} < t_{nul}$, can the nucleation occur in a homogenized environment, and effectively prevent the secondary nucleation due to non-homogenous local polymer concentration.[217, 218] Therefore, one pivotal factor to construct NPs with good reproducibility and monodispersity is to increase the mixing efficiency. Microfluidics can widely increase in surface area-to-volume ratio by even several orders of magnitude.[42] For a system containing two or more phases of miscible fluids, which is mainly used in microfluidic-assisted NPs production, the widely enhanced surface area-to-volume ratio allows for more efficient mass or heat transfer within the system; This reduces the homogenization time to micro-second levels,[212, 219] and provides a new era for fabricating NPs via bottom-up methods.

The typical method for microfluidic-assisted NPs' production is by introducing two or more coaxial flows, which separately contain precursors and initiators. The NPs will spontaneously form upon the mixing of the co-flows within the channels (**Figure 7A-C**). Diffusion and convection are the two regimes commonly used in microfluidics that contribute to the mixing efficiency. Diffusion refers to the random motion of solutes driven by a gradient in chemical potential and convection refers to the mixing caused by the convective motion of fluids.[220] When discussing about mass transfer, one parameter is inevitably to be introduced for further discussion. The Peclect number (Pe) describes the ratio between characteristic time of diffusive mixing and characteristic time of convective mixing, where higher Pe indicates a more important role of convective bulk flow within the

mixing.[221] Based on the equation, Pe = $^{VD}/_{d}$, where *V* is the total flow speed within the microfluidics channel, *D* is the hydraulic cross-sectional diameter of the channel and *d* is the mass diffusion coefficient of the solute. For a typical sub-millimeter sized microfluidic channel (with the a diameter less than 10^{-3} m), two miscible fluids (such as ethanol and water, which is one of the most commonly used fluidic systems for fabricating polymeric NPs) usually obtain a typical Pe number ranging from 10^2 to 10^4,[222] suggesting the main function of convection flow during the mixing. Given the knowledge that the extent of convection is mainly dominated by the fluidic pattern in the microfluidics channel, to better understand and control the mixing, another important dimensionless parameter is introduced, namely Reynolds number (Re). Re, defined as Re = $^{\rho Q}/_{\eta D}$ = $^{Q}/_{\nu D}$, where ρ is the density of the fluid, *Q* is the total flow rate of the fluid, η is the viscosity of the fluid, ν is kinematic viscosity of the fluid and *D* is the hydraulic diameter of the channel, reflects the ratio of inertial to viscous force within the fluid.[220] Because viscosity produces a resistance to shear and the fluids have a tendency to move in parallel layers, the increase in Re suggests a more chaotic and stochastic fluidic pattern, ultimately resulting in a shift from laminar to turbulent flow. Despite the difficulty in predicting and modeling fluid mechanics in turbulent flow, the mixing efficiency within the turbulent regime is enhanced since convective mixing does not occur in laminar flow and is therefore preferred for NPs synthesis.

Therefore, one method to increase the mixing efficiency is by promoting the Re number. Based on this theory, Farokhzad *et al*. used a co-axial microfluidics device to synthesize a series of NPs, ranging from polymeric NPs (PLGA-PEG, polystyrene), liposomes to metal nanoclusters (iron oxides) via the nanoprecipitation method. Re was varied by tuning the total flow rate and flow velocity ratio between the inner and outer fluids ($R_{in/out}$). Under a fixed $R_{in/out}$ value, with the increase of Re, a clear flow pattern change from laminar flow to vortex and turbulence flow, and ultimately to turbulent jetting, was observed (**Figure 7E**). It should be noted that the conventional transitional Re number (Re_t), which refers to the critical Re number when the flow pattern shifts from laminar flow to turbulent flow, is usually observed at around 2000 to 2300. However, in microfluidics, a clear turbulent flow can be achieved with a Re number lower than 500.[223] Peng *et al*. first reported that the transition to turbulence occurred at Re numbers as low as 200–700 in micro-channels with hydraulic diameters of 133–367 μm,[224], and a similar phenomenon was observed by Mala *et al*. and other groups.[225] They attributed this phenomenon to the decreased diameter and increased surface roughness of the channel. In a comprehensive review illustrating the calculation of Re in a microfluidics system, Gravesen *et al*. claimed that Re_t in a microfluidics system should be consider the channel length.[223] Despite the controversial conclusion about the Re_t within microfluidics channel and corresponding flow pattern,[226] Farokhzad *et al*. clearly demonstrated that by simply manipulating Re number, one can fabricate NPs with significantly enhanced homogeneity comparing to bulk method.[227] To further illustrate the mechanism, they evaluated the t_{mix} through both by macroscopic observations and mathematical modeling. Results showed that the t_{mix} was tunable in the range of 7–53 ms by changing the Re, which was considerably lower than the typical t_{nul} of polymer (~1–100 ms, depending on the molecular weight of the chain, **Figure 7F**).[212, 217] Liu *et al*. further applied a computational fluidic dynamics (CFD) method to confirm the amplified microvortices in the microfluidics channel along with the increase of Re (**Figure**

7G), confirming the evaluated mixing efficiency and NPs homogenicity by increasing the Re number (**Figure 7H**).[228]

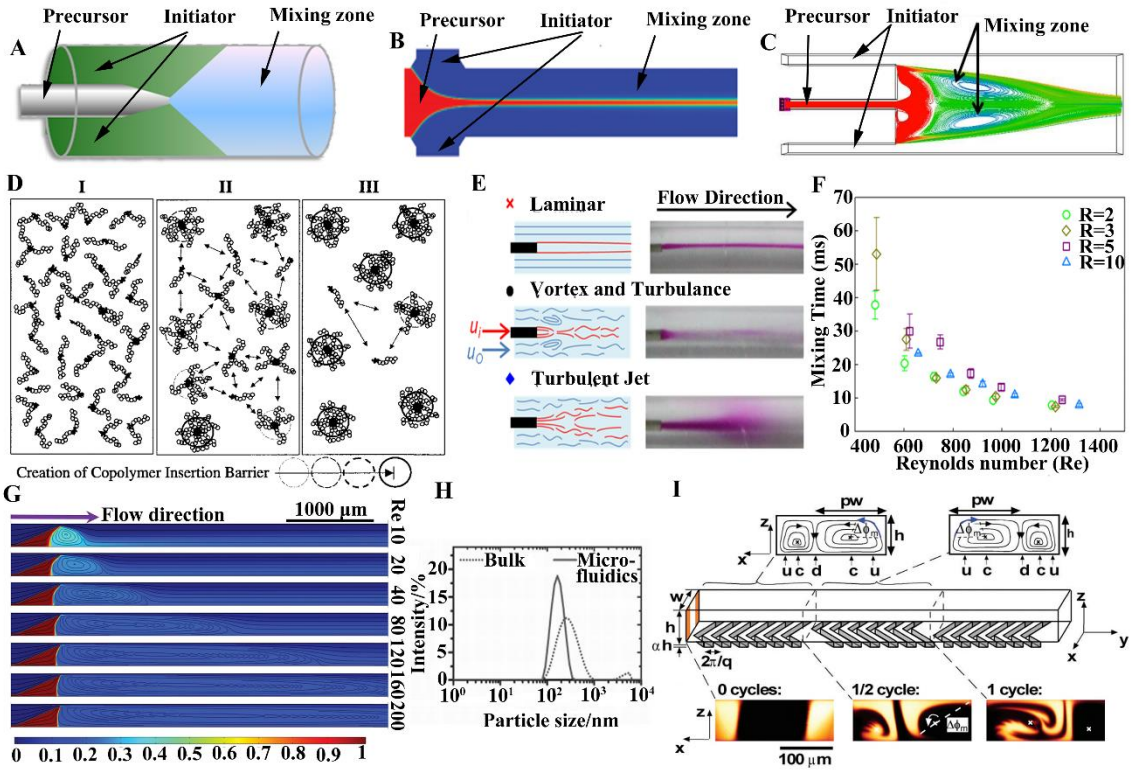

Figure 7. *(A-C) Representative illustration of typical microfluidic chip structures for conducting co-flow nanoprecipitation. (D) Brief illustration of NPs formation starting from (I) well dispersion of the precursor to (II) nucleation and (III) growth, suggesting the significance of fast mixing in producing monodisperse NPs. (E) Graphic and macroscopic illustration of flow pattern transfer with increasing Re. (F) The mixing time can be decreased to milliseconds as Re increases; (G) CFD simulation of enhanced mixing vortex along with increased Re. (H) Production of PLGA NPs by microfluidics showed better polydispersity than the bulk method. (I) Enhancing mixing efficiency at low Re by fabricating complex geometry, such as a herringbone structure. Figure B is reprinted with the permission from Ref. [229], Figure C is reprinted with the permission from Ref. [230], Figure D is reprinted with the permission from Ref. [217], Figure E-F is reprinted with the permission from Ref. [227], Figure G-H is reprinted with the permission from Ref. [228], Figure I is reprinted with the permission from Ref. [231].*

Manipulating Re number in order to enhance the mixing efficiency, it usually needs extra high flow rate to achieve the desired effect, which may be constrained by the maximum force of the fluidic pumps. The other commonly used method is typically based upon smart design of channel geometries.[232] One typical example leveraging this strategy is to prepare nano-liposomes. Complex geometry can decrease the mixing length at relatively low Re, thus increasing the polydispersity of the liposomes as discussed previously, and also ascertaining to obtain uni-lameller vesicles by preventing the lipid bi-layers stacking during the hydration process.[233, 234] Various types of microfluidic chips with complex geometry, such as Tesla-shape, herringbone-shaped, serpentine-shaped and zigzag-shaped channel, were designed and applied for preparing liposomes.[235-237] For example,

herringbone-shaped microchannel containing patterned microgrooves of varying shapes and angles can induce chaotic stirring at a low Re (Re = 10^{-2}–10^{2}) (**Figure 7I**).[231] Previous studies demonstrated that t_{mix} can reduced to ~8 ms at relatively low total flow rate (600 μL/min) by applying this apparatus.[238] However, to fabricate complex geometry, the most commonly used material for preparing the microfluidic chips is polydimethylsiloxane (PDMS), whereas PDMS is not resistant to many organic solvents, which may constrain its potential application for producing NPs.[239]

2.3.2 Microfluidic-assisted production of nanohybrids

Recently, there has been more focus on the incorporating two or more nanomaterials, namely nanohybrids, to achieve increased multifunctionality and create opportunities for the next generation of materials with enhanced in biocompatibility, stability and drug release control.[240] Various nanohybrids with core/shell structures, such as organic/inorganic nanohybrids, inorganic/inorganic nanohybrids and lipid/polymer nanohybrids have been designed and synthesized for DDS fabrication.[37, 241, 242] The conventional two-step method of separately preparing the core structure and the sequential shell coating usually has poor control over the encapsulation efficiency and reproducibility. With the development of microfluidics, a one-step method combining the simultaneous nanoprecipitation of core NPs and shell coating show considerable advantages by reducing intermediate disturbances and batch-to-batch variation.[243]

One of the first trials with potential mechanical explanations was proposed by Karnik *et al.*[243] The aim of the experiment was to fabricate lipid/polymer nanohybrids with PLGA NPs core and lipid outer layers through a microfluidic-assisted single step encapsulation. A co-flow, flow-focusing microfluidic chip was applied with PLGA in acetonitrile as the inner phase and lipid in EtOH/water as the outer phase. They found that this single step nanoprecipitation could form nano-sized (~40 nm) PLGA/lipid core/shell structures. Interestingly, the size of the newly formed nanohybrid was smaller than both bare PLGA and bare liposomes under the same synthesis conditions. They proposed that this phenomenon was due to the fast dispersion of lipid molecules within the mixing medium, rendering the coverage of lipid at the surface of the PLGA core, while the exposed hydrophilic part of lipid further arrested the growth of PLGA NPs. This generated the final nanohybrids with an overall reduced size compared to blank PLGA NPs. A corresponding mathematical simulation and calculation were introduced to prove the hypothesis, and the results showed that the time scale for total homogenization of the medium was around 0.23 ms, at least one an order of magnitude faster than the timescale for PLGA nucleation, suggesting the PLGA nucleation was initiated under a homogenized condition. On the other hand, the time scales of diffusion and binding between lipid and PLGA nucleates were on the same order as PLGA nucleation, indicating the simultaneous lipid coating at the PLGA surface.

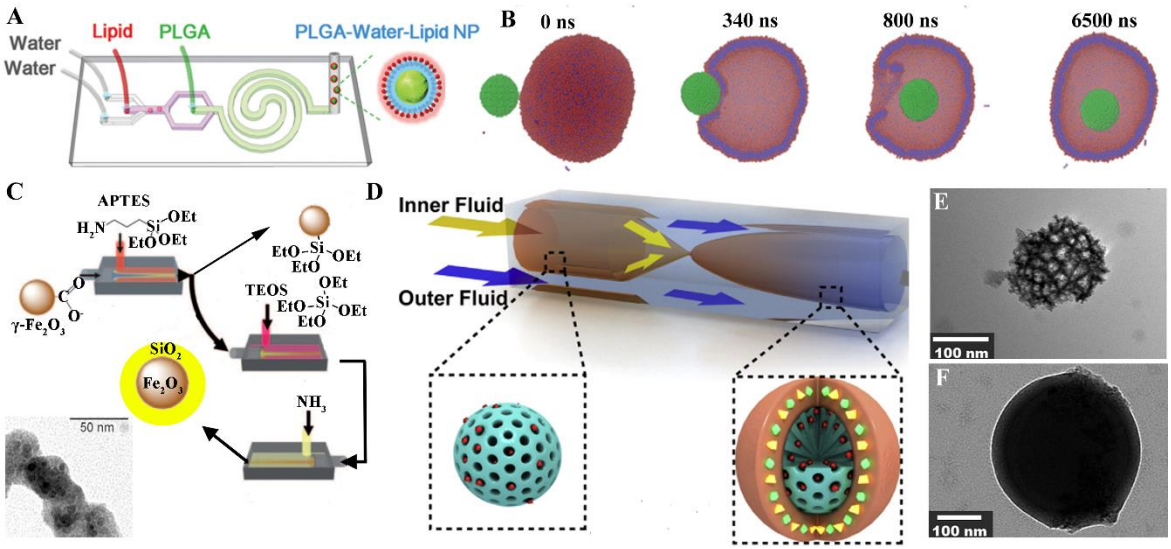

Figure 8. *(A) Schematic illustration of PLGA@Lipid core/shell structure synthesis. (B) Molecular dynamics simulation of the encapsulation process. (C) Graphic illustration of Fe_2O_3@SiO_2 nanohybrid fabrication. (D) Graphic illustration of inorganic@organic core/shell nanohybrids fabrication and the representative transmission electron microscopy (TEM) image of PSi NPs before (E) and after (F) encapsulation. Figures A-B are reprinted with the permission from Ref. [244]. Figure C is reprinted with the permission from Ref. [245]. Figure D-F are reprinted with the permission from Ref. [96].*

This "core nucleation-surface stabilization-shell formation" concept may further be applied to controlled drug loading and release if the "core" is composed of drug nano-crystals. Liu *et al.* developed a microfluidics platform with two consecutive precipitation processes, where the first step precipitation produced drug nano-crystals with fully dissolved polymer, which was precipitated out and coated the drug nano-crystals to form core/shell structures. More specifically, the application of this platform increased the paclitaxel (PTX) loading degree from ~6.7% to 42.6% and sorafenib (SFN) loading degree from 6.2% to 45.2%.[246] More recently, Prud'homme *et al.*, guided by the aforementioned hypothesis of the core/shell formation process, established a mathematical model with the equation $R = \left[K\left(\frac{k_B T {c_{core}}^{5/3}}{\pi\mu\rho c_{BCP}}\right)\right]^{1/3}$, where R is the predicted average aggregate radius for the final nanohybrids, T is the absolute temperature, k_B is the Boltzmann constant, μ is the solvent viscosity, ρ is the bulk density of the core, and c_{core} is the mass concentration of the core material during particle assembly (one-half of the concentration at the beginning), c_{BCP} is the mass concentration of the shell material during particle assembly (one-half of the concentration at the beginning) and K is a single scaling constant with the value 253 $ms \cdot g^{1/3}/m$.[247] This newly established equation was based on the assumption that the time at which particle growth was halted, t_f, was inversely proportional to the surface area of the core structure (proportional to ${c_{core}}^{2/3}$) and the surface area of the shell structure (proportional to c_{BCP}). To confirm this theory, a series of nanohybrids with hydrophilic stabilizer (PEG) containing co-polymer coatings were feasibly fabricated. The yielded size of the nanohybrids matched the size obtained from the equation above, therefore the

importance of this equation is to predict the required formulation composition with a given hydrophobic compound. However, it should be noted that the key parameter within the equation, K, was rather an empirical number obtained from the actual experimental data and the successful prediction may likely be dependent on the stabilizing polymer used. Despite that, considering the most commonly used stabilizer within this study (PEG), this simple and user-friendly equation may show particular significance in biomedical nanohybrids fabrication.

Despite one-step synthesis of organic core/shell nanohybrids, microfluidics can also encapsulate pre-existing NPs to form core/shell nanohybrids. Jiang *et al*. dispersed as-prepared nano-liposomes (40 nm) in aqueous solution as anti-solvent, which precipitated PLGA dissolved in N,N-dimethylformamide (DMF) solution, to prepare PLGA NPs encapsulated nano-liposomes (**Figure 8A**). Computational molecular dynamics simulation was further established to illustrate the encapsulation process (**Figure 8B**).[244] Not only organic NPs, but various inorganic NPs based DDS were also applied to this method to increase the inherent biocompatibility and stability. Cabuil *et al*. established a multi-step continuous synthesis method for fabricating iron oxide@silica core/shell nanohybrids.[245] The (3-aminopropyl)-triethoxysilane (APTES) grafted Fe_2O_3 NPs were co-mixed with tetraethyl orthosilicate (TEOS) in the channel to deposit silica shell on the surface of Fe_2O_3 (**Figure 8C**). Valencia *et al.* provided a facile method to encapsulate quantum dots (QDs, ~5 nm) within lipid matrix by dispersing QDs in organic solution, the flow was further focused by lipid aqueous solution. The generated nanohybrids showed an overall enhanced hydrophilicity, stability in plasma, and an overall improvement in their biocompatibility.[243] Despite smaller metal clusters, such as iron oxide and Au NPs, which usually obtained the size below 10 nm, larger inorganic NPs (~200 nm) such as PSi NPs or copper NPs could also be encapsulated within the polymer matrix. Upon the mixture with the anti-solvent, the precipitation of the polymer was preferably initiated at the surface of inorganic NPs, thus encapsulating the template inorganic NPs (**Figure 8D-F**).[96, 248] Corresponding potential mathematical calculations were also established by Gindy *et al*.[249] Within the study, Smoluchowski diffusion-limited growth kinetics were used to characterize the encapsulation of Au NPs into the polymeric nanoparticles. The given equation, $[P_N] = [P_0^{tot}] \left(\frac{t}{\tau}\right)^{N-1} \left(\frac{t}{\tau}\right)^{-N-1}$, characterizes how the number concentration of produced nanohybrids in solution, P_N, at a settled concentration of shell polymer, P_0^{tot}, changes over time, *t*. Considering P_N can reflect the size of the nanohybrids, the main function of the equation is to predict the size of the produced nanohybrids, whereas another fundamental question, regarding the parameters determining successful encapsulation of the core NPs, has been less investigated. As in most cases, the selected shell materials may not effectively encapsulate the core NPs. In addition, to achieve further multi-functionalities, simultaneous co-encapsulation of two or more types of NPs with altered physiochemical properties within one polymer matrix is also in great demand, yet few papers have demonstrated a single-step co-encapsulation of different NPs at the same time.

3 Aims of the study

A cutting-edge DDS should be capable of recognizing and responding to specific biological microenvironments in a dynamic way, simultaneously releasing the loaded cargo in a controlled manner, and preferably having a synchronous bio-imaging ability with multi-functionalities. This can substantially emphasize the advantages of nanotechnologies and facilitate personalized treatment. Taking advantage of the high capacity of PSi for the loading of both hydrophilic and hydrophobic active compounds, the aim of this dissertation was to develop a series of on-demand PSi based nano-sized DDS for different biomedical applications. Biocompatibility, especially immunogenicity of PSi with different surface chemistry at pre-existing lesion sites were also investigated to better evaluate the feasibility of DDS for clinical use.

The specific objectives of this dissertation were as follows:

1. To fabricate a DOX-loaded DDS with a pH-responsive releasing profile. A dopamine-inspired ligand was synthesized and functionalized PSi, and the drug release was monitored by fluorescence imaging (**I**).

2. To fabricate a PSi-based DDS which would specifically target CA IX over-expressing cancer cells. The pH-responsive DOX release was monitored by FRET (**II**).

3. To fabricate multi-components, multi-functional pH-responsive polymer shell-PSi/Au NPs core nanohybrids by a single-step microfluidics method. Simultaneous encapsulated hydrophobic drug was applied for liver regeneration. Co-resided Au NPs could enhance CT contrasting abilities, thus facilitating liver failure theranostics (**III**).

4. To fabricate a self-regulated nanohybrid with PSi core and polymer matrix outer layer via a single-step microfluidics method with hydrophilic/hydrophobic dual-drugs loading. The development of a close-loop DDS for recapitulated hyperglycemic condition with regulated drug release and facilitated stage-specific diabetic wound healing (**IV**).

5. To investigate the immunogenicity and biological effect of PSi with different surface chemistries under pathological condition, and to further propose the potential mechanism for the phenomenon (**V**).

4 Experimental

Detailed description of the methods, suppliers of the materials and the equipment used in this thesis can be found in the respective original publications (**I**–**V**). The PSi nanoparticles were produced by collaborators at the Laboratory of Industrial Physics, Department of Physics and Astronomy at the University of Turku, Finland.

4.1 Fabrication of the drug delivery carriers

4.1.1 Fabrication of PSi nanoparticles (I–V)

The PSi particles were produced by electrochemical etching of monocrystalline boron–doped *p*+ type Si ⟨100⟩ wafers (Cemat Silicon S.A., Poland) with a resistivity of 0.01–0.02 Ω.cm in a 1:1 (v/v) aqueous hydrofluoric acid (38%)–EtOH electrolyte with a current density of 50 mA/cm^2 in the dark, as described elsewhere.[173] The porous layer was detached from the substrate as a film by increasing the current density to the electro-polishing regime.

For the PSi nanoparticles in publications **I–IV**, thermally hydrocarbonized PSi (THC) films were obtained by heating at 500 °C under 1:1 N_2-acetylene flow for 15 min. undecylenic acid-terminated THCPSi (Un) films were obtained by treating THCPSi films in undecylenic acid at 120 °C for 16 h to obtain terminated carboxylic acid films, adapting the thermal addition process described elsewhere.[250] Next, the Un NPs were prepared by wet-milling in undecylenic acid and then centrifuged to obtain the required PSi NP size.[173, 251]

For the PSi nanoparticles in publication **V**, Un NPs were obtained with the same protocol as described before. Thermally carbonized (TC) PSi films were obtained by heating the THCPSi films absorbed with acetylene at 820 °C for 10 min.[252] Wet ball milling was carried out in 1-decene to reduce the size of the TC PSi multilayer films. Thermal oxidized PSi (TO) was made by exposing the fresh films to ambient air for 2 h at 300 °C, and the NPs were produced by wet ball milling the TO multilayer films in EtOH.[96] After milling, the excess silane was removed by replacing the liquid and redispersing the NPs in fresh toluene and EtOH for at least three times using centrifugation. The size sorting and change of the suspension media was achieved by centrifugation of the Un, TC and TO PSi NPs. The final NPs were dispersed in EtOH.

4.1.2 Fabrication of multifunctional pH-responsive nanocomposites (I)

Firstly, inspired by the structure of dopamine, a derivative of natural flavone quercetin, namely 3-aminopropoxy-linked quercetin (AmQu), was synthesized and the detailed synthetic route can be found in publication **I**. Afterwards, 1 mg of the as-prepared Un NPs were dispersed in 1 mL of anhydrous N,N-dimethylformamide (DMF). After the addition of 8 μL of N-(3-dimethylaminopropyl)-N'-ethylcarbodiimide hydrochloride (EDC) and 6 mg of N-hydroxysuccinimide (NHS), the solution was stirred overnight. Then 5 mg of AmQu was dissolved in 1 mL of anhydrous DMF and mixed with the solution to react for

24 h. The AmQu-UnTHCPSi was thoroughly washed three times with DMF to remove the electrostatically adsorbed AmQu, and then stored for further use. AmQu-UnTHCPSi NPs containing 1 mg of UnTHCPSi were then re-dispersed in 2 mL of ethanol, followed by the addition of 1.43 mg of $Fe(NO_3)_3 \bullet 9H_2O$. The resulting mixture was stirred for 24 h. Finally, the Fe^{3+}-AmQu-UnTHCPSi (FAP) particles were centrifuged, washed three times with EtOH, and dispersed in EtOH for subsequent usage.

4.1.3 Fabrication of multifunctional hypoxia-targeting nanocomposites (II)

Initially, a specific carbonic anhydrase IX (CA IX) targeting ligand VD11-4-2 was synthesized for further modification.[253] Un NPs (1 mg) were dispersed in anhydrous DMF (1 mL). EDC (8 μL) and NHS (6 mg) were added in the solution and stirred for 2 h. Then, 5 mg of NH_2-PEG-NH-tert-butyloxycarbonyl (Boc, Iris Biotech, Germany) was dissolved in 1 mL of anhydrous DMF and mixed with the solution to react for 24 h. The Boc-NH-PEG-Un was thoroughly washed three times with DMF and then redispersed in 3 mL of CH_2Cl_2 (DCM) containing 1.8 mL of trifluoroacetic acid (TFA). The solution was stirred for 3 h to remove the Boc protection. Then NH_2-PEG-Un particles were washed with saturated $NaHCO_3$, dd-H_2O, EtOH, and DCM, once with each, and finally redispersed in 1 mL of toluene. Dry toluene (2 mL), VD11-4-2 (1 mg), and N,N'-Carbonyldiimidazole (CDI, 0.4 mg) were added to a 10 mL round-bottom flask fitted with a dry argon (Ar) inlet and magnetic stirrer and heated to 60 °C with stirring for 3 h. The as-prepared NH_2-PEG-Un was then added drop-wise. The solution was left to stir at 60 °C overnight to obtain the final VD11-4-2-PEG-Un (further described as VD-PSi). Particles were washed three times with ethanol and stored in ethanol for further usage.

4.1.4 Fabrication of microfluidic flow–focusing device (III–IV)

Microfluidic flow-focusing devices were fabricated by assembling borosilicate glass capillaries on a glass slide (publications **III** and **IV**). One end of the cylindrical capillary (World Precision Instruments, Inc.), with inner and outer diameters of around 580 and 1000 μm, respectively, was tapered using a micropipette puller (P-97, Sutter Instrument Co., USA) to a diameter of 20 μm; this diameter was further enlarged to ca. 80 μm using a sand paper. This cylindrical tapered capillary was inserted into the left end of the cylinder capillary with inner dimension of around 1100 μm (Vitrocom, USA), and then coaxially aligned. A transparent epoxy resin (5 Minute® Epoxi, Devcon) was used to seal the capillaries. Two immiscible liquids were injected separately into the microfluidic device through polyethylene tubes attached to syringes at selected flow rates with constant flow. The flow rate of the different liquids was controlled by syringe pumps (PHD 2000, Harvard Apparatus, USA).

4.1.5 Fabrication of pH-responsive PSi/ Au nanohybrids (III)

pH-responsive biocompatible polymers AcDEX and spermine AcDEX were prepared by reversibly modifying dextran with acetal–protecting groups, as described in publication **III**. To achieve single-step co-encapsulation of different NPs simultaneously, prior to the

encapsulation, both PSi and Au NPs were modified to alter the surface properties. The Au NPs were initially synthesized with dodecanethiols as the capping monolayer (Nanoprobe, USA). To further conjugate the Au NPs onto spermine AcDEX, the Murray place exchange method was carried out to functionalize the Au NPs with a desired ligand. Briefly, 2 mg of Au NPs were mixed with a solution of 20 μL of 3-mercaptopropionic acid and 1 mL of TEA in EtOH. The mixture was stirred under argon at room temperature for 4 h and was then dried under vacuum. The black precipitation was further re-dispersed in DMF. Next, as-prepared Au-COOH was added in 12 mg of NHS and 16 μL of EDC. After stirring for 1 h, 100 mg spermine AcDEX was subsequently added and left to react overnight. The reaction was terminated by adding 4 mL of dd-water and the product was collected by centrifugation, and washed by EtOH 3 times. The spermine AcDEX modified Au NPs (DAu) solution was redispersed in EtOH for further use. 1 mg of the as-prepared Un NPs were dispersed in 1 mL of anhydrous DMF. After the addition of 8 μL of EDC and 6 mg of NHS, the solution was stirred overnight. Then 50 mg of as-prepared spermine AcDEX was dissolved in 1 mL of anhydrous DMF and mixed with the solution to react overnight. The spermine AcDEX modified Un NPs (DPSi) were thoroughly washed three times with EtOH to remove the electrostatically adsorbed spermine AcDEX, and then stored for further use. For the preparation of DPSi, DAu encapsulated nanohybrids (DPSi/DAu@AcDEX), a microfluidic 3D co-flow focusing glass capillary device was used at room temperature. DPSi (0.5 mg/mL), DAu (2.5 mg/mL) were dispersed into the AcDEX (10 mg/mL) EtOH/acetonitrile (90:10, v/v, with 0.2% TEA) co-solvent solution with a desired concentration, which together served as the inner fluid; the outer fluid was composed of 1% Poloxamer-188 (P-188) solution. The inner (1 mL/h) and outer (20 mL/h) fluids were separately pumped into the microfluidic device, in which the inner fluid was focused by the continuous outer fluid. In this procedure, water insoluble AcDEX self-assembled into the nanocarriers during diffusion from the organic solution into water, and thus, the nanohybrids (DPSi/DAu@AcDEX) were obtained.

4.1.6 Fabrication of close-loop nanohybrids loaded with collagen ark (IV)

A phenylboronic acid ester (PAE) containing oxidative responsive polymer (POD) was first synthesized by conjugating 4-(hydroxymethyl)-phenylboronic acid pinacol ester on oxidized dextran, where dextran was oxidized with sodium periodate. The detailed synthesis routine can be found in publication **IV**. POD cannot fully dissolve in the preferred solvent. Therefore, prior to the experiment we dispersed 30 mg of POD in 1 mL of EtOH/H_2O co-solvent (80/20, v/v). After bath sonicating for 10 min, the sample was centrifuged and the supernatant with a POD concentration of 15 mg/mL was collected. For the preparation of PSi encapsulated nanohybrids (PSi@POD), a microfluidic 3D co-flow focusing glass capillary device was used at room temperature. PSi (1 mg/mL) was dispersed into the POD (15 mg/mL) EtOH/H_2O (80/20, v/v) co-solvent solution with a desired concentration, which served as the inner fluid; the outer fluid was composed of dd-H_2O (pH = 7.2). The inner (1 mL/h) and outer (10 mL/h) fluids were separately pumped into the microfluidic device, in which the inner fluid was focused by the outer continuous fluid. In this procedure, water insoluble POD self-assembled into the nanocarriers during diffusion from the organic solution into water, and thus, the nanohybrids (PSi@POD) were obtained. Afterwards, 10

μg of GOx was added in 10 mL of as-prepared PSi@POD solution and stirred overnight to initiate the Schiff-base facilitated protein conjugation, resulting in the production of close-loop glucose responsive nanohybrids. The as-prepared nanohybrids were then embedded on a water-insoluble collagen patch with the diameter of 1 cm × 1 cm × 0.4 cm (l/w/h) to obtain the final nanohybrids/patch composites.

4.1.7 Dual-drug loading for different nanoparticles (I–IV)

For PSi-based NPs in publication **I**, a certain amount of Fe^{3+}-AmQu-UnTHCPSi (FAD) containing 100 μg of Un was mixed with 200 μg of DOX in 1.0 mL of PBS (pH 7.4), and stirred at room temperature overnight. The mixture was centrifuged and washed three times with 6.7 mM PBS (pH 7.4).

For PSi-based NPs in publication **II**, a certain amount of VD-PSi and PSi particles containing 1 mg of PSi was dispersed into 2 mL of PBS buffer at pH-value 7.4, and then 3 mg of DOX was added and stirred overnight. After the drug loading, the particles were collected by centrifugation and prepared for further studies.

For PSi-based nanohybrids in publication **III**, prior to the microfluidics assisted nanoprecipitation, 1 mg of DPSi was immersed in 0.5 mL of a dimethyl sulfoxide (DMSO) solution containing the hydrophobic drug XMU-MP-1 at a concentration of 50 mg/mL. Then, the particles were collected by centrifugation and washed with dd-H_2O for three times and re-dispersed into AcDEX solution for further encapsulation.

For PSi-based nanohybrids in publication **IV**, both hydrophobic (atorvastatin, ATO) and hydrophilic (deferoxamine, DFO) drugs were loaded in the nanohybrids. For ATO loaded nanohybrids, 4 mg/mL of PSi was mixed with 20 mg/mL of ATO methanol solution overnight The ATO-loaded particles were then collected through centrifuge and the residual methanol on the particle surface was gently washed away with dd-H_2O. Afterwards the drug-loaded PSi were dispersed in POD solution at corresponding concentrations and encapsulated by microfluidic-assisted nanoprecipitation, as described previously. To construct DFO, ATO dual-drug loaded nanohybrids, 100 μg of DFO and 10 μg of GOx were added in 10 mL of as-prepared ATO-encapsulated PSi@POD solution and stirred overnight to initiate the Schiff-base facilitated drug conjugation.

4.2 Characterization of the fabricated carriers

4.2.1 Physiochemical characterization of the nanoparticles (I–V)

The porous properties of the PSi particles were studied using N_2 adsorption/desorption (publications **I**–**V**). The surface area and pore characteristics of the particles were determined by Brunauer–Emmet–Teller and Barret–Joyner–Halenda theories.[254]

The chemical structures of the synthesized small molecules or polymers were confirmed by ^{1}H NMR (publications **I**–**IV**) or ^{13}C NMR (**I**) (AVANCE III, Bruker, Switzerland). The H_2O_2 dependent polymer degradation (publication **IV**) was confirmed by ^{1}H NMR.

Nanoparticle size measurements (publications **I**–**V**) were performed using DLS with Zetasizer NanoZS (Malvern Instruments Ltd., UK). For each measurement, the sample was loaded in a disposable polystyrene cuvette (SARSTEDT AG & Co., Germany). The

nanocarrier surface zeta-potential (ζ-potential) was measured with Zetasizer NanoZS using disposable folded capillary cells (DTS1070, Malvern, UK). Particle stability in human plasma (publication **II**) was investigated by incubating the NPs with human plasma at 37 °C for 2 h. Samples were withdrawn at different time intervals and diluted several times with water before measuring the average particle size and ζ-potential (Zetasizer Nano ZS, Malvern Instruments, UK). Anonymous donor human plasma was obtained from the Finnish Red Cross Blood Service.

The structures of the fabricated nanocarriers (publications **I**–**V**) and the glucose dependent particle degradation (publication **IV**) were evaluated by transmission electron microscopy (TEM, Tecnai 12, FEI Company, USA) at an acceleration voltage of 80 kV. The TEM samples were prepared by depositing 2 µL of the nanocarrier suspension with proper concentrations onto carbon-coated copper grids (300 mesh; Electron Microscopy Sciences, USA).

The morphology and surface topography of the nanohybrids/patch composites (Publication **IV**) were evaluated by SEM. The images were taken using a Hitachi S-4800 (SEM, Hitachi, Japan).

The qualitative analysis of the surface modification and interaction (publications **I**–**IV**) of the NPs were determined by Fourier transform infrared spectroscopy (FTIR) with a Vertex 70 spectrometer (Bruker Optics, USA), using a horizontal attenuated total reflectance (ATR) accessory (MIRacle, PIKE Technologies, USA). The spectra were recorded between 4000 and 500 cm^{-1} with a 2 cm^{-1} resolution.

The surface modification (publication **II**) or residence of different particles in the polymeric matrix (publications **III** and **IV**) were confirmed by energy dispersive X-ray (EDX) spectroscopy or EDX mapping (Oxford INCA 350 EDX, Oxford, UK).

Quantitative AmQu conjugating efficacy, iron chelating efficiency and the iron leakage content (publication **I**) were measured by spectrophotometric method with UV-1600PC spectrophotometer (VWR, U.S.A) or Varioskan Flash fluorometer (Thermo Fisher Scientific, USA).

4.2.2 Quantification of the payloads (I–V)

For publications **I** and **II**, the quantification of the model compounds, the loading degree and drug release were evaluated by fluorospectrophotometric method, using a Varioskan Flash fluorometer (Thermo Fisher Scientific, USA), while for publication **III** it was done by high performance liquid chromatography (HPLC, Agilent Inc., USA). For publication **IV**, HPLC was used for quantifying ATO and a spectrophotometric method was used for DFO. Detailed description of the HPLC experimental setup and conditions used can be found in the respective original publications (**I**–**IV**).

The fluorescence quenching (publication **I**) or FRET (publication **II**) phenomena caused by the interaction between the NPs and the loaded drug were analyzed by fluorospectrophotometric methods.

4.2.3 *In vitro* drug release (I–V)

For publications **I** and **II**, the *in vitro* drug release was performed at 37 °C in sink conditions by immersing different NPs in dissolution media with different pH-values (7.4 or 5.0). The samples were placed on a shaking plate with a shaking speed of 200 rpm. 100 µL of samples were withdrawn from each dissolution test at different time points. The collected samples were centrifuged at 16,000*g* for 5 min and the fluorescence intensity of the supernatants was measured.

To measure the AmQu cleavage from FAP (publication **I**), AmQu-modified UnTHCPSi with a concentration of 50 µg/mL was suspended in a solution with 0.5 mg/mL crude protease from bovine pancreas in 2 mL of 6.7 mM PBS (pH 7.4) at 37 °C under constant stirring. The solution pH was adjusted by titration with 1.0 M of HCl and/or 1.0 M of NaOH to obtain pH-values of 5.0 and 7.4, respectively. Following 8, 12, 20, and 24 h of incubation, the NP suspensions were centrifuged to isolate the NPs from the cleaved AmQu, PBS, and protease solutions. The AmQu cleaved from the NPs was then quantified with UV-spectroscopy at a wavelength of 360 nm.

The *in vitro* release of XMU-MP-1 from the DPSi/DAu@AcDEX (publication **III**) was evaluated in PBS at pH-values of 7.4 and 5.0 in sink conditions. Due to the low solubility of XMU-MP-1, amphiphilic P-188 (5%, w/v) was added to all the release media. The drug-loaded nanohybrids containing 50 µg of DPSi were added to buffer solutions using a shaking plate method at 250 rpm and 37 °C. At each time point, 100 µL of releasing medium was centrifuged (4 min, 5,000*g*) and the supernatant was collected. Then, the same amount of preheated medium was added back along with the centrifuged particles to replace the withdrawn volume. The concentration of free drugs at each time point was quantified by HPLC. Cellular release of XMU-MP-1 from macrophage cells KG-1 was measured by dispersing NPs into free IMDM medium or IMDM medium containing 0.5×10^6 KG-1 macrophage cells. At each time point, 50 µL of the medium was withdrawn and centrifuged (4 min, 5,000*g*) to remove the particles and macrophages. The supernatant was then diluted with 50 µL of DMSO to remove the protein binding. The free drug concentration was subsequently measured by HPLC. The same amount of preheated medium was added back along with the centrifuged particles (or the particles together with macrophage cells) to replace the withdrawn volume. After 5 h, the medium containing particles or particles per macrophage cells were centrifuged (5 min, 200*g*) and the supernatants removed. The residue was lysated by DMSO (tip sonication for 1 min). After centrifugation (5 min, 16,000*g*), the supernatant was collected and measured by HPLC. The amount of XMU-MP-1 within the macrophage cells was calculated as $W = W_{m+p}\ W_p$, where W is the amount of drug within the macrophage cells, W_{m+p} is the amount of the drug in the sample containing both macrophage cells and particles, and W_p is the amount of drug in the sample only containing the particles.

The glucose dependent release profiles of nanohybrids/patch composites (publication **IV**) were evaluated with Transwells (Costar 3401, Corning Inc. USA). The particle embedded patch (containing 300 µg of PSi) was added to the upper chamber and the donor chamber was filled with 3 mL of corresponding PBS buffer, containing 0, 1 or 4 mg/mL of glucose. Free drugs embedded in the patch were used as controls. A 100 µL sample was collected for ATO quantification, and 200 µL samples were collected for DFO

quantification at each time-point, after which 300 μL of pre-heated releasing buffer was added in each well.

4.2.4 Cell lines and culture (I–V)

Human breast cancer cells (MCF-7, publications **I** and **II**), human hepatocellular carcinoma cells (HepG2, publications **III** and **V**), human bone marrow acute myelogenous leukemia macrophages (KG-1, publication **III**), human umbilical vein endothelial cells (HUVECs, publication **IV**), human dermal fibroblast cells (Fibroblasts, publication **IV**) and murine leukemic monocyte macrophage cells (RAW 264.7 macrophages; publication **V**) were selected for the *in vitro* studies (all from American Type Culture Collection, USA). The MCF-7, HepG2, Fibroblasts and RAW 264.7 macrophages were cultured in Dulbecco's modified Eagle's medium (DMEM, EuroClone S.p.A., Italy) with 4.5 g/L glucose, supplemented with 10% fetal bovine serum (Gibco, Invitrogen, USA), 1% nonessential amino acids, 1% L-glutamine, penicillin (100 IU/mL), and streptomycin (100 mg/mL) (all from HyClone, USA). For the KG-1 cells, Roswell Park Memorial Institute 1640 medium was used instead of DMEM for cell culturing. For HUVECs, medium 200 (M200) was used with 1× low serum growth supplement (LSGS, Thermal Fisher, USA) for cell culturing. The cell cultures were maintained in a standard incubator (BB 16 gas, Heraeus Instruments GmbH, Germany) at 37 °C with an atmosphere of 5% CO_2 and 95% relative humidity. Prior to each test, the cells were harvested with trypsin (0.25%, v/v)–ethylenediaminetetraacetic acid PBS.

DOX-resistant MCF-7 cells (MCF-7/DOX^R, publication **I**) were cultured with sequential exposure of MCF-7 cells to 1–10 μg/mL of free DOX.[255] Each concentration of DOX (from low to high concentrations) was added to MCF-7 for one day, and the cells were incubated in DMEM medium without DOX for 4 days, followed by repeating the same treatment twice and moving to the next higher concentration cycle.

4.2.5 Cellular viability of the fabricated carriers (I–V)

The cellular viability of the prepared carriers with and without loaded drugs was evaluated using luminescence- based cell viability assays (publications **I**–**V**). The assay was conducted in 96-well plates (PerkinElmer Inc., USA) and certain amounts of different types of cells were seeded in these plates. After the cell attachment and removing of the culture media, the wells were washed twice with 1×HBSS (pH 7.4) prior to the addition of the fabricated carriers with a series of concentrations, and then incubated for the desired exposure times. All assays were conducted at least in triplicate.

In publication **III**, to simulate the bio-fate of NPs within the liver, another method was carried out. Different concentrations of XMU-MP-1 loaded DPSi/DAu@AcDEX (10, 25, 50, and 100 μg/mL, DPSi/DAu@AcDEX concentration) and free DPSi, free DAu, free XMU-MP-1, free AcDEX, and free DPSi/DAu@AcDEX NPs at corresponding concentrations, were incubated with 1×10^4 KG1 macrophage cells overnight. Then the macrophage cells were harvested by centrifuge (900*g*, 5 min). The macrophages treated with different drugs were re-suspended in medium and added to 96-well plates, where

HepG2 cells were seeded with a density of 2×10^4 cells per well. After 24 h of co-incubation the viability of different groups was evaluated, as described previously above.

4.2.6 Embedding TEM images (I)

For the embedding TEM experiments, the following protocol was followed. After the particle–cell interaction studies, the PSi suspension was carefully removed and the cells were fixed with glutaraldehyde (2%, w/w) in PBS (pH 7.4, 0.1 M) for 30 min at room temperature. The wells were then washed twice with sodium cacodylate buffer (NaCac) for 3 min. Afterwards, the cells were post-fixed with 1% osmium tetroxide in NaCac buffer (pH 7.4, 0.1 M) and then dehydrated and embedded in epoxy resin. Ultrathin sections (60 nm) were cut perpendicular to the insert, post-stained with uranyl acetate and lead citrate, and examined with TEM using an acceleration voltage of 120 kV.

4.2.7 Flow cytometry investigation (I, II, V)

For publication **I**, MCF-7 or MCF-7/DOX^R Cells (2.0 mL per well) were separately seeded in 6-well plates at concentration of 2.5×10^5 cells/mL. Following 24 h of cell attachment to the wells, the cells were first rinsed three times with 1× HBSS (pH 7.4) and then incubated with free DOX or DOX@FAP (1 mL, 23 μg/mL, DOX concentration equivalent) for 3 h. Then, the samples were removed and the wells washed three times with 1× HBSS (pH 7.4), and subsequently cultured for another 4 h. After washing with 1× HBSS (pH 7.4), the cells were harvested and fixed with 2.5% glutaraldehyde or 4% of paraffinaldehyde in 1× 6.7 mM of PBS (pH 7.4) for 30 min at room temperature. For publication **II**, 100 μg/mL of DOX loaded VD-PSi was dispersed in a medium with or without cobalt chloride. The following protocol was the same as described above. Exactly 10,000 events were collected on a LSR II flow cytometer (BD Biosciences, USA) with a laser excitation wavelength of 488 nm using FACS Diva software. For publication **V**, RAW 264.7 macrophage cells were separately seeded in 12-well plates at a concentration of 5×10^5 cells per well. Following cell attachment to the wells, the cells were incubated with 10 pg/mL of IFN-γ and 1 μg/mL lipopolysaccaride (LPS) for 4 h. Then the cells were washed with 1× PBS (pH 7.4) and 0.5 mL of 10 μM 2',7'-dichlorodihydrofluorescein diacetate (DCFH-DA) was added. After 1 h, the medium was removed and cells were washed with 1× PBS (pH 7.4) for 3 times followed by adding 2, 10, 20 and 50 μg/mL of each PSi sample. After 24 h, the cells were collected and measured, as described above.

4.2.8 *In vitro* fluorescence confocal imaging (I-II)

Suspensions of cells (1×10^5 cells per well) were seeded in Lab-Tek™ Chamber Slides (Thermo Fisher Scientific, USA). After 24 h of cell attachment to the wells, Alexa-Fluor® 633 (Alexa-633) labeled nanocarriers were added into the wells. Following 2 h incubation, the samples were removed and the wells were washed three times with 1×HBSS (pH 7.4), following culture in DMEM medium with another 0 or 4 h. Afterwards, the medium was removed and the wells were washed three times. Cells were fixed with glutaraldehyde (2.5%,

w/v) in 1× 6.7 mM of PBS (pH 7.4) for 30 min at room temperature and DAPI (Thermo Fisher, USA) with a concentration of 2.8 μM was added for cell staining (publication **I**).

Suspensions of cells (1×10^5 cells per well) were seeded in Lab-Tek Chamber Slides (Thermo Fisher Scientific, USA). After 24 h of cell attachment to the wells, the cells were cultured with $CoCl_2$ containing medium for 24 h to create hypoxia conditions. Afterwards, the cells were rinsed three times with 1×HBSS (pH 7.4), and particles containing 100 μg/mL PSi were added into the wells. After 3 and 24 h incubation, the samples were removed and the wells were washed three times with 1× HBSS (pH 7.4). CellMask DeepRed (Life Technologies, USA) was used to stain the cell membranes by incubating the cells at 37 °C for 3 min. Then the cells were washed twice with buffer and fixed with 2.5% glutaraldehyde at room temperature for 20 min. The cells were again washed twice with 1× PBS buffer and stored in 2 mL buffer (publication **II**).

4.2.9 CA IX expression and binding study (II)

An immunofluorescence study was carried out to confirm the CA IX expression within hypoxia conditions. MCF-7 cells were grown on glass coverslips and incubated under normoxic and hypoxic conditions. After 48 h, cells were fixed with cold methanol. Nonspecific binding was blocked by incubation with PBS containing 2% bovine serum albumin (BSA) and 2% FBS. Cells were incubated with CA IX-specific monoclonal antibody (mAb) M75 (BioScience, Slovakia) at a concentration of 1:100 for 1 h and then incubated with goat antimouse AlexaFluor 488-conjugated IgG antibody (Life Technologies, USA) for 1 h. DAPI was used to stain the nuclei. Cell immunofluorescence was imaged with Invitrogen EVOS FL Auto Imaging System (Thermo Fisher Scientific, USA). ImageJ was used for the quantitative evaluation of fluorescence intensity of FITC labeled secondary CA IX antibody in three hypoxic (59 cells in total) and normoxic (53 cells in total) images.

Fluorescent thermal shift assay was carried out to determine protein−ligand binding. Stopped-flow kinetics CO_2 hydration assay was performed using Applied Photophysics SX.18MV-R stopped-flow spectrometer. Reaction velocities were measured by recording the absorbance of phenol-red indicator (30 μm, $\lambda = 557$ nm). A saturated CO_2 solution was prepared by bubbling the gas in Milli-Q water at 25 °C for 1 h. Serial dilutions with 16 concentrations of VD11-4-2 compound; PEG-PSi and VD-PSi particles were prepared and used for testing the inhibition. Protein CA IX preparation and purification were reported previously.[253] Samples containing 20 μM CA IX, 0−2 μM ligand (or 0−75 μM particles), 20 mM of HEPES with 100 mM of NaCl, and 60 μm phenol red at pH 7.5, 10% of FBS, and 2.5% of EtOH were incubated for 1 h at 25 °C and then used for the stopped-flow experiments. Equal volumes of the protein sample and CO_2 saturated water were mixed and the reaction was observed. Samples without protein (spontaneous CO_2 hydration) and samples of protein without any inhibitor were used as zero and full activity controls, respectively. The K_d values were determined using the Morrison model for tight binding inhibitors.[256]

4.2.10 *In vitro* western blot analysis (III)

HepG2 cells (2.0 mL per well) were separately seeded in 6-well plates at a concentration of 5×10^4 cells/mL. After overnight cell attachment to the wells, free XMU-MP-1 (1, 3, and 10 μM dissolved in DMSO), and MP@DPSi/DAu@AcDEX (containing the same corresponding concentration of XMU-MP-1), DPSi/DAu@AcDEX (containing DPSi at the corresponding concentration) were added in the cells. DMSO or H_2O_2 were added as negative and positive controls, respectively. Cells were harvested at 0.5, 3, 6 or 12 h for further analysis.

Cell samples were prepared in ice-cold lysis buffer containing 1% Tritonax-100, 50 mM Tris-HCL(pH 7.4), 10% glycerol, 150 mM NaCl, 2 mM EDTA, 50 mM NaF, 10 mM Na_3VO_4, complete Mini protease inhibitor mixture tablet (Roche), and 2 mM phenylmethanesulfonyl fluoride. Total protein contents were determined by a BCA Protein Assay Kit (Pierce). Lysate corresponding to 20 μg of total protein was subjected to sodium dodecyl sulfate polyacrylamide gel electrophoresis (SDS-PAGE) using 4–10% of gradient gel, and transferred to polyvinylidene fluoride membranes (100 V, 90 min).

The proteins were identified by immunoblot analysis with the appropriate primary antibodies at a dilution of 1:1000 (or as otherwise stated below). Anti-GAPDH (2118, Cell Signaling), anti-MOB1 (13730, Cell Signaling), anti-phospho-MOB1 (Thr35) (8699, Cell Signaling), anti-YAP (14074, Cell Signaling), anti-phospho-YAP (S127) (4911, Cell Signaling), anti-MST1 (3682, Cell Signaling), anti-MST2 (3952, Cell Signaling). Horseradish peroxidase-conjugated antibody to Rabbit IgG (7074) (1:3000 dilution for each) were purchased from Jackson ImmunoResearch Laboratories. The protein brands were visualized with a SuperSignal West Pico Kit according to the manufacturer's instructions (Thermo Fisher Scientiftic Pierce, USA)

4.2.12 *In vitro* PSi degradation study (V)

To evaluate *in vitro* PSi degradation kinetics, 150 μg of different PSi were incubated in 3 mL of 1% Poloxamer 188 PBS buffer (pH 7.4) with or without 3-morpholinosydnonimine (SIN-1, 2 mM), under orbital agitation of 100 rpm at 37 °C. At designated time intervals, aliquots were sampled and replaced with fresh corresponding degradation buffer. The resulting liquid was stored at 4 °C for later analysis of total silicon by Microwave Plasma-Atomic Emission Spectrometer (Varian Inc. Santa Clara, CA, USA; MP-AES).

4.2.13 *In vitro* q-PCR (V)

RAW 264.7 macrophage cells were seeded in 6-well plates at a concentration of 1.5×10^5 cells per well. After incubating overnight, the cells were treated with PSi at concentrations of 20 μg/mL. After incubating for 1.5 h, the cells were harvested and total RNA was isolated in the presence of Trizol Reagent (Sigma-Aldrich, USA), according to the manufacturer's protocol. The concentration and purity of the RNA preparations were determined by the absorbance of RNA at 260 and 280 nm. cDNA was synthesized using the TransScript One-Step gDNA Removal and cDNA Synthesis SuperMix (Transgen Biotech, China), according to the manufacturer's instructions. Gene expression was detected using a SYBR Select

Master Mix (Thermo Fisher, USA) and an ABI Step One Plus Real-Time PCR System. The mice primer sequences used in the polymerase chain reaction were shown as follows: TNF-α: 5' - CAG CCT CTT CTC ATT CCT GCT TGT G - 3', 5' -CTG GAA GAC TCC TCC CAG GTA TAT - 3'; CXCL1: 5' - AGC TTC AGG GTC AAG GCA AG - 3', 5' - CTG CAC CCA AAC CGA AGT - 3'; CCL2(MCP-1): 5' - AGG TGT CCC AAA GAA GCT GTA - 3', 5' - ATG TCT GGA CCC ATT CCT TCT - 3'; IL-6: 5' - TAG TCC TTC CTA CCC CAA TTT C - 3', 5' -TTG GTC CTT AGC CAC TCC TTC - 3'; IL-1β: 5' - GAA ATG CCA CCT TTT GAC AG - 3', 5' - CCA CAG CCA CAA TGA GTG AT- 3'.

4.3 *In vivo* evaluation of the fabricated carriers

4.3.1 Animal model establishment and treatment process (III–V)

All experiments involving animals were performed in compliance with guidelines under the Institutional Animal Care and Use Committee at Experimental Animal Centre in Xiamen University, China. Acetaminophen (APAP) induced acute liver failure (ALF) or acute liver inflammation (ALI) mice models were correspondingly established in publications **III** and **V**. Eight- to ten-week-old male C57BL/6 mice were randomly allocated to different groups, further administered with APAP (Sigma) via oral gavage after 20 h of starvation. APAP was used at a sub-lethal dose of 200 mg/kg for the liver injury study. The treatment initiated at 2.5 h post APAP gavage. For publication **III**, five mice per group received twice a day *i.v.* injections of 15% Solutol® HS 15 (control), DPSi/DAu@AcDEX loading XMU-MP-1 (0.1 or 0.5 mg/kg), XMU-MP-1 (0.1 or 0.5 mg/kg, dispersed in 15% of Solutol® HS 15) or the blank DPSi/DAu@AcDEX control at the corresponding concentration at the indicated times post-APAP administration. For publication **V**, 3 h post ALF model establishment, the mice were separately *i.v.* injected with 0.3 or 3 mg/kg of TO, TC and Un (which were referred to as TO L, TO H, TC L, TC H, Un L and Un H), saline was injected as a control.

The streptozotocin (STZ) induced diabetic model and the following diabetic wound mice model were established in publication **IV**. Male C57BL/6 (20-25 g) mice were treated with high fat diet for 4 weeks before the induction of diabetes. Afterwards the mice were intraperitoneally (*i.p.*) injected with STZ (Sigma-Aldrich, US) to induce pancreatic islet β-cell death. Mice were fastening for 18 h and then weighed prior to injections. STZ was freshly dissolved in dilution buffer (0.1 M sodium citrate, pH 4.5, with HCl, stored at 4 °C) and filter sterilized. To induce diabetes, the mice were given 0.1 mL *i.p.* injections of 50 mg STZ per kg of body weight for 5 consecutive days. All the mice were fed a high fat diet during the process. Blood glucose levels were measured daily beginning 5 days after the second *i.p.* injection. Blood glucose levels were measured for each mouse, and a mouse was considered diabetic after two consecutive readings of more than 250 mg/dL blood glucose. The diabetic mice were anesthetized with isoflurane and the hair on their backs was shaved and completely removed with depilatory cream. After disinfection with alcohol swabs, one wound was gently outlined by a marked 6 mm punch biopsy (Acuderm, Fort Lauderdale, FL). Following the outline, full-thickness wounds were made using a McPherson-Vannas Micro Scissor (World Precision Instruments, Sarasota, FL). The mice were randomly divided into 4 groups (n = 5): (1) blank PSi@POD embedded in collagen patch (CP); (2) free agents (including ATO, DFO and GOx) embedded in collagen patch (CF); (3) ATO

and GOx loaded PSi@POD embedded in collagen patch (PA); and (4) ATO, DFO and GOx loaded PSi@POD embedded in collagen patch (PAD). Wounds were further covered with Tegaderm and coban. The animals were individually caged, and the various treatments were reapplied every 3 days. Wounds were photographed with a digital camera, and the wound area was calculated with Image J.

4.3.2 Histological analysis (III–V)

For publication **III**, the mice were sacrificed at 12, 24 and 72 h post treatment, and the dissected liver tissues were fixed in buffered formalin, embedded in paraffin, and then processed for tissue-section staining with hematoxylin–eosin (H&E). Transferase-mediated deoxyuridine triphosphate-biotin nick end labelling (TUNEL), C-X-C chemokine receptor type 4 (CXCR-4) assays were performed according to the manufacturer's instructions, using the Apoptag Peroxidase in Situ Apoptosis Detection Kit (Millipore). The rest of the tissues were snap frozen in liquid nitrogen and subsequently stored at −80°C.

For publication **IV**, wounds were harvested on days 7 and 14 with a 3 mm rim of unwounded skin for histological analysis. The samples were fixed in 4% paraformaldehyde overnight, embedded in paraffin and then sectioned (5 μm slabs(?)). The length of the new epidermis was used to evaluate the wound healing conditions after H&E staining. Ki-67 staining was used to investigate the regeneration process at days 7 and 14. ZEISS Axioskop microscope was used for capturing digital photographs and Image J software was used to evaluate the wound healing process.

For publication **V**, the mice were sacrificed at 48 h post PSi administration and the liver tissues were processed as described above, followed by conducting the H&E staining.

4.3.3 *In vivo* immunofluorescence imaging (III–V)

For publication **III**, solutions of Alexa-488 labled DPSi/DAu@AcDEX (within which DPSi was labeled) was prepared at concentrations 0.1 mg/mL (DPSi concentration), and a NP solution containing 1 mg/kg of DPSi was injected into healthy or ALF C57BL/6 mice via the tail vein. After 24 h, the mice were narcotized via chloral hydrate and the liver was perfused by paraformaldehyde. The liver was then collected and prepared for histologic section. Before confocal imaging, all the slices were stained by DAPI to image the nucleus, and F4/80 ab90247 was used to stain the macrophages. The confocal images were taken with a Zeiss LSM 780 (Carl Zeiss, Germany) inverted confocal microscope, equipped with argon (488 nm), UV (diode 405 nm) and HeNE (594 nm) lasers.

For publication **IV**, the harvested skin tissues were embedded in an optimal cutting temperature compound (OCT) and frozen in liquid nitrogen for fluorescent immunostaining. 7 μm thick frozen sections were blocked in 10% normal goat serum/0.05% Triton X-100/0.2% BSA (Sigma) in PBS for 40 min at room temperature. The sections were incubated overnight at 4 °C with a CD31 (PECAM-1) antibody (1:200, sc-1506r, Santa Cruz, USA), followed by incubation with goat anti-mouse IgG-TR (Texas Red) secondary antibody for 1 h at 37 °C. DAPI (Sigma) was used to stain the nuclei for 10 min. Subsequently, sections were imaged with fluorescence microscopy. Microvessel density (MVD) was assessed in the wound bed under 200× magnification for each specimen. Subsequently, the microvessel numbers were

counted at 200× magnification within the hot spot area. Only the vessels with clear clusters of endothelial cells with lumen were counted. The MVD value was defined as the average vessel count in 5 specimens.

For publication **V**, all liver slices were conducted with TUNEL staining with the nuclei stained with DAPI as described above.

4.3.4 *In vivo* and *ex vivo* western blot analysis (III–V)

For publication **III**, fresh liver tissue samples from wild-type mice or ALF mice with different formulations were collected or stored under -80 °C, and then prepared and analyzed as described above.

For publication **IV**, fresh skin tissue samples were prepared in ice-cold lysis buffer, as described above. Lysate corresponding to 20 μg of total protein was subjected to SDS-PAGE, and transferred to polyvinylidene fluoride membranes (100 V, 90 min).

The proteins were identified by immunoblot analysis with the appropriate primary antibodies at a dilution of 1:1000 (or as otherwise stated below). Anti-β-actin (A1978, Sigma-Aldrich), anti-Hif-1α (10006421, Cayman Chemical), anti-VEGF (19003, Proteintech). Biotinylated secondary antibody to Rabbit IgG (BAF008 1:5000 dilution for each) was purchased from R&D System. The protein brands were visualized as described above.

For publication **V**, 3 h post ALI-establishment mice were sacrificed and the plasma (ALI plasma) was collected from heart blood, while blank plasma was collected from healthy mice (healthy plasma). DMEM medium containing 10% of healthy plasma and ALI plasma were referred to as healthy medium and ALI medium, correspondingly. Healthy and ALI media with or without PSi at a concentration of 20 μg mL^{-1} were incubated with RAW macrophage cells for 1 h. Then the cell samples were prepared as described above. The proteins were identified by immunoblot analysis with appropriate primary antibodies at a dilution of 1:1000 (or as otherwise stated below). The antibodies used are as follows: Anti-NF-κB (SC-372, Santa Cruz), anti-p-IκBα (2859s, CST), anti-IκBα (SC-371, Santa Cruz) Anti-β-Actin (A5316, Sigma). Biotinylated secondary antibody to mouse IgG (A28177) or Rabbit IgG (BAF008 1:5000 dilution for each) were separately obtained from Invitrogen or R&D System. The protein brands were visualized as described above.

4.3.5 Whole blood and serological analysis (III, V)

Whole blood cell analyses were conducted by an automatic biomedical analyzer (VetScan HM5, ABAXIS, USA) according to the manufacturer's instruction. To assess the injurious effects of APAP on liver histology and function, serum was collected from mice via orbit puncture. Serum samples were taken at indicated post-APAP time points of 12, 24 and 72 h (publication **III**) or 48 h post PSi injection (publication **V**). Alanine aminotransferase (ALT) and aspartate aminotransferase (AST) levels were determined in blood specimens using ALT/AST assay kit (C010-1; NJJCBio, China, publication **III**) and measured by Varioskan plate reader (Thermal Fisher, USA) or using ALT/AST assay kit (140118005, 140218004, Mindray, China, publication **V**) and measured by an automatic biomedical analyzer (VetScan HM5, ABAXIS, USA).

4.3.6 *In vivo* computed tomography (CT) imaging (III)

Prior to conducting *in vivo* CT imaging, the particle concentration dependent hounsfield unit (HU) increase was first measured. Deionized water was used as a control. All the samples were scanned on a positron emission computed tomography (PET)/CT system (Mlabs U-CT, Netherlands) and the images were obtained at an X-ray voltage of 80 kVp, anode current of 500 μA in accurate mode, and full angle with 3 frame averaging. The CT contrasting effect of DPSi/DAu@AcDEX, was evaluated with C57BL/6 mice (body weights: 18–22 g). All the mice were scanned on the same machine. The images were obtained at an X-ray voltage of 55 kVp, and anode current of 615 μA in accurate mode using full angle and 3 frames averaging. Healthy or ALF mice were anesthetized by isoflurane inhalation. The injection volume of contrast agent for each mouse was 200 μL with a dose of 20 mg DAu equiv./kg. The CT imaging was taken at 0, 4, 30, or 90 min post injection.

4.3.7 Assessment of cellular cytokines release by ELISA methods (IV, V)

For ELISA analysis in publication **IV**, fresh wound samples were harvested and stored at −80 °C, and all skin samples were prepared in ice-cold saline. IL-1β, IL-6 and TNF-α levels were analyzed in the same supernatants by using the BD OptEIA human ELISA Set II (cat. 557953, 555244, BD Bioseciences, USA). All assays were performed according to the manufacturers' instructions. Absorbance was measured at 450 nm with a SpectraMax M5 microplate spectrophotometer, and cytokine quantities were calculated through standard curves for each recombinant cytokine.

For publication **V**, both *in vivo* and *ex vivo* ELISA tests were performed. For *in vivo* ELISA tests, liver samples from each mice were harvested and stored at -80 °C, and all liver samples were prepared in ice-cold saline. Then cytokine levels were measured as described above.

For *ex vivo* ELISA tests, healthy and ALI medium with or without PSi at a concentration of 20 μg mL^{-1} were incubated with RAW macrophage cells for 24 h, and IL-1β, IL-6 and TNF-α levels in blank healthy medium, blank ALI medium and the corresponding cell culturing medium were analyzed, as described above.

4.3.8 *Ex vivo* and *in vivo* real-time quantitative polymerase chain reaction (qPCR) analysis (V)

For *ex vivo* qPCR experiments, RAW 264.7 macrophage cells were seeded in 6-well plates at a concentration of 1.5×10^5 cells per well. After incubation overnight, the cells were treated with healthy medium and ALI medium with or without 20 μg mL^{-1} of each type of PSi. After incubating for 1.5 h, total RNA was isolated and analyzed, as described above.

For *in vivo* qPCR experiments, liver samples from each mice were prepared and analyzed as described above.

4.3.9 Brief protein corona analysis (V)

80 μg of each type of PSi was incubated in 4 mL of 40% healthy or ALI plasma in DMEM medium at 4 °C for 4 h. After incubation, the NPs were collected by centrifugation and washed twice with Milli-Q water. The proteins were extracted from the plasma treated NPs with SDS-PAGE. The opsonized NPs (40 μg) were suspended in the PAGE sample buffer (125 mM of Tris-HCl, pH 6.8, 2% of SDS, 5% of glycerol, 0.002% of bromophenol blue) and incubated at 100 °C for 5 min in order to release and denaturate the adsorbed proteins. The samples were run on a 9% SDS-PAGE-gel for 2 h at a constant voltage of 100 V. The gel was stained with 0.025% Coomassie brilliant blue (Thermo Scientific, USA).

4.3.10 Proteomics of different PSi protein corona (V)

Mass Spectrometry (MS)-based shotgun proteomics was employed to study the varying composition of protein coronas from different PSi. ALI plasma was collected as described above, and further incubated with TO, TC and Un at a concentration of 20 μg/mL for 4 h. Afterwards, proteins were digested with trypsin and peptides were labeled with isobaric tags for relative and absolute quantification (iTRAQ), and quantified by LC-MS/MS (see Ref.[257] for detailed information about mass spectrometry-based peptide quantification using iTRAQ).

4.3.11 Statistical analysis

Results are expressed as mean ± standard deviation (SD) or mean ± standard error of mean (SEM). The statistical difference were analyzed using two-tailed paired-samples Student's *t* test (and nonparametric test) via Graphpad Prism (Graphpad softward, USA). The level of significance was set at probabilities of $*p < 0.05$, $**p < 0.005$, and $***p < 0.001$ when comparing viability and flow cytometry results in publication **I**, and $*p < 0.05$, $**p < 0.01$, $***p < 0.0005$ and $****p < 0.0001$ for publications **II-V**

5 Results and discussion

Depending on the physicochemical properties of the payloads, different strategies should be applied to fulfill the preferred release profile(s). Herein, a series of PSi-based nanocomposites/nanohybrids were constructed to load/co-load hydrophilic and hydrophobic drugs. Further multi-functionalities were simultaneously achieved, according to the specific requirements for different biomedical applications.

5.1 Hydrophilic drug (DOX) loaded multifunctional PSi nanocomposites for cancer therapy (I)

PSi has been widely investigated for advanced DDS due to its attractive properties. However, due to the freely accessible pores, bare PSi has several deficiencies in controlling the release of drugs, especially of hydrophilic drugs. In the first two studies of this thesis, the aim was to fabricate PSi-based nanocomposites for the hydrophilic anti-cancer drug DOX, for loading and pH-responsive release, and for further applications of potential anti-cancer efficacy. To achieve this, in publication **I**, a ligand to feasibly modify PSi was designed and synthesized. This nanosystem inherits several advanced properties in a single carrier, including promoted anticancer efficiency, multiple drug resistance (MDR) reversal, stimuli-responsive drug release, drug release monitoring, and enhanced particle–cell interactions.

5.1.1 pH-sensitive drug release behavior of the nanosystem

A pH-sensitive metal-drug complex was applied in the design of the system for hydrophilic drug loading. Inspired by the structure of dopamine, 3-aminopropoxy-linked quercetin (AmQu), a derivative of a natural anti-cancer flavonoid was designed and subsequently used to modify PSi (**Figure 9A**). The successful synthesis of AmQu was confirmed by ^{1}H NMR and ^{13}C NMR. Successful conjugation of AmQu was confirmed by FTIR and UV-*vis* spectra (see **Figure S3** in publication **I**). Moreover, the following iron ion chelation was confirmed by energy dispersive X-ray spectroscopy (EDX, see **Figure 2** in publication **I**). The DOX loading capacity of Fe^{3+}-AmQu-UnTHCPSi (FAP) was 24 ± 2% (w/w), higher than the loading capacity of bare UnTHCPSi (10 ± 1%, w/w). In addition, after DOX was loaded into the particles, its fluorescence was quenched (**Figure 9B**), probably due to the interaction between DOX and the anthocyanidin ring structure within the AmQu through an electron transfer mechanism.[258] This feature may further be applied to monitor the drug release behavior.

In vitro DOX release behavior was also investigated. In the bare UnTHCPSi most of the loaded DOX was burst-released within 1 h of incubation in the release medium. For DOX-loaded in FAP (DOX@FAP), when the pH-value was 7.4, only about 14.8 ± 0.9% of DOX was released within 4 h, and no clear extra DOX was released in the following 20 h. However, the released drug amount was significantly increased when the pH-value was more acidic, as 77.3 ± 1.6% of DOX was released at pH 5 within 24 h (**Figure 9C**).

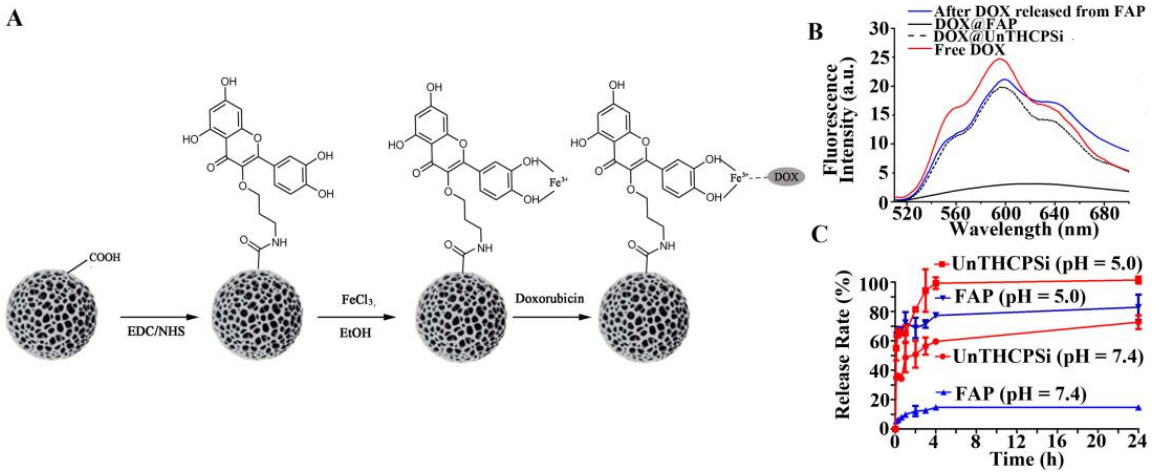

Figure 9. *(A) Synthesis process for FAP/DOX PSi-modified nanocomposites. Abbr. EDC, 1-ethyl-3-(3-dimethylaminopropyl) carbodiimide; NHS, N-hydroxysuccinimide; Et, ethyl. (B) Fluorescence spectra of DOX before and after release from FAP, λ_{ex} = 490 nm. In vitro DOX release curves of UnTHCPSi and FAP at pH 5 and pH 7.4 PBS buffer at 37 °C within 24 h. Data are shown as mean ± SD (n = 3). Figures were reprinted with permission from publication* ***I***.

5.1.2 Potential application in DOX-resistent cancer treatment and imaging

One of the most challenging obstacles in NP surface modification is to achieve the concept that one ligand can accomplish multiple purposes. The modification of AmQu could not only endow PSi with pH-responsive DOX release behavior, due to the similar structure between AmQu and dopamine, but it could also enhance the particle–cellular interaction of FAP compared to bare PSi, which was observed from the fluorescence intensity assisted quantitative analysis and the corresponding confocal imaging (**Figure 10A(a)**). In addition, the stimuli-induced drug release was correlated with the recovery of fluorescence, thus giving real-time information about the stimuli-dependent drug release, as only the fluorescence of DOX could be observed when the drug was intracellularly released while no obvious fluorescence signal was observed when the drug was still residing in the vehicle (**Figure 10A(b)**). Moreover, the anti-cancer efficiency of the developed nanocomposite was tested on a DOX-resistant human breast cancer cell line, DOX/MCF-7^R, and a statistically significant difference was observed between DOX@FAP and free DOX (37 ± 1% *vs.* 65 ± 2%, ***p< 0.001) (**Figure 10B**). This could not only be explained by the promoted cellular uptake of FAP as described above, but also due to the anti-cancer effect of AmQu, which can be cleaved from FAP when endocytosized by cancer cells (**Figure 10C**). Indeed, the anticancer efficiency of free AmQu + free DOX was higher than that of DOX alone (44 ± 3% v.s. 65 ± 2%, **p< 0.005). Previous results have confirmed the anti-cancer and drug resistance reversing ability of quercetin, and 4'-OH and 7-OH groups within the quercetin structure are necessary for this activity.[259] Herein, we specifically modified the 3-OH moiety of quercetin, and therefore a better anticancer effect was expected.

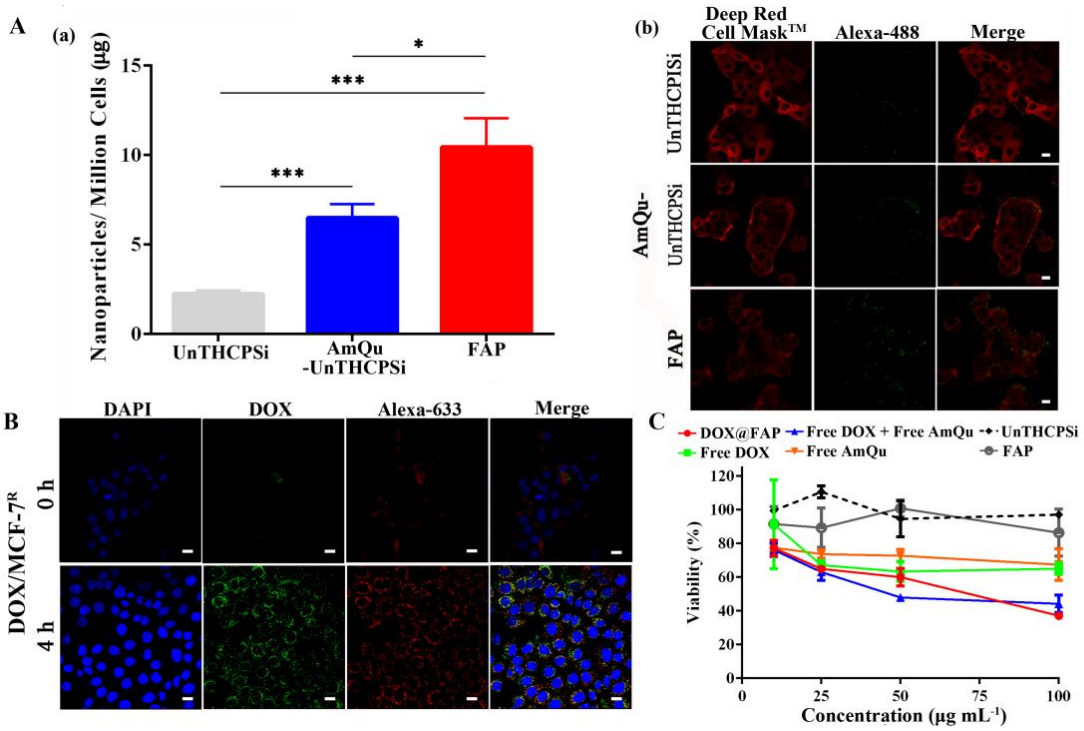

Figure 10. *(A) (a) Quantitative cellular uptake of different particles by DOX/MCF-7^R. Error bars represent standard deviation (n = 3), *p < 0.05 and ***p < 0.005. (b) Confocal microscope images of Alexa-Fluor 488 conjugated particles interacting with DOX/MCF-7^R cells after incubation at 37 °C for 3 h. All scale bars are 20 µm. (B) Confocal images of Alexa-Fluor 633 conjugated NPs (red) interacting with DOX/MCF-7^R cells after incubation at 37 °C for 2 h, followedg by immediate imaging or after incubating for another 4 h. All scale bars are 8 µm. (C) Cell viability of DOX/MCF-7^R breast cancer cells treated with different formulations. The concentration indicates the amount of UnTHCPSi; for other agents the concentration is equivalent to the corresponding concentration within FAP. Data are shown as mean ± SD (n ≥ 3). Figures were reprinted with permission from publication* ***I***.

5.2 Hydrophilic drug loaded PSi nanocomposites for cancer targeting (II)

In addition to pH-responsive hydrophilic drug release and multi-functionalities for anti-cancer therapy applications, it would be preferred to simultaneously obtain a specific targeting ability. In publication **II**, a versatile carbonic anhydrase IX (CA IX, a specific protein expressed in the outer cell membrane of cancer cells in hypoxia conditions) targeting nanocomposite was constructed. The fluorescence properties of the ligand also equipped the nanocomposites with imaging capabilities.

5.2.1 Characterization and DOX loading/release studies of the nanocomposites

A novel CA IX targeting ligand VD11-4-2 was applied to modify PSi. VD11-4-2 was conjugated on PSi particles (VD-PSi), as illustrated in **Figure 11A**. The DOX loading

degree of VD-PSi was higher than that of bare PSi (21.4 ± 0.1% *vs.* 10.1 ± 0.1%, w/w). This may be caused by the hydrogen bond formation between VD11-4-2 and DOX. UV-Vis spectrum of DOX-loaded VD-PSi (DOX@VD-PSi) confirmed the initial hypothesis. Compared to free DOX and VD11-4-2, the spectrum of DOX@VD-PSi showed a clear red shift for DOX and VD11-4-2, which was the main characteristic for hydrogen bond formation (**Figure 11B**). A pH-responsive DOX release was also observed from DOX@VD-PSi, mainly due to NH_3^+ formation in the acidic solution, which reduced the number of hydrogen-bond-forming acceptors and therefore weakened the overall hydrogen-bonding interactions (**Figure 11C**).

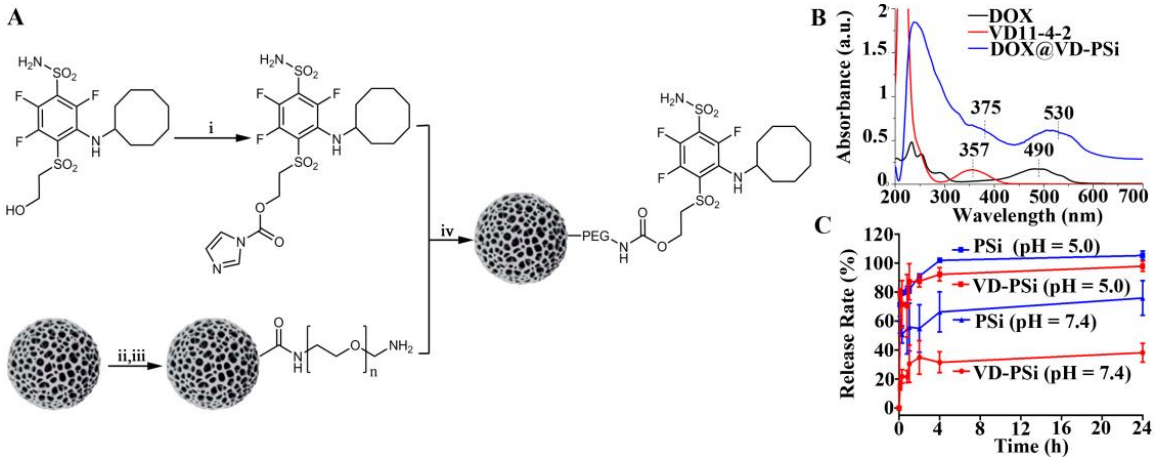

Figure 11. *(A) Scheme of the VD-PSi fabrication. (B) UV−Vis absorption spectra of DOX, VD11-4-2, and DOX@VD-PSi in aqueous solution indicating the hydrogen bond between VD11-4-2 and DOX. (C) In vitro DOX release curves of DOX@PSi and DOX@VD-PSi at different pH-values. Data is shown as mean ± s.d. (n = 3). Figures were reprinted with permission from publication* ***II****.*

5.2.2 Enhanced cancer targeting and potential application in imaging

Immunofluorescence analysis was carried out to verify the exclusive expression of CA IX in MCF-7 cells under hypoxic conditions. Afterwards, the capability of VD-PSi to inhibit CA IX catalytic activity was evaluated and compared to the free compound VD11-4-2: VD-PSi showed a similar inhibition effect towards CA IX catalytic activity, but presented a higher equilibrium dissociation constant (K_D) value (**Figure 12A**). This minor difference was partly due to the immobilized compound being inaccessible to the protein. The anti-cancer effect of DOX@VD-PSi was evaluated under normoxia and hypoxia conditions. Under normoxia, DOX@VD-PSi showed less of an anti-cancer effect compared to free DOX, due to the detained DOX release and decrease in cellular–particle interactions as a result of the PEG modification. However, under hypoxia, which can better mimic the solid tumor environment, a prominent DOX resistance was observed, and the DOX@VD-PSi formulation showed the highest killing ratio among all the study groups. Moreover, extra addition of free VD11-4-2 could dampen the effect, partly proving the hypoxia induced cancer targeting effect by VD-PSi (**Figure 12B**).

VD11-4-2 obtained special fluorescence properties with a λ_{ex} of 360 nm and λ_{em} of 500 nm. This distinctive fluorescence feature may assemble a system resulting in the formation of a FRET complex: a donor VD11-4-2 energy transfer to the acceptor DOX (λ_{ex} = 490 nm, λ_{em} = 600 nm), where the fluorescence of VD11-4-2 was quenched as a result of DOX absorbance. The fluorescence spectra of VD-PSi before and after DOX loading (λ_{ex} = 360 nm) confirmed the initial hypothesis (**Figure 12C**), further suggesting the potential of applying VD-PSi to monitor the DOX release behavior via fluorescence imaging. Confocal laser scanning microscopy experiments were conducted to confirm the hypothesis about using the FRET effect between VD11-4-2 and DOX to monitor the drug release. While DOX is inside the particles (3 h incubation), 360 nm wavelength excites VD11-4-2 and the energy from VD11-4-2 transfers to DOX; thus, a DOX fluorescence signal (~600 nm) was observed with no notable VD11-4-2 fluorescence (~500 nm). After DOX was released from the particles, and the distance between DOX and VD11-4-2 was larger than the typical limiting distance of FRET (about 10 nm), the VD11-4-2fluorescence signal was observed (**Figure 12D**).

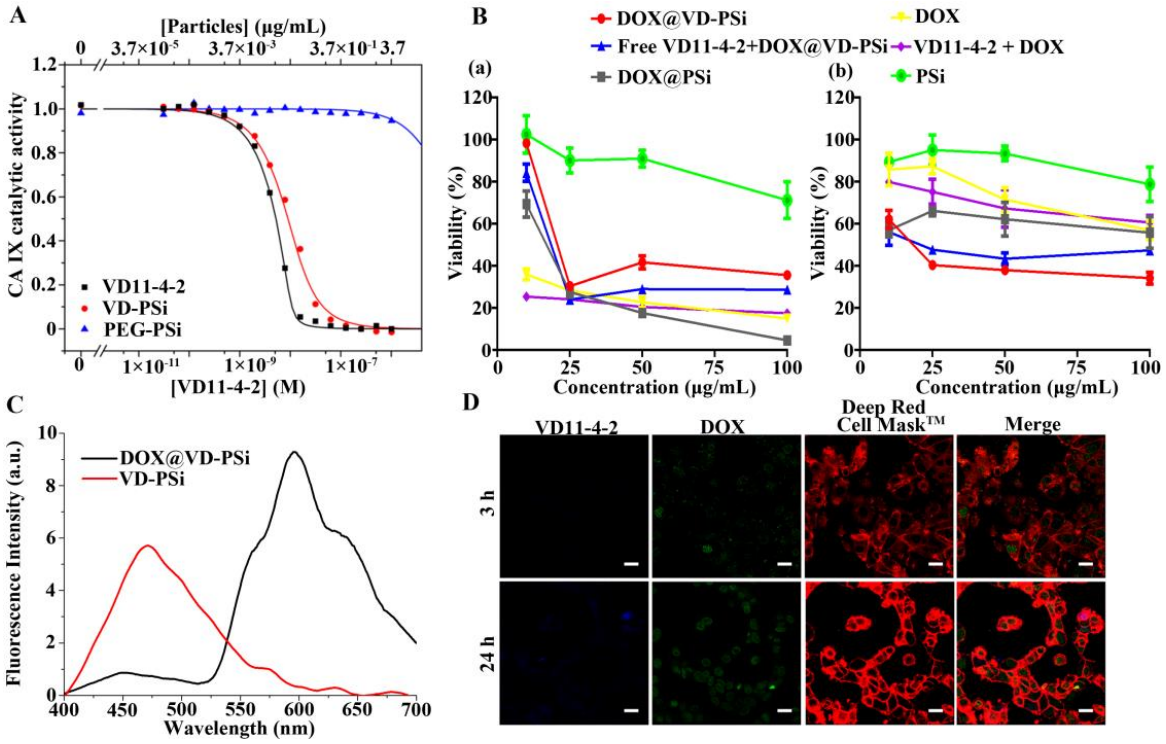

Figure 12. *(A) CA IX protein inhibition determined by stopped-flow kinetics CO_2 hydration assay. The lines were fitted according to the Morrison model. (B) Normoxia (a) and hypoxia (b) cellular viability results of MCF-7 cancer cells treated with different concentrations of DOX in different formulations for 48 h. The concentration indicates the amount of PSi; for the other compounds the concentration was equivalent to the corresponding concentration within VD-PSi. Data are shown as mean ± SD (n ≥ 3). (C) Fluorescence intensity of VD-PSi and DOX@VD-PSi at PSi concentration of 5 mg/mL with λ_{ex} = 360 nm. (D) Confocal microscope images of DOX@VD-PSi interacting with MCF-7 cells after incubation for 3 and 24 h under hypoxic conditions. Figures were reprinted with permission from publication* ***II***.

5.3 Hydrophobic drug loaded PSi nanohybrids for theranostic liver regeneration (III)

Hydrophobic PSi has been shown to improve the solubility and bioavailability of hydrophobic drugs, making it a good candidate for hydrophobic drug loading. To better control the drug release profile, microfluidic-assisted nanoprecipitation was carried out to encapsulate different particles within one polymer matrix by simply altering their surface properties. The nanohybrids also can act as contrasting agents for CT imaging due to the presence of Au NPs in the polymer matrix. Due to the major accumulation of the nanohybrids in the liver, the constructed nanohybrids were loaded with a hydrophobic small molecule (XMU-MP-1) with effective regenerative capability,[260] intended for further applications in acute liver failure (ALF) theranostics.

5.3.1 Characterization

Un PSi was adopted in the study due to its feasible surface modification properties. pH-responsive polymer AcDEX was used to encapsulate both PSi and Au NPs. A schematic illustration of the procedure to prepare the DPSi/DAu@AcDEX by microfluidics is shown in **Figure 13A**, demonstrating a single-step, simultaneous co-encapsulation of different NPs. After encapsulation, PSi with irregular shape (**Figure 13B(a)**) and small-sized gold nanoparticles (~ 5 nm, **Figure 13B(b)**) were fully covered by AcDEX matrix and new nanohybrids were formed containing both types of particles with spherical morphology (**Figure 13B(c-d)**).

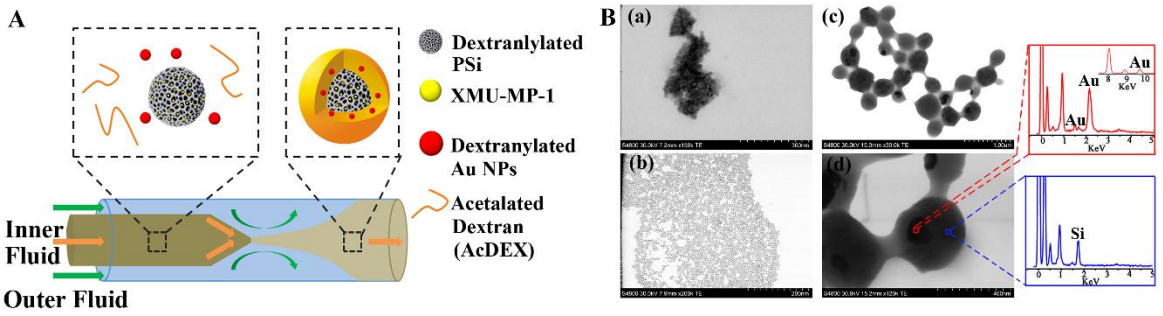

Figure 13. *(A) Schematic illustration of the procedure to prepare the DPSi/DAu@AcDEX by microfluidics. (B) TEM images showing morphologies of (a) PSi, (b) Au, (c, d) DPSi/DAu@AcDEX at each step and the corresponding EDX spectrum. Figures were reprinted with permission from publication **III**.*

5.3.2 Drug loading/release behavior

Without PSi, the drug loading degree within the polymer matrix was as low as 0.04% with the same loading procedure, whereas a loading degree of 7.8% was achieved by applying PSi. The outer layer of the pH-sensitive polymer AcDEX will render the nanohybrids to release the drug only in an acidic environment, which occurs within the intracellular environment. The *in vitro* release study showed that only 13.1 ± 2% of the loaded drug was released within 5 h at extracellular pH (7.4), while the amount released increased to over

90% at intracellular pH (5.0) (**Figure 14A**). Indeed, when co-incubating the particles and macrophages (KG1) cells, a drug release augmentation was observed compared to blank medium (**Figure 14B**). This was mainly due to the cellular internalization induced drug release in the endosomes. Subsequently, XMU-MP-1 with high permeability could penetrate through the membrane of KG1 and potentially reach the extracellular medium, suggesting that the nanohybrid interacted with the target cells (hepatocytes) in an indirect manner. Western blot results further confirmed this cellular uptake dependent drug release profile. HepG2 was co-incubated with drug loaded nanohybrids (MP@DPSi/DAu@AcDEX) over time. The inhibition of key proteins' expression, phosphorylated Mps one binder (p-MOB) and phosphorylated Yes-associated protein (p-YAP), became prominent from 3 h to 12 h, which was mainly induced by time-dependent particle uptake triggered drug release, suggesting that the nanohybrids could serve their function in a direct manner (**Figure 14C**).

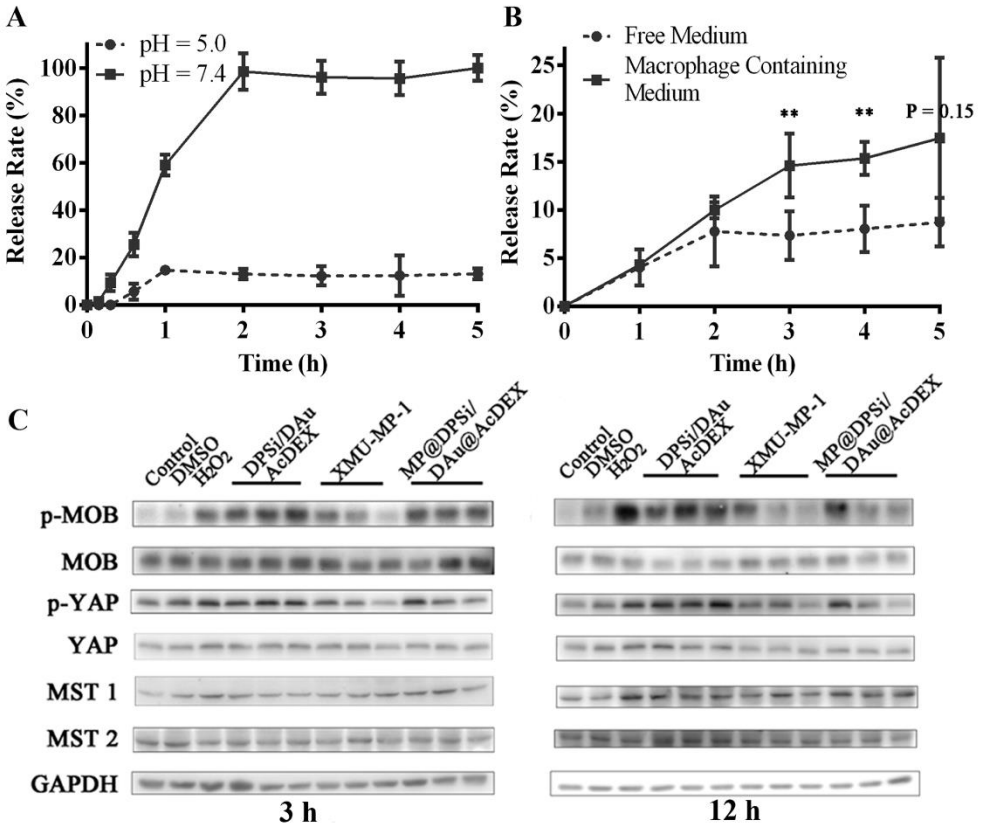

Figure 14. *(A) In vitro XMU-MP-1 release curves at pH 5 and 7.4 in PBS containing 5% of P-188 at 37 ºC within 5 h. (B) XMU-MP-1 release curve in RPMI medium, containing KG1 macrophages at 37 ºC within 5 h. Data are shown as mean ± SD (n ≥ 3), **p < 0.01. (C) Relative phosphorylation levels of MOB and YAP (p-MOB and p-YAP) in HepG2 with different formulation treatments over time (3 to 12 h). The corresponding panels (from left to right) are: control, dimethyl sulfoxide (DMSO)–treated control, H_2O_2-treated control, DPSi/DAu@AcDEX with low, medium and high concentration (from left to right), free XMU-MP-1 (1, 3, and 10 μM from left to right, dissolved in DMSO), and MP@DPSi/DAu@AcDEX (containing the same amount of XMU-MP-1 at the corresponding concentration). Figures were reprinted with permission from publication **III**.*

5.3.3 *In vivo* ALF theranostic evaluation

ALF model was established by the overdosed administration of acetaminophen (APAP), which is also a common cause of ALF worldwide. Serum alanine aminotransferase (ALT) and aspartate transaminase (AST) levels at different time points quantitatively confirmed the overall better alleviation of hepatic damage by MP@DPSi/DAu@AcDEX compared to free drug (see **Figure 3C** in publication **III**). This was further qualitatively confirmed by TdT-mediated dUTP Nick-End labeling (TUNEL) staining (**Figure 15A**). Moreover, MP@DPSi/DAu@AcDEX obtained better cardiac compliance at high drug concentration (3 mg/kg for XMU-MP-1), as the hydrophobic free drug precipitated out and caused myocardial infarction at high dose, while this phenomenon was averted by applying the nanohybrids (**Figure 15B**).

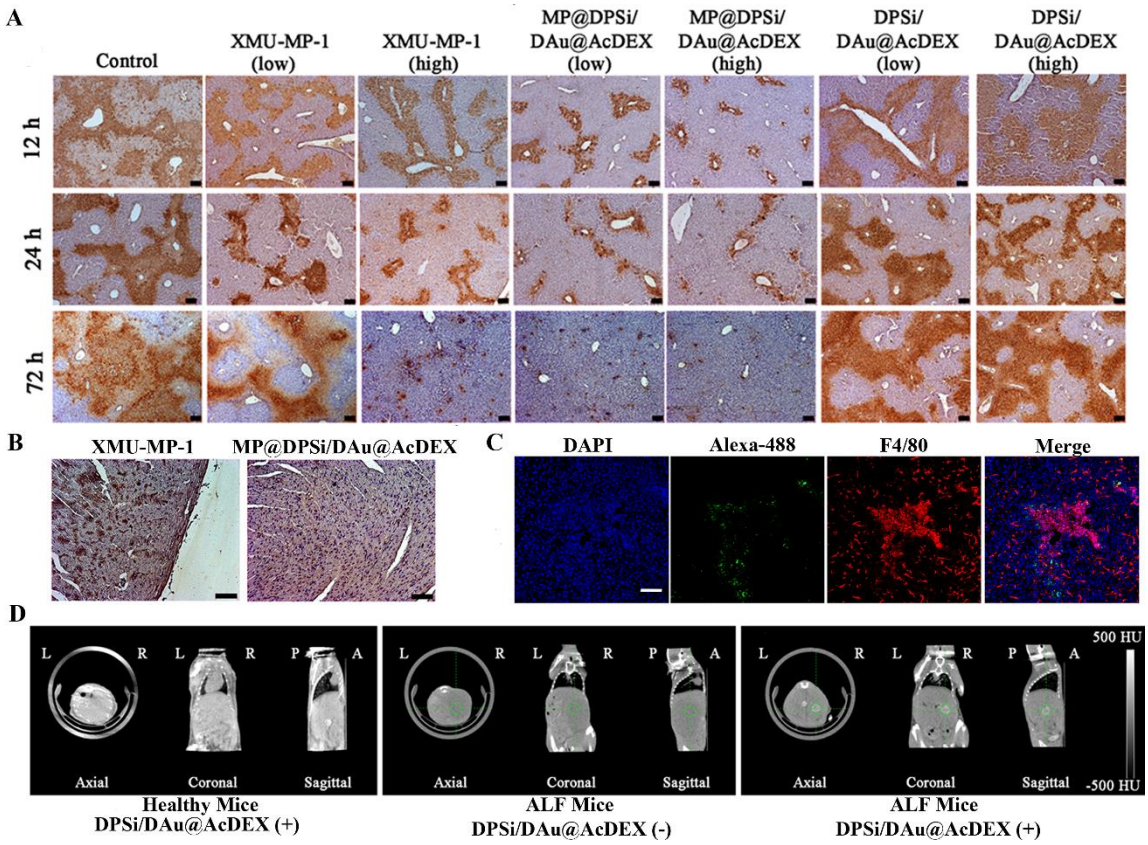

Figure 15. *(A) TUNEL staining of liver sections at different time-points. ALF model was established by 200 mg/kg APAP gavage administration. The treatment was initiated 2.5 h post APAP gavage. ALF mice were administrated with different formulations twice daily. (B) CXCR-4 immunohistochemical staining heart sections at 72 h after administrating free drug or MP@DPSi/DAu@AcDEX (with 3 mg/kg of XMU-MP-1), suggesting enhanced compliance with the application of nanohybrids. (C) Immunofluorescence images of ALF liver after i.v. administration with Alexa-488 labeled DPSi/DAu@AcDEX. (D) In vivo CT images of healthy or ALF mice with or without i.v. administration of DPSi/DAu@AcDEX. Detailed concentrations and sample preparation methods can be found in the corresponding paper. Figures were reprinted with permission from publication* ***III****.*

The potential rationale for the enhanced treatment index of MP@DPSi/DAu@AcDEX was due to the lesion site specific accumulation of the particles. Immunofluorescence imaging demonstrated that the immune cells were recruited and accumulated at lesion sites after ALF establishment and the NPs were co-localized within the macrophages, thus resulting in targeted accumulation within the damaged part (**Figure 15C**). Taking advantage of this property, the co-resided Au NPs were applied as contrasting agents for CT imaging for lesion detection and characterization. For ALF mice, after *i.v.* injection of DPSi/DAu@AcDEX, a distinguishable area was generated 30 min post-injection, while no clear signal was observed from healthy mice, which is promising for early stage ALF diagnosis (**Figure 15D**). Altogether, these results support the idea of developing nanohybrids as potential theranostic platforms for ALF.

5.4 Dual-drug loaded PSi nanohybrids for tissue regeneration (IV)

Simultaneous incorporation of two drugs with different physiochemical properties into a single carrier was achieved. A deliberately designed oxidation responsive polymer was synthesized to encapsulate a hydrophobic drug loaded PSi that dynamically conjugated a hydrophilic drug. Furthermore, the orchestrated cascade from wound detection, ROS scavenge, and drug release to hydrogel formation was initiated by the specific disease status, therefore bio-mimetically enhancing the tissue regeneration effect.

5.4.1 Characterization and close-loop degradation of the nanohybrids

An oxidation responsive polymer, POD, was synthesized by modifying ODEX with phenylboronic pinacol ester, which was further applied into encapsulating hydrophobic drug (ATO) loaded PSi to form ATO loaded PSi@POD. Due to the excess aldehyde groups from ODEX, the newly formed nanohybrids were simultaneously anchored with the amine group containing GOx and deferoxamine (DFO) through a pH-sensitive dynamic bond Schiff-base formation (D-G-PSi@POD). To facilitate further *in vivo* applications, the nanohybrids were integrated onto collagen patches. The introduction of GOx endowed the system with the ability to respond to surrounding glucose levels as it can catalyze glucose oxidation, and generate gluconic acid and H_2O_2. Gluconic acid decreased the surrounding pH-value and triggered the DFO release, and the pernicious side product H_2O_2 could be close-loop consumed by POD, synchronously releasing the loaded ATO. Furthermore, the degradation product of POD, ODEX, formed *in situ* into a hydrogel embedded within a collagen patch. This *in situ* NP/hydrogel transformation created a moist environment around the wound bed, altering the stiffness of the patch to better mimic the elastic properties of the natural soft tissues (**Figure 16A**). The produced PSi-encapsulated nanohybrids are shown in **Figure 16B**, and after embedding on the collagen patch, a nano-network was formed (**Figure 16C**). TEM images confirmed the glucose triggered close-loop particle degradation. An integrated PSi@POD structure was still observed after 24 h incubation without addition of glucose. However, the shell structure of POD was barely observed at 4 mg mL^{-1} of glucose, and at 1 mg mL^{-1} of glucose only an indistinct polymeric layer was found (**Figure 16D**). The degradation product ODEX can further function as a cross-linker to form into a hydrogel with the collagen-ark *in situ*, and thereby the inherent flaw of collagen patches, namely low

stability and poor mechanical properties, would be partially solved. Oscillatory stress sweep tests were carried out to confirm the enhanced viscoelastic property. **Figure 16E** shows that a structure breakdown occurred at higher shear stress when adding ODEX or PSi@POD, where the collagen + PSi@POD + 4 mg mL^{-1} glucose (CP4) obtained the highest stiffness enhancement. Despite the same cross-linker (ODEX) concentration, the reason for the higher viscoelastic property of CP4 could be explained by the local pH value decrease as a result of gluconic acid production. This could allow the fibers of collagen to repel against each other and to de-aggregate, further facilitating the interactions between collagen and ODEX.[261]

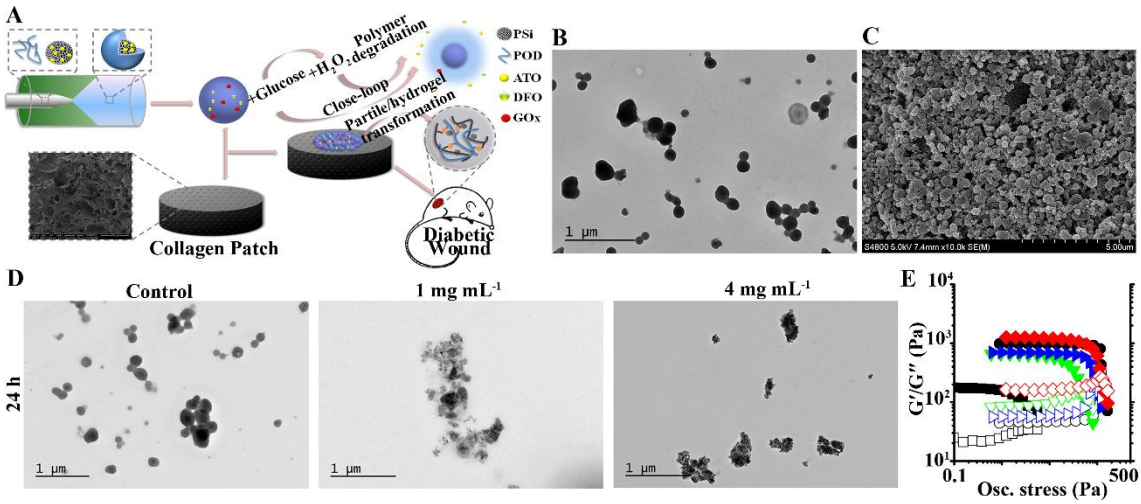

Figure 16. *(A) Scheme of the dynamic close-loop nanohybrids construction and the following biomedical applications for diabetic wound healing. (B) TEM image showing the morphologies of D-G-PSi@POD. (C) SEM image showing the nanohybrids embedded collagen patch. (D) TEM images of D-G-PSi@POD with different concentrations of glucose at 24 h, suggesting a glucose dependent dissassembly behavior of the nanosystem. (E) Rheological dynamic oscillatory stress sweep tests of different hydrogels. The solid data points correspond to the storage moduli G'. The open data points correspond to the loss moduli G". black square, black circle, green down-triangle, blue right-triangle and red diamond respectively correspond to collagen (C), collagen+ODEX (COD), collagen+PSi@POD (containing the same concentration of ODEX, CP), collagen+PSi@POD+1 mg/mL glucose (CP1) and collagen+PSi@POD+4 mg/mL glucose (CP4). Figures were reprinted with permission from publication **IV**.*

5.4.2 *In vitro* dual drugs release

We further investigated the dual-drug release profiles of D-G-PSi@POD *in vitro* (**Figure 17**). Transwell-assisted method was applied here, where the D-G-PSi@POD embedded collagen patch was loaded in the upper chamber, and drugs' concentrations were monitored in the donor chamber. For free drugs loaded collagen patches, over 97% of the drugs were released during the first 3 h, whereas only 9.5 ± 1.4 % of ATO and 35 ± 2.9 % of DFO were released after 72 h without glucose addition, when the nanohybrid was employed. Cumulative ATO/DFO release was significantly higher when the glucose concentration was increased. After 72 h the cumulative release of ATO/DFO was 57 ± 2.7% and 71 ± 22%at

the glucose concentration of 1 mg mL^{-1}, and the release values increased to more than 90% at a glucose concentration of 4 mg mL^{-1}. This glucose dependent release profile may further lead to stage-specific drug release from the patch when applied *in vivo*. As the local glucose content in a diabetic wound bed is highly correlated to the diabetic condition and tissue repairing process, and thus the drug release rate is biomimetically related to the healing process. With the closure of the dermis gap, fewer blood and tissue exudates can infiltrate into the wound bed, thus altering the release behavior of both drugs, and benefitting the therapeutic efficiency and rehabilitation.

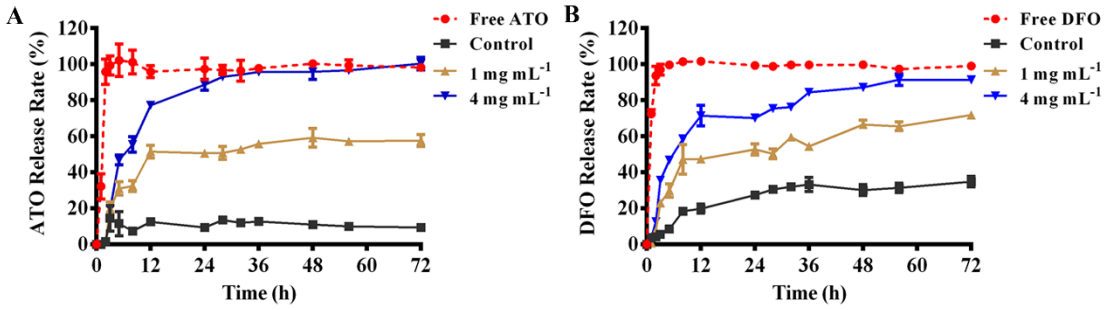

Figure 17. *Release profiles of ATO (A) and DFO (B) from a D-G-PSi@POD embedded collagen patch. The release was conducted in 1× PBS buffer (pH = 7.4) with 0, 1 or 4 mg mL^{-1} glucose. Free ATO and DFO were directly added in collagen patches and were used as the control. Data represent mean ± SD (n = 3). Figures were reprinted with permission from publication* ***IV****.*

5.4.3 Biomimetically stage-specific enhanced regeneration

Streptozotocin (STZ)-induced diabetic mice with full thickness wounds were used to evaluate the *in vivo* performance of the system for diabetic wound closure. The mice were randomly divided into four groups (n = 5) and topically administrated with different samples, including (1) collagen patch with blank PSi@POD (CP), (2) collagen patch with free ATO, DFO and GOx (CF), (3) collagen patch with ATO/GOx loaded PSi@POD (PA), and (4) collagen patch with ATO/DFO/GOx loaded PSi@POD (PAD). The PAD group showed the best healing efficiency in the early stage. However, the healing rate of the PAD group was detained after day 6, while the wound closure rate of CF group was not interfered (**Figure 18A**). This was caused by the fact that less tissue exudate and bleeding limited the release of drugs from the nanosystem. Yet the release of free drugs was not affected. This biomimetically altered regeneration capability is beneficial for tissue engineering, as long term uncontrolled regeneration may bring detrimental side effects.[262] To better explore this phenomenon, immunofluorescence staining for CD31 was studied to investigate the distribution of micro-vessels in the regenerative dermis near the wound bed, and the microvessel density (MVD) was semi-quantitatively evaluated (**Figure 18B**). At day 7, the MVD of PAD was higher than CF (PAD *vs.* CF, 181 ± 33 *vs.* 128 ± 28 microvessels/hot spot, *P < 0.05), yet the tendency was reversed at day 14 (69 ± 25 *vs.* 124 ± 25 microvessels/hot spot, *P < 0.05). DFO has long been confirmed to inhibit the degradation of hypoxia inducible factor 1α (Hif-1α), resulting in a promoted regeneration effect. To confirm the mechanism, western blot analysis was conducted and semi-quantitatively

confirmed this stage specific Hif-1α expression (**Figure 18C**). Furthermore, the production of vascular endothelial growth factor (VEGF), as a downstream effector of Hif-1α, consequently exhibited a similar tendency (**Figure 18D**).

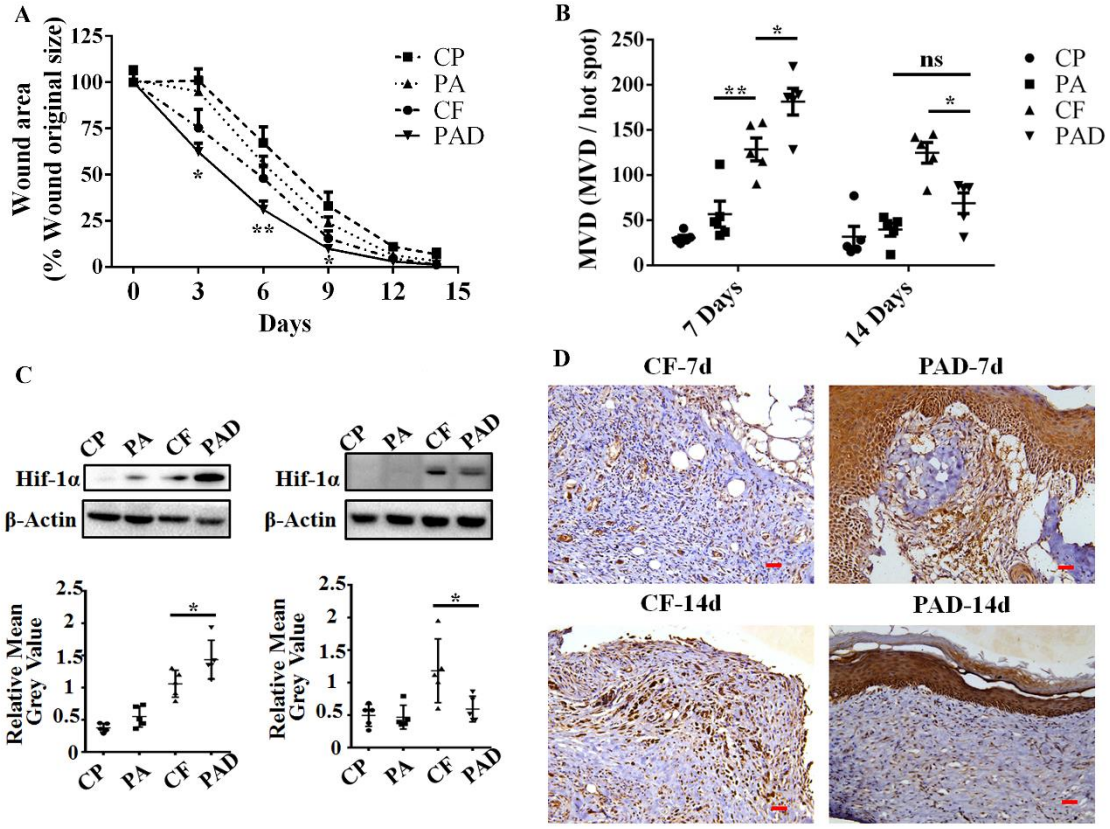

Figure 18. *(A) Quantification of the wound area of different groups at different days by using Image J software. (B) Semi-quantitative micro-vessel density of different groups at day 7 and day 14. (C) Western blot analysis of Hif-1α at different healing stage. (D) Immunohistochemical staining of VEGF within the wound sites at 7 d or 14 d after treatment with different formulations. All scale bars are 100 μm. All the error bars indicate the SD value (n = 5). *p < 0.05 and **p < 0.01. Figures were reprinted with permission from publication **IV**.*

5.5 Biological response of different PSi under inflammation (V)

When applying PSi for DDS fabrication, NPs would ideally accumulate within lesion sites, and the interaction between DDS and lesion sites might alter the biocompatibility of the materials and affect the disease outcome. Therefore, it would be valuable to investigate the immunomodulatory and biological effects of different PSi within pre-existing lesion sites, and explore the potential mechanisms.

5.5.1 Effects of different PSi on acute liver inflammation

Three different PSi NPs, namely TO, TC and Un, were investigated within the current work, as they obtained an overall similar size, ζ-potential and porosity, but distinguished surface chemistries, representing the majorly applied PSi surface stabilization methods.

Considering the high accumulation of PSi NPs in the liver, prior to PSi injection, mice were induced with acute liver inflammation (ALI) in order to investigate the biological response of different PSi NPs within lesion sites. After 48 h post PSi injection, the whole blood analysis was first conducted to evaluate systemic changes associated with blood leukocytes. Compared with healthy mice, the ALI group showed a significantly enhanced total white blood cells (WBC) number. Notably, compared to ALI group, none of the PSi NPs showed further WBC number enhancement (**Figure 19A**), suggesting a confined secondary WBC recruitment effect of the different PSi NPs under the inflammatory conditions. Furthermore, ALT and AST values of each sample were measured to examine the hepatic function for partly reflecting the inflammation progression after injecting the PSi NPs. Compared to the ALI group, PSi administration caused a surface chemistry dependent decrease in the AST/ALT value, with Un at high concentration reaching a statistically significant difference (**Figure 19B**). GSH values were further evaluated and the results suggested that TO and Un administration significantly attenuated the liver damage (**Figure 19C**). ELISA assay was conducted to further unravel the inflammatory status after PSi injection. The expression levels of three main pro-inflammatory cytokines (TNF-α, IL-6, and IL-1β) were examined, and the results suggested that TO and Un show a significant inflammation attenuation effect, whereas this effect was marginally robust from TC (**Figure 19D-F**). Overall, the results suggested that under an inflammatory condition, PSi administration might alter the disease outcome and immune response in a surface chemistry dependent manner.

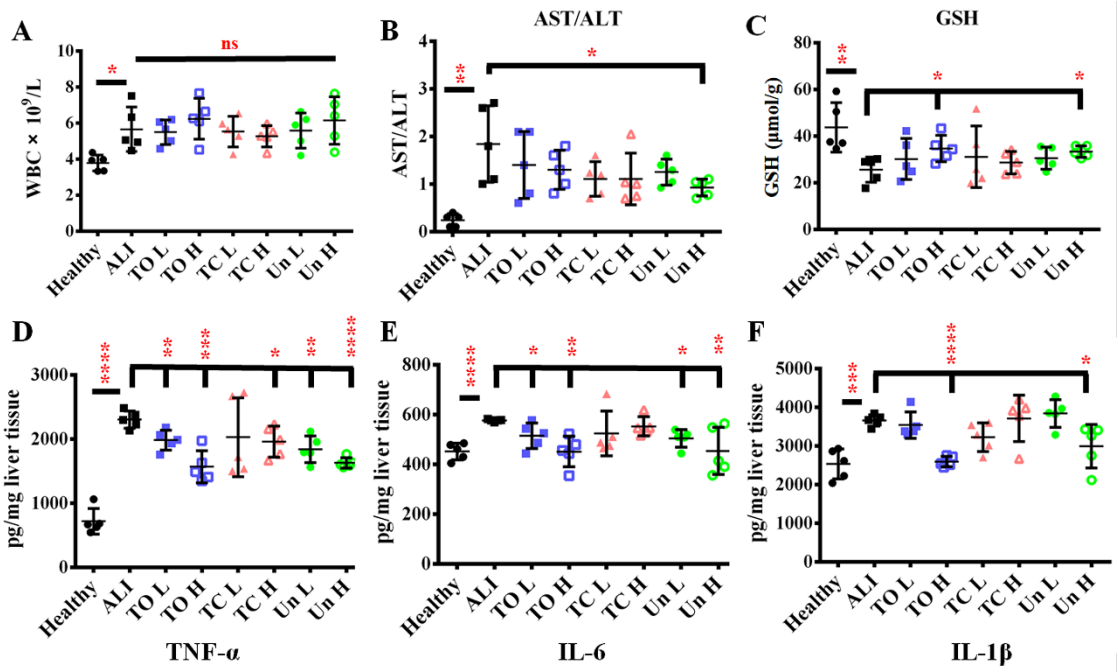

Figure 19. *(A) Total WBC numbers of each group. (B) Serum AST/ALT level of each group. Quantitative analysis of GSH (C), TNF-α(D), IL-6 (E) and IL-1β (F) within liver tissues of each group. All the error bars indicate the SD value (n = 5). *p < 0.05, **p < 0.01, ***p < 0.005 and ****p < 0.001.*

5.5.2 Effects of PSi back bonds on ROS scavenge

The ubiquitous decline in AST levels and the induced AST/ALT ratio attenuations after PSi administration were of interest to us. Considering that the hepatocellular AST is mainly presented in the mitochondria, a decline in AST leakage may suggest remitted mitochondrial damage, which is usually caused by over-produced ROS.[263] The existence of reductive Si–Si back bonds, which is a unique feature of PSi NPs, may feasibly consume and scavenge ROS to proceed with the oxidation process, further forming Si–O–Si linkages to facilitate the hydrolysis and degradation reactions (**Figure 20A**).[264] Therefore, our first hypothesis was to investigate whether the reductive PSi back bonds might consume overt ROS and further modulate liver damage.

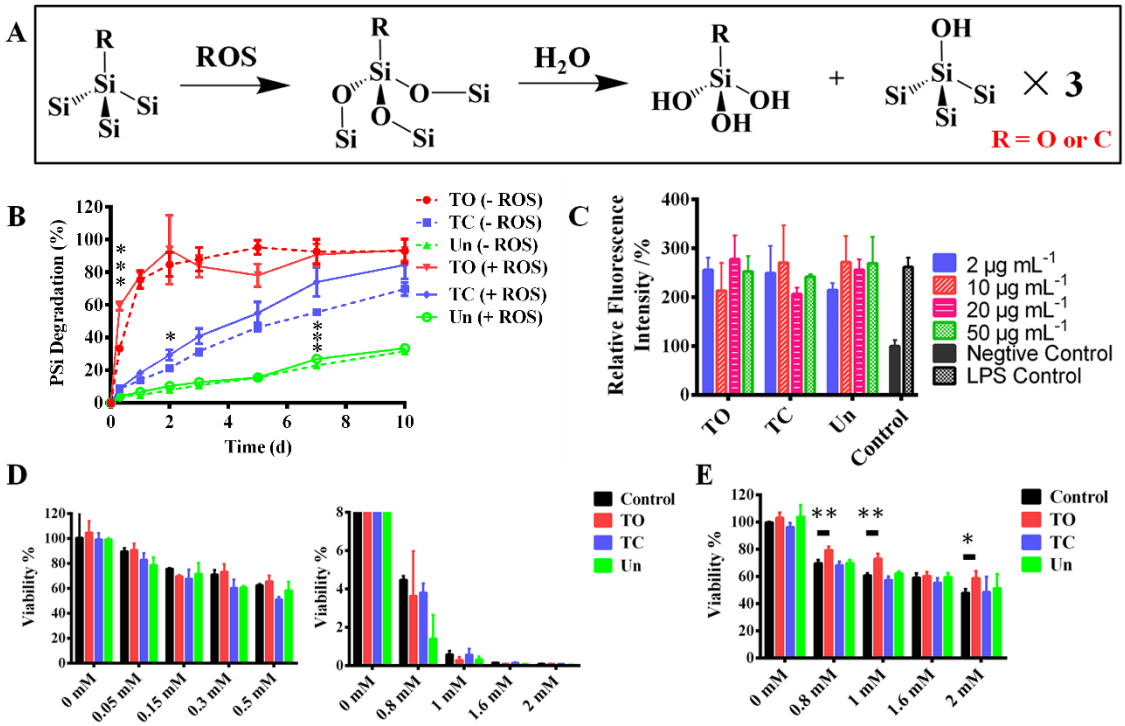

Figure 20. *(A) Schematic illustration of the PSi NPs' degradation process. (B) ROS addition enhanced the degradation kinetics of PSi NPs to a different extent. (C) Sequential addition of PSi NPs to RAW cells under inflammatory stress showed no effect on attenuating the intracellular ROS amount. (D) Co-adding PSi NPs and H_2O_2 to HepG2 cells simultaneously showed no effects on reversing the ROS-induced cellular apoptosis. (E) Pre-incubating H_2O_2 containing medium with TO for 24 h could mildly reduce the cytotoxicity of H_2O_2. All the error bars indicate the SD value (n = 5). *p < 0.05, **p < 0.01, ***p < 0.005 and ****p < 0.001.*

Indeed, the addition of ROS could accelerate the PSi degradation kinetics to different extents, and the degradation rate ranking for the different PSi NPs was TO > TC > Un (**Figure 20B**). The variations in degradation kinetics were due to the hydrophobic surface of TC and Un preventing the surface wetting. However, this ROS scavenging effect was marginally robust under *in vitro* levels. The intracellular ROS contents of murine macrophage RAW cells was highly enhanced after LPS/IFN-γ co-activation, yet the

sequential administration of different PSi NPs showed no effect on intracellular ROS attenuation (**Figure 20C**). In addition, PSi showed no effect on reversing the H_2O_2 induced cellular apoptosis (**Figure 20D**). However, if we pre-incubated PSi with H_2O_2 containing medium for 24 h, further incubating cells with the corresponding pre-treated medium, then only TO could mildly ameliorate the toxicity of H_2O_2 (**Figure 20E**). This can be explained as ROS induced cellular damage that was initiated within 30 min,[260] whereas the ROS scavenging effect from PSi NPs was a rather slow process, as described above. Overall, our results suggested that PSi NPs could consume ROS to undertake an accelerated degradation processes. Nonetheless, this effect might only have a sparing effect on modulating the inflammatory process *in vitro*.

5.5.3 Immune perturbation caused by protein corona formation

Since the reductive nature of PSi back bonds showed limited ROS scavenging effect within a short period, a further mechanism should be proposed to explain the obtained data. Previous studies suggested that the immune response of particles could be primed and regulated via protein corona formation.[265, 266] As such, we hypothesized whether the protein corona of PSi NPs might perturb the inflammation process. First, we roughly checked the different protein binding patterns of different PSi NPs. Blood plasma from ALI mice was collected and incubated with different PSi NPs to form protein corona, and the protein corona composition was investigated by SDS-PAGE (**Supplementary Figure 4** in publication **V**), confirming the surface chemistry dependent protein binding patterns. Protein binding did not only influence the cellular uptake and clearance of the particles under inflammatory conditions, but the synchronously captured/absorbed inflammation related proteins might also interfere with the inflammatory process, as the biological functions of the immobilized proteins/peptides might be altered or even abolished.[267-269]

The following experiments were conducted to confirm the hypothesis. DMEM medium containing 10% of blood plasma from healthy mice or ALI mice were prepared and referred to as healthy medium or ALI medium. As shown in **Figure 21A**, ALI medium induced an pro-inflammatory cascade for murine RAW macrophage cells through increasing the phosphorylation of nuclear factor κB (NF-κB) inhibitor κBα (IκBα), enhancing the expression of NF-κB subunit transcription factor p65 (RELA). However, pre-incubating ALI medium with TO and Un, but not with TC, showed ameliorated NF-κB activations compared to blank ALI medium, which was consistent with *in vivo* results. Further mRNA expression levels associated with key pro-inflammatory cytokines were also evaluated via quantitative PCR. Consistent with the up-mentioned results, ALI medium enhanced the pro-inflammatory gene expression (see **Supplementary Figure 5b** in publication **V**). However, PSi treatment modulated the pro-inflammatory effect of ALI medium to a different extent, where TO showed an enhanced IL-6 expression, but a decreased IL-1β expression. Meanwhile, TC only reduced IL-1β expression, while Un down-regulated the expression of TNF-α and IL-1β (**Figure 21B**, gene expression levels from blank ALI medium were fixed as 1). This phenomenon was most probably induced by the ALI plasma absorption, as sole PSi NPs administration exhibited a different expression profile of these genes (see **Supplementary Figure 5c** in publication **V**). ELISA assay was carried out to observe the cytokines release profiles of the macrophages treated with healthy medium, ALI medium,

and ALI medium pre-treated and containing different PSi NPs. Similar as described above, PSi treatment of ALI medium modulated the pro-inflammatory effect of ALI medium in a surface chemistry dependent manner, as TO and Un significantly reduced all the three cytokines, whereas this effect was retained from TC (See **Figure 5c-d** in publication **V**).

We further applied isobaric tags for Tandem Mass Tag (TMT) method to unravel the composition of each corona complex and in total 4459 types of proteins were identified from the corona complex. Among which, 2123 types of proteins with $P < 0.05$ were considered to obtain a significantly altered affinity towards different PSi based on the one-way analysis of variance (ANOVA), and 1127 of them were mainly captured by TO, whereas the corresponding number for TC and Un were 483 and 513. The proteins were further classified by their subcellular location based on database for annotation, visualization and integrated discovery (DAVID). Noteworthy, the percentage of mitochondrial proteins within the TO-corona complex (22.8%) was significantly higher than TC-corona (13.9%) and Un-corona (12.5%), and Un obtained high percentage of extracellular proteins within its corona complex (TO-corona, 15.1%; TC-corona, 11.0%; Un-corona, 28.5%. See **Figure 4a** in publication **V**). Mitochondrion has been recently highlighted as a key intracellular organelle to release immunostimulatory molecules.[270, 271] It has been previous reported that both whole and fragmented mitochondria had potency in eliciting non-infectious inflammatory responses.[270] Tissue injury releases mitochondrial contents, including proteins and DNA, into the circulation with functionally important immune consequences in activating antigen-presenting cells (e.g., dendritic cells and macrophages).[272, 273]

Under diseased condition, cells would secrete proteins to exert the corresponding molecular functions, and the binding between these proteins with PSi NPs might directly disrupt the biological processes. As such, concerning the cellular localization of the proteins in corona-complex, extracellular or secreted proteins were firstly filtered to conduct further analysis. In total 862 extracellular and secreted proteins were further filtered, and then subjected to biological process (BP) and molecular function (MF) annotations to obtain their biological roles. Among which, the most significant enrichments of biological process were response to stimulus, immune system process and locomotion; the top 3 significant enrichments of molecular function molecular function modulator, ligand binding and chemoattractant (**Figure 21C**), as such, confirming the pro-inflammatory properties of the captured proteins within the corona-complex. Within the 862 types of proteins, 244 of them were directly associated with inflammatory cascade and obtained enough abundance in all three types of corona-complex for conducting relative quantification, and 208 identified proteins with $P < 0.05$ were considered to obtain a significantly altered affinity between different PSi (**Figure 21D**). Based on the relative abundance comparison, 84 types of proteins were mainly enriched in TO-corona and the corresponding number for TC-corona and Un-corona were 33 and 91. This was consistent with the up-described *in vitro* and *in vivo* results as TO and Un showed more significant immune perturbation effects than TC.

Overall, the current study highlighted the altered biological responses of PSi NPs under pathological condition, providing insights for further evaluating the biocompatibility and immunogenicity of other NPs for biomedical usage, as such facilitating the successful clinical translation of nanomaterials.

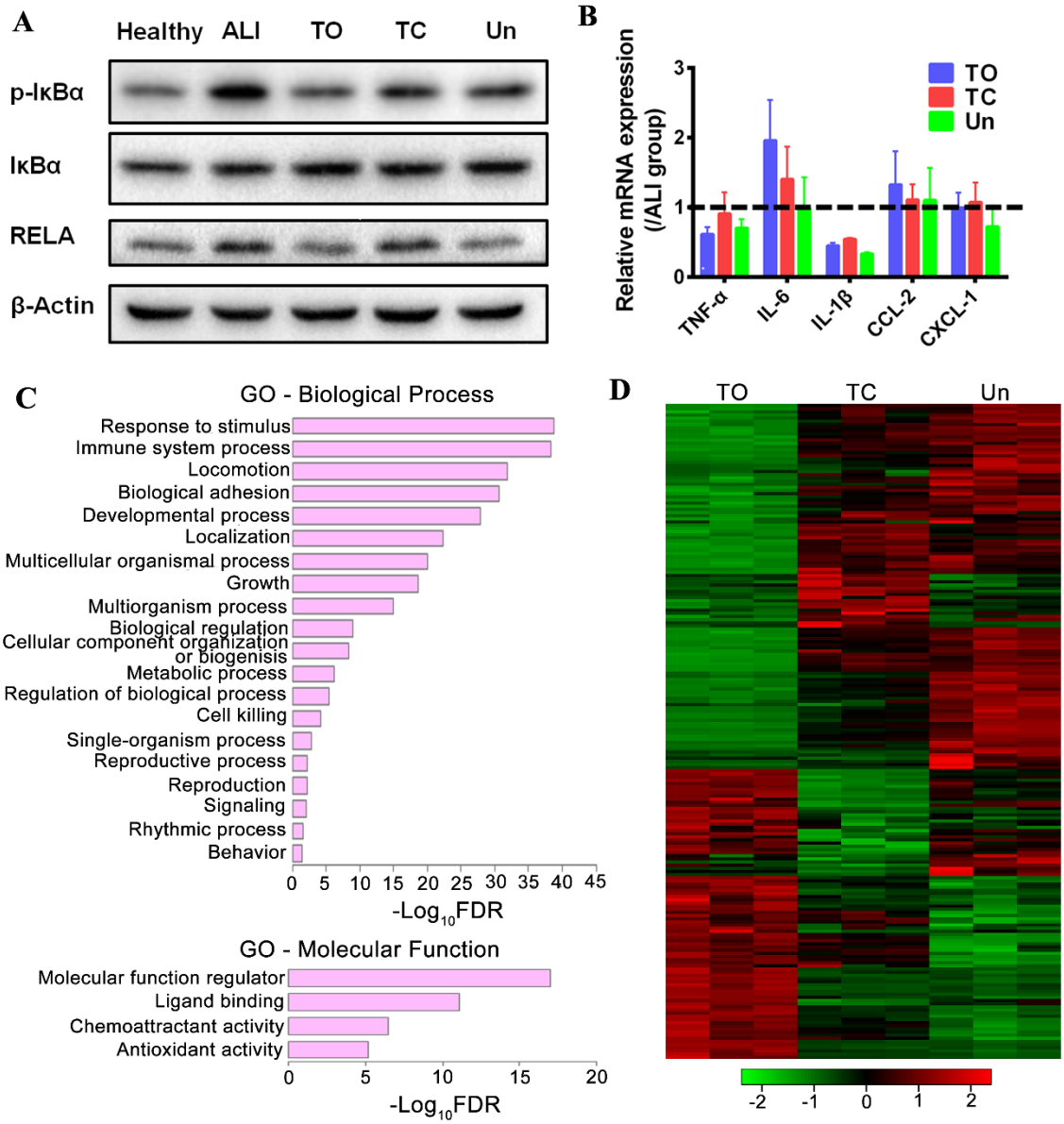

Figure 21. *(A) The effects of healthy, ALI and PSi-treated ALI media on modulating the NK-κB signaling pathway in RAW macrophage cells. (B) qPCR results delineating the pro-inflammatory genes expression level in RAW macrophage cells after healthy, ALI and PSi-treated ALI media treatment. (C) The GO term enrichment of extracellular/secreted proteins in NPs-corona complex. (D) Heat map of 244 pro-inflammatory extracellular/secreted proteins in NPs-corona complex. Log-transformed normalized peak intensities of proteins in each samples were expressed using red, black, or green colors in a heat map (n = 3).*

6 Conclusions

In this dissertation, both chemical modification and physical encapsulation methods were applied to prepare on-demand PSi-based nanohybrids with responsiveness towards specific biological conditions according to the disease characteristics, thus rendering precise control over the loading and release of drugs with different physiochemical properties at desired sites. Convergence of multi-functionalities were achieved within a single nanocarrier by simultaneously incorporating bio-imaging or theranostics modalities, thus shedding light on the potential for multimodal therapeutics.

First, a hydrophilic anti-cancer drug, DOX, was efficiently loaded into a PSi-based pH-responsive DDS. Inspired by the structure of dopamine, a derivative of an anti-cancer flavonoid was synthesized to modify PSi, and further bind with iron ions. A pH-responsive DOX release was achieved via metal-chelation bond breakage and the release process was monitored via fluorescence imaging.

Next, to enhance the tumor targeting ability of a DDS, a specific CA IX targeting ligand, VD11-4-2, was conjugated to PSi. A pH-responsive DOX release behavior was achieved, due to the special fluorescence spectrum of VD11-4-2, and the DOX release was also feasibly monitored by the FRET effect.

To encapsulate a hydrophobic drug, a microfluidic-assisted nanoprecipitation method was employed to produce PSi/Au co-encapsulated nanohybrids. PSi enhanced the loading efficiency of the regenerative drug, while Au was applied for lesion-specific CT imaging. The outer polymer matrix promoted the monodispersity and tailored the release behavior of the system in a pH-dependent manner. The yielded nanohybrids prominently reduced liver damage, improved biosafety by illustrating the liver damage extent, and showed the systems to hold great promise for further personalized treatment.

The co-loading of both hydrophilic and hydrophobic drugs was achieved by fabricating an oxidation/acid dual-responsive nanohybrid/ark system. The microfluidics-produced PSi-based nanohybrids endowed a system with an orchestrated cascade from wound detection, ROS scavenging, drug release, and hydrogel formation. The drug release behavior imitated the dynamic wound healing process, thus rendering an enhanced bio-mimetic regeneration, which demonstrates great potential for diabetic wound healing.

Finally, the immunogenicity and biocompatibility of different PSi under pathological conditions were evaluated. The PSi surface chemistry dependent inflammatory damage amelioration was confirmed to be in virtue of the pervasive, yet miscellaneous protein corona formation, where a myriad of different proteins were bound to different PSi, rendering a perturbation to the inflammatory process.

Overall, several promising PSi-based DDS with multi-functional modalities and on-demand control over drugs release profiles were prepared and characterized. With current works emphasizing the feasibility and advantages in different bio-medical applications, further efforts are still required, e.g., on exploring the potential process and mechanism of the successful core/shell nanostructure formation via microfluidics assisted nanoprecipitation method, further expanding applications in encapsulating biological compounds, such as peptides/proteins, RNA/DNA and even cells.

References

1. Allen, T. M.; Cullis, P. R., Drug delivery systems: entering the mainstream. *Science* **2004,** *303* (5665), 1818-1822.
2. Uhrich, K. E.; Cannizzaro, S. M.; Langer, R. S.; Shakesheff, K. M., Polymeric systems for controlled drug release. *Chem. Rev.* **1999,** *99* (11), 3181-3198.
3. Ganta, S.; Devalapally, H.; Shahiwala, A.; Amiji, M., A review of stimuli-responsive nanocarriers for drug and gene delivery. *J. Controlled Release* **2008,** *126* (3), 187-204.
4. Urtti, A., Challenges and obstacles of ocular pharmacokinetics and drug delivery. *Adv. Drug Delivery Rev.* **2006,** *58* (11), 1131-1135.
5. Kesisoglou, F.; Panmai, S.; Wu, Y., Nanosizing—oral formulation development and biopharmaceutical evaluation. *Adv. Drug Delivery Rev.* **2007,** *59* (7), 631-644.
6. Moghimi, S. M.; Hunter, A. C.; Murray, J. C., Long-circulating and target-specific nanoparticles: theory to practice. *Pharmacol. Rev.* **2001,** *53* (2), 283-318.
7. Ganipineni, L. P.; Danhier, F.; Préat, V., Drug delivery challenges and future of chemotherapeutic nanomedicine for glioblastoma treatment. *J. Controlled Release* **2018,** *281*, 42-57.
8. McCarthy, J. R.; Weissleder, R., Multifunctional magnetic nanoparticles for targeted imaging and therapy. *Adv. Drug Delivery Rev.* **2008,** *60* (11), 1241-1251.
9. Torchilin, V. P., Multifunctional, stimuli-sensitive nanoparticulate systems for drug delivery. *Nat. Rev. Drug Discovery* **2014,** *13* (11), 813.
10. Blanco, E.; Shen, H.; Ferrari, M., Principles of nanoparticle design for overcoming biological barriers to drug delivery. *Nat. Biotechnol.* **2015,** *33* (9), 941.
11. Gabizon, A.; Catane, R.; Uziely, B.; Kaufman, B.; Safra, T.; Cohen, R.; Martin, F.; Huang, A.; Barenholz, Y., Prolonged circulation time and enhanced accumulation in malignant exudates of doxorubicin encapsulated in polyethylene-glycol coated liposomes. *Cancer Res.* **1994,** *54* (4), 987-992.
12. Parhiz, H.; Khoshnejad, M.; Myerson, J. W.; Hood, E.; Patel, P. N.; Brenner, J. S.; Muzykantov, V. R., Unintended effects of drug carriers: Big issues of small particles. *Adv. Drug Delivery Rev.* **2018**.
13. Li, W.; Liu, Z.; Fontana, F.; Ding, Y.; Liu, D.; Hirvonen, J. T.; Santos, H. A., Tailoring Porous Silicon for Biomedical Applications: From Drug Delivery to Cancer Immunotherapy. *Adv. Mater.* **2018**, 1703740.
14. Stewart, M. P.; Buriak, J. M., Chemical and biological applications of porous silicon technology. *Adv. Mater.* **2000,** *12* (12), 859-869.
15. Anglin, E. J.; Cheng, L.; Freeman, W. R.; Sailor, M. J., Porous silicon in drug delivery devices and materials. *Adv. Drug Delivery Rev.* **2008,** *60* (11), 1266-1277.
16. Tasciotti, E.; Liu, X.; Bhavane, R.; Plant, K.; Leonard, A. D.; Price, B. K.; Cheng, M. M.-C.; Decuzzi, P.; Tour, J. M.; Robertson, F., Mesoporous silicon particles as a multistage delivery system for imaging and therapeutic applications. *Nat. Nanotechnol.* **2008,** *3* (3), 151.
17. Park, J.-H.; Gu, L.; Von Maltzahn, G.; Ruoslahti, E.; Bhatia, S. N.; Sailor, M. J., Biodegradable luminescent porous silicon nanoparticles for in vivo applications. *Nat. Mater.* **2009,** *8* (4), 331.
18. Low, S. P.; Voelcker, N. H.; Canham, L. T.; Williams, K. A., The biocompatibility of porous silicon in tissues of the eye. *Biomaterials* **2009,** *30* (15), 2873-2880.
19. Bimbo, L. M.; Mäkilä, E.; Raula, J.; Laaksonen, T.; Laaksonen, P.; Strommer, K.; Kauppinen, E. I.; Salonen, J.; Linder, M. B.; Hirvonen, J., Functional hydrophobin-coating of thermally hydrocarbonized porous silicon microparticles. *Biomaterials* **2011,** *32* (34), 9089-9099.
20. Prestidge, C. A.; Barnes, T. J.; Mierczynska‐Vasilev, A.; Skinner, W.; Peddie, F.; Barnett, C., Loading and release of a model protein from porous silicon powders. *Phys. Status Solidi A* **2007,** *204* (10), 3361-3366.

21. Kinnari, P. J.; Hyvönen, M. L. K.; Mäkilä, E. M.; Kaasalainen, M. H.; Rivinoja, A.; Salonen, J. J.; Hirvonen, J. T.; Laakkonen, P. M.; Santos, H. A., Tumour homing peptide-functionalized porous silicon nanovectors for cancer therapy. *Biomaterials* **2013,** *34* (36), 9134-9141.
22. Liu, D.; Zhang, H.; Herranz‐Blanco, B.; Mäkilä, E.; Lehto, V. P.; Salonen, J.; Hirvonen, J.; Santos, H. A., Microfluidic Assembly of Monodisperse Multistage pH‐Responsive Polymer/Porous Silicon Composites for Precisely Controlled Multi‐Drug Delivery. *Small* **2014,** *10* (10), 2029-2038.
23. Wang, C.-F.; Sarparanta, M. P.; Mäkilä, E. M.; Hyvönen, M. L. K.; Laakkonen, P. M.; Salonen, J. J.; Hirvonen, J. T.; Airaksinen, A. J.; Santos, H. A., Multifunctional porous silicon nanoparticles for cancer theranostics. *Biomaterials* **2015,** *48*, 108-118.
24. Fan, W.; Yung, B. C.; Chen, X., Stimuli‐Responsive NO Release for On‐Demand Gas‐Sensitized Synergistic Cancer Therapy. *Angew. Chem., Int. Ed.* **2018**.
25. Wang, Y.; Kohane, D. S., External triggering and triggered targeting strategies for drug delivery. *Nat. Rev. Mater.* **2017,** *2* (6), 17020.
26. Stuart, M. A. C.; Huck, W. T. S.; Genzer, J.; Müller, M.; Ober, C.; Stamm, M.; Sukhorukov, G. B.; Szleifer, I.; Tsukruk, V. V.; Urban, M., Emerging applications of stimuli-responsive polymer materials. *Nat. Mater.* **2010,** *9* (2), 101.
27. Lavan, D. A.; McGuire, T.; Langer, R., Small-scale systems for in vivo drug delivery. *Nat. Biotechnol.* **2003,** *21* (10), 1184.
28. Shen, B.-Q.; Xu, K.; Liu, L.; Raab, H.; Bhakta, S.; Kenrick, M.; Parsons-Reponte, K. L.; Tien, J.; Yu, S.-F.; Mai, E., Conjugation site modulates the in vivo stability and therapeutic activity of antibody-drug conjugates. *Nat. Biotechnol.* **2012,** *30* (2), 184.
29. Junutula, J. R.; Raab, H.; Clark, S.; Bhakta, S.; Leipold, D. D.; Weir, S.; Chen, Y.; Simpson, M.; Tsai, S. P.; Dennis, M. S., Site-specific conjugation of a cytotoxic drug to an antibody improves the therapeutic index. *Nat. Biotechnol.* **2008,** *26* (8), 925.
30. Zhu, W.; Xiang, G.; Shang, J.; Guo, J.; Motevalli, B.; Durfee, P.; Agola, J. O.; Coker, E. N.; Brinker, C. J., Versatile Surface Functionalization of Metal–Organic Frameworks through Direct Metal Coordination with a Phenolic Lipid Enables Diverse Applications. *Adv. Funct. Mater.* **2018,** *28* (16), 1705274.
31. Li, Y.; Song, L.; Wang, B.; He, J.; Li, Y.; Deng, Z.; Mao, C., Universal pH‐responsive and metal‐ion‐free self‐assembly of DNA nanostructures. *Angew. Chem., Int. Ed.* **2018,** *57* (23), 6892-6895.
32. Karimi, M.; Ghasemi, A.; Zangabad, P. S.; Rahighi, R.; Basri, S. M. M.; Mirshekari, H.; Amiri, M.; Pishabad, Z. S.; Aslani, A.; Bozorgomid, M., Smart micro/nanoparticles in stimulus-responsive drug/gene delivery systems. *Chem. Soc. Rev.* **2016,** *45* (5), 1457-1501.
33. Yang, Y.; Xu, L.; Zhu, W.; Feng, L.; Liu, J.; Chen, Q.; Dong, Z.; Zhao, J.; Liu, Z.; Chen, M., One-pot synthesis of pH-responsive charge-switchable PEGylated nanoscale coordination polymers for improved cancer therapy. *Biomaterials* **2018,** *156*, 121-133.
34. Li, B.; Xie, X.; Chen, Z.; Zhan, C.; Zeng, F.; Wu, S., Tumor Inhibition Achieved by Targeting and Regulating Multiple Key Elements in EGFR Signaling Pathway Using a Self‐Assembled Nanoprodrug. *Adv. Funct. Mater.* **2018,** *28* (22), 1800692.
35. Mout, R.; Moyano, D. F.; Rana, S.; Rotello, V. M., Surface functionalization of nanoparticles for nanomedicine. *Chem. Soc. Rev.* **2012,** *41* (7), 2539-2544.
36. Makila, E.; Ferreira, M. n. P. A.; Kivela, H.; Niemi, S.-M.; Correia, A.; Shahbazi, M.-A.; Kauppila, J.; Hirvonen, J.; Santos, H. A.; Salonen, J., Confinement effects on drugs in thermally hydrocarbonized porous silicon. *Langmuir* **2014,** *30* (8), 2196-2205.
37. Liu, D.; Mäkilä, E.; Zhang, H.; Herranz, B.; Kaasalainen, M.; Kinnari, P.; Salonen, J.; Hirvonen, J.; Santos, H. A., Nanostructured Porous Silicon‐Solid Lipid Nanocomposite: Towards Enhanced Cytocompatibility and Stability, Reduced Cellular Association, and Prolonged Drug Release. *Adv. Funct. Mater.* **2013,** *23* (15), 1893-1902.
38. Whitesides, G. M., The origins and the future of microfluidics. *Nature* **2006,** *442* (7101), 368.
39. Zhang, H.; Liu, D.; Shahbazi, M. A.; Mäkilä, E.; Herranz‐Blanco, B.; Salonen, J.; Hirvonen, J.; Santos, H. A., Fabrication of a Multifunctional Nano‐in‐micro Drug

Delivery Platform by Microfluidic Templated Encapsulation of Porous Silicon in Polymer Matrix. *Adv. Mater.* **2014,** *26* (26), 4497-4503.
40. Hou, X.; Zhang, Y. S.; Trujillo-de Santiago, G.; Alvarez, M. M.; Ribas, J.; Jonas, S. J.; Weiss, P. S.; Andrews, A. M.; Aizenberg, J.; Khademhosseini, A., Interplay between materials and microfluidics. *Nat. Rev. Mater.* **2017,** *2* (5), 17016.
41. Sackmann, E. K.; Fulton, A. L.; Beebe, D. J., The present and future role of microfluidics in biomedical research. *Nature* **2014,** *507* (7491), 181.
42. Stone, H. A.; Stroock, A. D.; Ajdari, A., Engineering flows in small devices: microfluidics toward a lab-on-a-chip. *Annu. Rev. Fluid Mech.* **2004,** *36*, 381-411.
43. Günther, A.; Jensen, K. F., Multiphase microfluidics: from flow characteristics to chemical and materials synthesis. *Lab Chip* **2006,** *6* (12), 1487-1503.
44. Liu, D.; Zhang, H.; Fontana, F.; Hirvonen, J. T.; Santos, H. A., Current developments and applications of microfluidic technology toward clinical translation of nanomedicines. *Adv. Drug Delivery Rev.* **2018,** *128*, 54-83.
45. Sanjay, S. T.; Zhou, W.; Dou, M.; Tavakoli, H.; Ma, L.; Xu, F.; Li, X., Recent advances of controlled drug delivery using microfluidic platforms. *Adv. Drug Delivery Rev.* **2017**.
46. Matsumura, Y.; Maeda, H., A new concept for macromolecular therapeutics in cancer chemotherapy: mechanism of tumoritropic accumulation of proteins and the antitumor agent smancs. *Cancer Res.* **1986,** *46* (12 Part 1), 6387-6392.
47. Sigovan, M.; Boussel, L.; Sulaiman, A.; Sappey-Marinier, D.; Alsaid, H.; Desbleds-Mansard, C.; Ibarrola, D.; Gamondès, D.; Corot, C.; Lancelot, E., Rapid-clearance iron nanoparticles for inflammation imaging of atherosclerotic plaque: initial experience in animal model. *Radiology* **2009,** *252* (2), 401-409.
48. Möllmann, U.; Heinisch, L.; Bauernfeind, A.; Köhler, T.; Ankel-Fuchs, D., Siderophores as drug delivery agents: application of the "Trojan Horse" strategy. *Biometals* **2009,** *22* (4), 615-624.
49. Wagner, V.; Dullaart, A.; Bock, A.-K.; Zweck, A., The emerging nanomedicine landscape. *Nat. Biotechnol.* **2006,** *24* (10), 1211.
50. Merisko-Liversidge, E.; Liversidge, G. G., Nanosizing for oral and parenteral drug delivery: a perspective on formulating poorly-water soluble compounds using wet media milling technology. *Adv. Drug Delivery Rev.* **2011,** *63* (6), 427-440.
51. Nishiyama, N., Nanomedicine: nanocarriers shape up for long life. *Nat. Nanotechnol.* **2007,** *2* (4), 203.
52. Zagorovsky, K.; Chan, W. C. W., Bioimaging: illuminating the deep. *Nat. Mater.* **2013,** *12* (4), 285.
53. Sanhai, W. R.; Sakamoto, J. H.; Canady, R.; Ferrari, M., Seven challenges for nanomedicine. *Nat. Nanotechnol.* **2008,** *3* (5), 242.
54. Tsoi, K. M.; MacParland, S. A.; Ma, X.-Z.; Spetzler, V. N.; Echeverri, J.; Ouyang, B.; Fadel, S. M.; Sykes, E. A.; Goldaracena, N.; Kaths, J. M., Mechanism of hard-nanomaterial clearance by the liver. *Nat. Mater.* **2016,** *15* (11), 1212.
55. Wilhelm, S.; Tavares, A. J.; Dai, Q.; Ohta, S.; Audet, J.; Dvorak, H. F.; Chan, W. C. W., Analysis of nanoparticle delivery to tumours. *Nat. Rev. Mater.* **2016,** *1* (5), 16014.
56. Gillies, R. J.; Verduzco, D.; Gatenby, R. A., Evolutionary dynamics of carcinogenesis and why targeted therapy does not work. *Nat. Rev. Cancer* **2012,** *12* (7), 487.
57. Ernsting, M. J.; Murakami, M.; Roy, A.; Li, S.-D., Factors controlling the pharmacokinetics, biodistribution and intratumoral penetration of nanoparticles. *J. Controlled Release* **2013,** *172* (3), 782-794.
58. Tan, Y. F.; Lao, L. L.; Xiong, G. M.; Venkatraman, S., Controlled-release nanotherapeutics: State of translation. *J. Controlled Release* **2018,** *284*, 39-48.
59. Mura, S.; Nicolas, J.; Couvreur, P., Stimuli-responsive nanocarriers for drug delivery. *Nat. Mater.* **2013,** *12* (11), 991.
60. Mohammed, J. S.; Murphy, W. L., Bioinspired design of dynamic materials. *Adv. Mater.* **2009,** *21* (23), 2361-2374.

61. Zhou, J.; Tian, G.; Zeng, L.; Song, X.; Bian, X. w., Nanoscaled Metal‐Organic Frameworks for Biosensing, Imaging, and Cancer Therapy. *Adv. Healthcare Mater.* **2018**, 1800022.
62. Li, X.; Kim, J.; Yoon, J.; Chen, X., Cancer‐Associated, Stimuli‐Driven, Turn on Theranostics for Multimodality Imaging and Therapy. *Adv. Mater.* **2017,** *29* (23), 1606857.
63. Mu, J.; Lin, J.; Huang, P.; Chen, X., Development of endogenous enzyme-responsive nanomaterials for theranostics. *Chem. Soc. Rev.* **2018**.
64. Du, J.; Lane, L. A.; Nie, S., Stimuli-responsive nanoparticles for targeting the tumor microenvironment. *J. Controlled Release* **2015,** *219*, 205-214.
65. Lu, Y.; Aimetti, A. A.; Langer, R.; Gu, Z., Bioresponsive materials. *Nat. Rev. Mater.* **2017,** *2* (1), 16075.
66. Han, X.; Huang, J.; Lin, H.; Wang, Z.; Li, P.; Chen, Y., 2D Ultrathin MXene‐Based Drug‐Delivery Nanoplatform for Synergistic Photothermal Ablation and Chemotherapy of Cancer. *Adv. Healthcare Mater.* **2018,** *7* (9), 1701394.
67. Bazban-Shotorbani, S.; Hasani-Sadrabadi, M. M.; Karkhaneh, A.; Serpooshan, V.; Jacob, K. I.; Moshaverinia, A.; Mahmoudi, M., Revisiting structure-property relationship of pH-responsive polymers for drug delivery applications. *J. Controlled Release* **2017,** *253*, 46-63.
68. Corbet, C.; Feron, O., Tumour acidosis: from the passenger to the driver's seat. *Nat. Rev. Cancer* **2017,** *17* (10), 577-593.
69. Parks, S. K.; Chiche, J.; Pouysségur, J., Disrupting proton dynamics and energy metabolism for cancer therapy. *Nat. Rev. Cancer* **2013,** *13* (9), 611.
70. Schulze, A.; Harris, A. L., How cancer metabolism is tuned for proliferation and vulnerable to disruption. *Nature* **2012,** *491* (7424), 364.
71. Supuran, C. T., Carbonic anhydrases: novel therapeutic applications for inhibitors and activators. *Nat. Rev. Drug Discovery* **2008,** *7* (2), 168.
72. He, D.; Yang, T.; Qian, W.; Qi, C.; Mao, L.; Yu, X.; Zhu, H.; Luo, G.; Deng, J., Combined photothermal and antibiotic therapy for bacterial infection via acidity-sensitive nanocarriers with enhanced antimicrobial performance. *Appl. Mater. Today* **2018,** *12*, 415-429.
73. Morey, M.; Pandit, A., Responsive triggering systems for delivery in chronic wound healing. *Adv. Drug Delivery Rev.* **2018**.
74. Ohkuma, S.; Poole, B., Fluorescence probe measurement of the intralysosomal pH in living cells and the perturbation of pH by various agents. *Proc. Natl. Acad. Sci. U. S. A.* **1978,** *75* (7), 3327-3331.
75. Lesniak, A.; Fenaroli, F.; Monopoli, M. P.; Åberg, C.; Dawson, K. A.; Salvati, A., Effects of the presence or absence of a protein corona on silica nanoparticle uptake and impact on cells. *ACS Nano* **2012,** *6* (7), 5845-5857.
76. Zhang, S.; Li, J.; Lykotrafitis, G.; Bao, G.; Suresh, S., Size‐dependent endocytosis of nanoparticles. *Adv. Mater.* **2009,** *21* (4), 419-424.
77. Hider, R. C.; Liu, Z. D.; Khodr, H. H., Metal chelation of polyphenols. *Methods Enzymol.* **2001,** *335* (335), 190-203.
78. Mauro, M., Dynamic metal-ligand bonds as scaffold towards autonomously healable multi-responsive materials. *Eur. J. Inorg. Chem.* **2018,** *2018* (20-21), 2090-2100.
79. Zheng, X.; Zhang, J.; Wang, J.; Qi, X.; Rosenholm, J. M.; Cai, K., Polydopamine coatings in confined nanopore space: toward improved retention and release of hydrophilic cargo. *J. Phys. Chem. C* **2015,** *119* (43), 24512-24521.
80. Myers, C. E.; Gianni, L.; Simone, C. B.; Klecker, R.; Greene, R., Oxidative destruction of erythrocyte ghost membranes catalyzed by the doxorubicin-iron complex. *Biochemistry* **1982,** *21* (8), 1707.
81. Raghunand, N.; He, X.; Van Sluis, R.; Mahoney, B.; Baggett, B.; Taylor, C.; Paine-Murrieta, G.; Roe, D.; Bhujwalla, Z.; Gillies, R., Enhancement of chemotherapy by manipulation of tumour pH. *Br. J. Cancer* **1999,** *80* (7), 1005.
82. Xu, X.; Persson, H. L.; Richardson, D. R., Molecular pharmacology of the interaction of anthracyclines with iron. *Mol. Pharmacol.* **2005,** *68* (2), 261-71.

83. Liu, P.; Chen, M.; Chen, C.; Fang, X.; Chen, X.; Zheng, N., An iron silicate based pH-sensitive drug delivery system utilizing coordination bonding. *J. Mater. Chem. B* **2013,** *1* (22), 2837-2842.
84. Liu, Z.; Tang, S.; Xu, Z.; Wang, Y.; Zhu, X.; Li, L.-c.; Hong, W.; Wang, X., Preparation and in vitro evaluation of a multifunctional iron silicate@ liposome nanohybrid for pH-sensitive doxorubicin delivery and photoacoustic imaging. *J. Nanomater.* **2015,** *16* (1), 44.
85. Chen, M.-C.; Mi, F.-L.; Liao, Z.-X.; Hsiao, C.-W.; Sonaje, K.; Chung, M.-F.; Hsu, L.-W.; Sung, H.-W., Recent advances in chitosan-based nanoparticles for oral delivery of macromolecules. *Adv. Drug Delivery Rev.* **2013,** *65* (6), 865-879.
86. Yu, H.; Zou, Y.; Wang, Y.; Huang, X.; Huang, G.; Sumer, B. D.; Boothman, D. A.; Gao, J., Overcoming endosomal barrier by amphotericin B-loaded dual pH-responsive PDMA-b-PDPA micelleplexes for siRNA delivery. *ACS Nano* **2011,** *5* (11), 9246-9255.
87. Li, Y.; Wang, Z.; Wei, Q.; Luo, M.; Huang, G.; Sumer, B. D.; Gao, J., Non-covalent interactions in controlling pH-responsive behaviors of self-assembled nanosystems. *Polym. Chem.* **2016,** *7* (38), 5949-5956.
88. Wu, W.; Chen, M.; Wang, J.; Zhang, Q.; Li, S.; Lin, Z.; Li, J., Nanocarriers with dual pH-sensitivity for enhanced tumor cell uptake and rapid intracellular drug release. *RSC Adv.* **2014,** *4* (58), 30780-30783.
89. Zhang, C.; An, T.; Wang, D.; Wan, G.; Zhang, M.; Wang, H.; Zhang, S.; Li, R.; Yang, X.; Wang, Y., Stepwise pH-responsive nanoparticles containing charge-reversible pullulan-based shells and poly (β-amino ester)/poly (lactic-co-glycolic acid) cores as carriers of anticancer drugs for combination therapy on hepatocellular carcinoma. *J. Controlled Release* **2016,** *226*, 193-204.
90. Han, S. S.; Li, Z. Y.; Zhu, J. Y.; Han, K.; Zeng, Z. Y.; Hong, W.; Li, W. X.; Jia, H. Z.; Liu, Y.; Zhuo, R. X., Dual-pH Sensitive Charge-Reversal Polypeptide Micelles for Tumor-Triggered Targeting Uptake and Nuclear Drug Delivery. *Small* **2015,** *11* (21), 2543-2554.
91. Liu, P.; Xu, G.; Pranantyo, D.; Xu, L.; Neoh, K.; Kang, E., pH-Sensitive Zwitterionic Polymer as an Antimicrobial Agent with Effective Bacterial Targeting. *ACS Biomater. Sci. Eng.* **2017,** *4* (1), 40-46.
92. Hu, J.; Quan, Y.; Lai, Y.; Zheng, Z.; Hu, Z.; Wang, X.; Dai, T.; Zhang, Q.; Cheng, Y., A smart aminoglycoside hydrogel with tunable gel degradation, on-demand drug release, and high antibacterial activity. *J. Controlled Release* **2017,** *247*, 145-152.
93. Gao, D.; Lo, P.-C., Polymeric micelles encapsulating pH-responsive doxorubicin prodrug and glutathione-activated zinc (II) phthalocyanine for combined chemotherapy and photodynamic therapy. *J. Controlled Release* **2018**.
94. Bachelder, E. M.; Beaudette, T. T.; Broaders, K. E.; Dashe, J.; Fréchet, J. M. J., Acetal-derivatized dextran: an acid-responsive biodegradable material for therapeutic applications. *J. Am. Chem. Soc.* **2008,** *130* (32), 10494-10495.
95. Arno, M. C.; Brannigan, R. P.; Policastro, G. M.; Becker, M. L.; Dove, A. P., pH Responsive, Functionalizable Spyrocyclic Polycarbonate: A Versatile Platform for Biocompatible Nanoparticles. *Biomacromolecules* **2018**.
96. Liu, D.; Zhang, H.; Mäkilä, E.; Fan, J.; Herranz-Blanco, B.; Wang, C.-F.; Rosa, R.; Ribeiro, A. J.; Salonen, J.; Hirvonen, J., Microfluidic assisted one-step fabrication of porous silicon@ acetalated dextran nanocomposites for precisely controlled combination chemotherapy. *Biomaterials* **2015,** *39*, 249-259.
97. Kalia, J.; Raines, R. T., Hydrolytic stability of hydrazones and oximes. *Angew. Chem., Int. Ed.* **2008,** *47* (39), 7523-7526.
98. Trachootham, D.; Alexandre, J.; Huang, P., Targeting cancer cells by ROS-mediated mechanisms: a radical therapeutic approach? *Nat. Rev. Drug Discovery* **2009,** *8* (7), 579.
99. Blanco, F. J.; Valdes, A. M.; Rego-Pérez, I., Mitochondrial DNA variation and the pathogenesis of osteoarthritis phenotypes. *Nat. Rev. Rheumatol.* **2018,** *14*, 327-40.
100. Koelwyn, G. J.; Corr, E. M.; Erbay, E.; Moore, K. J., Regulation of macrophage immunometabolism in atherosclerosis. *Nat. Immunol.* **2018**, 1.

101. Cano, M. S.; Lancel, S.; Boulanger, E.; Neviere, R., Targeting Oxidative Stress and Mitochondrial Dysfunction in the Treatment of Impaired Wound Healing: A Systematic Review. *Antioxidants* **2018,** *7* (8).
102. Schuster, S.; Cabrera, D.; Arrese, M.; Feldstein, A. E., Triggering and resolution of inflammation in NASH. *Nat. Rev. Gastroenterol. Hepatol.* **2018,** *15* (6), 349-364.
103. de Gracia Lux, C.; Joshi-Barr, S.; Nguyen, T.; Mahmoud, E.; Schopf, E.; Fomina, N.; Almutairi, A., Biocompatible polymeric nanoparticles degrade and release cargo in response to biologically relevant levels of hydrogen peroxide. *J. Am. Chem. Soc.* **2012,** *134* (38), 15758-15764.
104. Broaders, K. E.; Grandhe, S.; Fréchet, J. M., A biocompatible oxidation-triggered carrier polymer with potential in therapeutics. *J. Am. Chem. Soc.* **2010,** *133* (4), 756-758.
105. Tao, W.; He, Z., ROS-responsive drug delivery systems for biomedical applications. *Asian J. Pharm. Sci.* **2017,** *13* (2), 101-112.
106. Napoli, A.; Valentini, M.; Tirelli, N.; Müller, M.; Hubbell, J. A., Oxidation-responsive polymeric vesicles. *Nat. Mater.* **2004,** *3* (3), 183-189.
107. Lee, S. H.; Gupta, M. K.; Bang, J. B.; Bae, H.; Sung, H. J., Current Progress in Reactive Oxygen Species (ROS) ‐ Responsive Materials for Biomedical Applications. *Adv. Healthcare Mater.* **2013,** *2* (6), 908-915.
108. Poole, K. M.; Nelson, C. E.; Joshi, R. V.; Martin, J. R.; Gupta, M. K.; Haws, S. C.; Kavanaugh, T. E.; Skala, M. C.; Duvall, C. L., ROS-responsive microspheres for on demand antioxidant therapy in a model of diabetic peripheral arterial disease. *Biomaterials* **2015,** *41*, 166-175.
109. Rehor, A.; Hubbell, J. A.; Tirelli, N., Oxidation-sensitive polymeric nanoparticles. *Langmuir* **2005,** *21* (1), 411-417.
110. Allen, B. L.; Johnson, J. D.; Walker, J. P., Encapsulation and enzyme-mediated release of molecular cargo in polysulfide nanoparticles. *ACS Nano* **2011,** *5* (6), 5263-72.
111. Gupta, M. K.; Meyer, T. A.; Nelson, C. E.; Duvall, C. L. J. J. o. C. R., Poly(PS-b-DMA) Micelles for Reactive Oxygen Species Triggered Drug Release. *J. Controlled Release* **2012,** *162* (3), 591-598.
112. Poole, K. M.; Nelson, C. E.; Joshi, R. V.; Martin, J. R.; Gupta, M. K.; Haws, S. C.; Kavanaugh, T. E.; Skala, M. C.; Duvall, C. L. J. B., ROS-Responsive Microspheres for On Demand Antioxidant Therapy in a Model of Diabetic Peripheral Arterial Disease. *Biomaterials* **2015,** *41* (41C), 166-175.
113. Savina, A.; Peres, A.; Cebrian, I.; Carmo, N.; Moita, C.; Hacohen, N.; Moita, L. F.; Amigorena, S., The small GTPase Rac2 controls phagosomal alkalinization and antigen crosspresentation selectively in CD8(+) dendritic cells. *Immunity* **2009,** *30* (4), 544-555.
114. Dowling, D. J.; Scott, E. A.; Scheid, A.; Bergelson, I.; Joshi, S.; Pietrasanta, C.; Brightman, S.; Sanchez-Schmitz, G.; Van Haren, S. D.; Ninković, J., Toll-like receptor 8 agonist nanoparticles mimic immunomodulating effects of the live BCG vaccine and enhance neonatal innate and adaptive immune responses. *J. Allergy Clin. Immunol.* **2017,** *140* (5), 1339-1350.
115. Tapeinos, C.; Pandit, A., Physical, Chemical, and Biological Structures based on ROS ‐ Sensitive Moieties that are Able to Respond to Oxidative Microenvironments. *Adv. Mater.* **2016,** *28* (27), 5553-5585.
116. Song, C.-C.; Du, F.-S.; Li, Z.-C., Oxidation-responsive polymers for biomedical applications. *J. Mater. Chem. B* **2014,** *2* (22), 3413-3426.
117. Hu, X.; Yu, J.; Qian, C.; Lu, Y.; Kahkoska, A. R.; Xie, Z.; Jing, X.; Buse, J. B.; Gu, Z., H2O2-responsive vesicles integrated with transcutaneous patches for glucose-mediated insulin delivery. *ACS Nano* **2017,** *11* (1), 613-620.
118. Zhang, D.; Wei, Y.; Chen, K.; Zhang, X.; Xu, X.; Shi, Q.; Han, S.; Chen, X.; Gong, H.; Li, X., Biocompatible reactive oxygen species (ROS) ‐ responsive nanoparticles as superior drug delivery vehicles. *Adv. Healthcare Mater.* **2015,** *4* (1), 69-76.
119. Jeanmaire, D.; Laliturai, J.; Almalik, A.; Carampin, P.; d'Arcy, R.; Lallana, E.; Evans, R.; Winpenny, R. E. P.; Tirelli, N., Chemical specificity in REDOX-responsive materials: the diverse effects of different reactive oxygen species (ROS) on polysulfide nanoparticles. *Polym. Chem.* **2014,** *5* (4), 1393-1404.

120. Zhou, L.; Qiu, T.; Lv, F.; Liu, L.; Ying, J.; Wang, S., Self‐Assembled Nanomedicines for Anticancer and Antibacterial Applications. *Adv. Healthcare Mater.* **2018**, 1800670.
121. Zhai, S.; Hu, X.; Hu, Y.; Wu, B.; Xing, D., Visible light-induced crosslinking and physiological stabilization of diselenide-rich nanoparticles for redox-responsive drug release and combination chemotherapy. *Biomaterials* **2017,** *121*, 41-54.
122. Ma, N.; Li, Y.; Xu, H.; Wang, Z.; Zhang, X., Dual redox responsive assemblies formed from diselenide block copolymers. *J. Am. Chem. Soc.* **2009,** *132* (2), 442-443.
123. Shi, S.; Zhang, L.; Zhu, M.; Wan, G.; Li, C.; Zhang, J.; Wang, Y.; Wang, Y., ROS-Responsive Nanoparticles Based on PEGlated Prodrug for Targeted Treatment of Oral Tongue Squamous Cell Carcinoma by Combining Photodynamic Therapy and Chemotherapy. *ACS Appl. Mater. Interfaces* **2018**.
124. Xu, X.; Saw, P. E.; Tao, W.; Li, Y.; Ji, X.; Bhasin, S.; Liu, Y.; Ayyash, D.; Rasmussen, J.; Huo, M., ROS‐responsive polyprodrug nanoparticles for triggered drug delivery and effective cancer therapy. *Adv. Mater.* **2017,** *29* (33), 1700141.
125. Xu, L.; Zhao, M.; Yang, Y.; Liang, Y.; Sun, C.; Gao, W.; Li, S.; He, B.; Pu, Y., A reactive oxygen species (ROS)-responsive low molecular weight gel co-loaded with doxorubicin and Zn (ii) phthalocyanine tetrasulfonic acid for combined chemo-photodynamic therapy. *J. Mater. Chem. B* **2017,** *5* (46), 9157-9164.
126. Li, J.; Dirisala, A.; Ge, Z.; Wang, Y.; Yin, W.; Ke, W.; Toh, K.; Xie, J.; Matsumoto, Y.; Anraku, Y., Therapeutic Vesicular Nanoreactors with Tumor‐Specific Activation and Self‐Destruction for Synergistic Tumor Ablation. *Angew. Chem.* **2017,** *129* (45), 14213-14218.
127. Li, J.; Ke, W.; Wang, L.; Huang, M.; Yin, W.; Zhang, P.; Chen, Q.; Ge, Z., Self-sufficing H2O2-responsive nanocarriers through tumor-specific H2O2 production for synergistic oxidation-chemotherapy. *J. Controlled Release* **2016,** *225*, 64-74.
128. Lee, D.; Khaja, S.; Velasquezcastano, J. C.; Dasari, M.; Sun, C.; Petros, J.; Taylor, W. R.; Murthy, N., In vivo imaging of hydrogen peroxide with chemiluminescent nanoparticles. *Nat. Mater.* **2007,** *6* (10), 765-769.
129. Tauschmann, M.; Hovorka, R., Technology in the management of type 1 diabetes mellitus—current status and future prospects. *Nat. Rev. Endocrinol.* **2018**, 1.
130. Fan, W.; Lu, N.; Huang, P.; Liu, Y.; Yang, Z.; Wang, S.; Yu, G.; Liu, Y.; Hu, J.; He, Q., Glucose‐Responsive Sequential Generation of Hydrogen Peroxide and Nitric Oxide for Synergistic Cancer Starving‐Like/Gas Therapy. *Angew. Chem., Int. Ed.* **2017,** *56* (5), 1229-1233.
131. Brooks, W. L.; Sumerlin, B. S., Synthesis and Applications of Boronic Acid-Containing Polymers: From Materials to Medicine. *Chem. Rev.* **2016,** *116* (3), 1375.
132. Sun, X.; James, T. D., Glucose Sensing in Supramolecular Chemistry. *Chem. Rev.* **2015,** *115* (15), 8001.
133. Chou, D. H.-C.; Webber, M. J.; Tang, B. C.; Lin, A. B.; Thapa, L. S.; Deng, D.; Truong, J. V.; Cortinas, A. B.; Langer, R.; Anderson, D. G., Glucose-responsive insulin activity by covalent modification with aliphatic phenylboronic acid conjugates. *Proc. Natl. Acad. Sci. U. S. A.* **2015,** *112* (8), 2401-2406.
134. Brownlee, M.; Cerami, A., A glucose-controlled insulin-delivery system: semisynthetic insulin bound to lectin. *Science* **1979,** *206* (4423), 1190.
135. Liu, F.; †, S. C. S.; Mix, D.; Miroslav Baudyš, A.; Kim, S. W., Glucose-Induced Release of Glycosylpoly(ethylene glycol) Insulin Bound to a Soluble Conjugate of Concanavalin A. *Bioconjugate Chem.* **2000,** *8* (5), 664.
136. Fu, L.-H.; Qi, C.; Lin, J.; Huang, P., Catalytic chemistry of glucose oxidase in cancer diagnosis and treatment. *Chem. Soc. Rev.* **2018**.
137. Wang, C.; Ye, Y.; Sun, W.; Yu, J.; Wang, J.; Lawrence, D. S.; Buse, J. B.; Gu, Z., Red Blood Cells for Glucose‐Responsive Insulin Delivery. *Adv. Mater.* **2017,** *29* (18), 1606617.
138. Yu, J.; Qian, C.; Zhang, Y.; Cui, Z.; Zhu, Y.; Shen, Q.; Ligler, F. S.; Buse, J. B.; Gu, Z., Hypoxia and H2O2 dual-sensitive vesicles for enhanced glucose-responsive insulin delivery. *Nano Lett.* **2017,** *17* (2), 733-739.

139. Gu, Z.; Aimetti, A. A.; Wang, Q.; Dang, T. T.; Zhang, Y.; Veiseh, O.; Cheng, H.; Langer, R. S.; Anderson, D. G., Injectable nano-network for glucose-mediated insulin delivery. *ACS Nano* **2013,** *7* (5), 4194-4201.
140. Ravaine, V.; Ancla, C.; Catargi, B., Chemically controlled closed-loop insulin delivery. *J. Controlled Release* **2008,** *132* (1), 2-11.
141. Søndergaard, R. V.; Christensen, N. M.; Henriksen, J. R.; Kumar, E. K. P.; Almdal, K.; Andresen, T. L., Facing the design challenges of particle-based nanosensors for metabolite quantification in living cells. *Chem. Rev.* **2015,** *115* (16), 8344-8378.
142. Almdal, K.; Sun, H.; Poulsen, A. K.; Arleth, L.; Jakobsen, I.; Gu, H.; Scharff‐Poulsen, A. M., Fluorescent gel particles in the nanometer range for detection of metabolites in living cells. *Polym. Adv. Technol.* **2006,** *17* (9‐10), 790-793.
143. Rink, T. J.; Tsien, R. Y.; Pozzan, T., Cytoplasmic pH and free Mg2+ in lymphocytes. *J. Cell Biol.* **1982,** *95* (1), 189-196.
144. Peng, J.; He, X.; Wang, K.; Tan, W.; Wang, Y.; Liu, Y., Noninvasive monitoring of intracellular pH change induced by drug stimulation using silica nanoparticle sensors. *Anal. Bioanal. Chem.* **2007,** *388* (3), 645-654.
145. Formica, J. V.; Regelson, W., Review of the biology of quercetin and related bioflavonoids. *Food Chem. Toxicol.* **1995,** *33* (12), 1061-1080.
146. Carvalho, J. M.; Leandro, K. C.; da Silva, A. R.; Aucélio, R. Q., Selective determination of rutin by fluorescence attenuation of the CdS-2-mercaptopropionic acid nanocrystal probe. *Anal. Lett.* **2013,** *46* (1), 207-224.
147. Hu, W.-P.; Cao, G.-D.; Dong, W.; Shen, H.-B.; Liu, X.-H.; Li, L.-S., Interaction of quercetin with aqueous CdSe/ZnS quantum dots and the possible fluorescence probes for flavonoids. *Anal. Methods* **2014,** *6* (5), 1442-1447.
148. Jeyadevi, R.; Sivasudha, T.; Rameshkumar, A.; Ananth, D. A.; Aseervatham, G. S. B.; Kumaresan, K.; Kumar, L. D.; Jagadeeswari, S.; Renganathan, R., Enhancement of anti arthritic effect of quercetin using thioglycolic acid-capped cadmium telluride quantum dots as nanocarrier in adjuvant induced arthritic Wistar rats. *Colloids Surf., B* **2013,** *112*, 255-263.
149. Nagel, G.; Tschiche, H. R.; Wedepohl, S.; Calderón, M., Modular approach for theranostic polymer conjugates with activatable fluorescence: Impact of linker design on the stimuli-induced release of doxorubicin. *J. Controlled Release* **2018**.
150. Clegg, R. M., Fluorescence resonance energy transfer. *Curr. Opin. Biotechnol.* **1995,** *6* (1), 103-110.
151. Wu, P. G.; Brand, L., Resonance energy transfer: methods and applications. *Anal. Biochem.* **1994,** *218* (1), 1-13.
152. Piston, D. W.; Kremers, G.-J., Fluorescent protein FRET: the good, the bad and the ugly. *Trends Biochem. Sci.* **2007,** *32* (9), 407-414.
153. Sparks, H.; Kondo, H.; Hooper, S.; Munro, I.; Kennedy, G.; Dunsby, C.; French, P.; Sahai, E., Heterogeneity in tumor chromatin-doxorubicin binding revealed by in vivo fluorescence lifetime imaging confocal endomicroscopy. *Nat. Commun.* **2018,** *9* (1), 2662.
154. Senthilkumar, T.; Zhou, L.; Gu, Q.; Liu, L.; Lv, F.; Wang, S., Conjugated Polymer Nanoparticles with Appended Photo‐Responsive Units for Controlled Drug Delivery, Release, and Imaging. *Angew. Chem., Int. Ed.* **2018,** *57* (40), 13114-13119.
155. Sharma, P.; Brown, S.; Walter, G.; Santra, S.; Moudgil, B., Nanoparticles for bioimaging. *Adv. Colloid Interface Sci.* **2006,** *123*, 471-485.
156. Lee, J.-H.; Huh, Y.-M.; Jun, Y.-w.; Seo, J.-w.; Jang, J.-t.; Song, H.-T.; Kim, S.; Cho, E.-J.; Yoon, H.-G.; Suh, J.-S., Artificially engineered magnetic nanoparticles for ultra-sensitive molecular imaging. *Nat. Med.* **2007,** *13* (1), 95.
157. Kim, D.; Jeong, Y. Y.; Jon, S., A drug-loaded aptamer− gold nanoparticle bioconjugate for combined CT imaging and therapy of prostate cancer. *ACS Nano* **2010,** *4* (7), 3689-3696.
158. Huang, P.; Lin, J.; Li, W.; Rong, P.; Wang, Z.; Wang, S.; Wang, X.; Sun, X.; Aronova, M.; Niu, G., Biodegradable gold nanovesicles with an ultrastrong plasmonic coupling effect for photoacoustic imaging and photothermal therapy. *Angew. Chem., Int. Ed.* **2013,** *52* (52), 13958-13964.

159. Kircher, M. F.; De La Zerda, A.; Jokerst, J. V.; Zavaleta, C. L.; Kempen, P. J.; Mittra, E.; Pitter, K.; Huang, R.; Campos, C.; Habte, F., A brain tumor molecular imaging strategy using a new triple-modality MRI-photoacoustic-Raman nanoparticle. *Nat. Med.* **2012,** *18* (5), 829.
160. Wang, S.; Huang, P.; Chen, X., Hierarchical Targeting Strategy for Enhanced Tumor Tissue Accumulation/Retention and Cellular Internalization. *Adv. Mater.* **2016,** *28* (34), 7340-7364.
161. De Jong, W. H.; Hagens, W. I.; Krystek, P.; Burger, M. C.; Sips, A. J. A. M.; Geertsma, R. E., Particle size-dependent organ distribution of gold nanoparticles after intravenous administration. *Biomaterials* **2008,** *29* (12), 1912-1919.
162. Zhang, X.-D.; Wu, D.; Shen, X.; Liu, P.-X.; Fan, F.-Y.; Fan, S.-J., In vivo renal clearance, biodistribution, toxicity of gold nanoclusters. *Biomaterials* **2012,** *33* (18), 4628-4638.
163. Li, X.; Hu, Z.; Ma, J.; Wang, X.; Zhang, Y.; Wang, W.; Yuan, Z., The systematic evaluation of size-dependent toxicity and multi-time biodistribution of gold nanoparticles. *Colloids Surf., B* **2018,** *167*, 260-266.
164. Yu, M.; Zheng, J., Clearance pathways and tumor targeting of imaging nanoparticles. *ACS Nano* **2015,** *9* (7), 6655-6674.
165. Arvizo, R. R.; Miranda, O. R.; Moyano, D. F.; Walden, C. A.; Karuna, G.; Resham, B.; David, R. J.; Rotello, V. M.; Reid, J. M.; Priyabrata, M., Modulating Pharmacokinetics, Tumor Uptake and Biodistribution by Engineered Nanoparticles. *Plos One* **2011,** *6* (9), e24374.
166. Mao, W.; Kim, H. S.; Son, Y. J.; Kim, S. R.; Yoo, H. S., Doxorubicin encapsulated clicked gold nanoparticle clusters exhibiting tumor-specific disassembly for enhanced tumor localization and computerized tomographic imaging. *J. Controlled Release* **2018,** *269*, 52-62.
167. Lu, J.; Sun, J.; Li, F.; Wang, J.; Liu, J.; Kim, D.; Fan, C.; Hyeon, T.; Ling, D., Highly Sensitive Diagnosis of Small Hepatocellular Carcinoma Using pH-Responsive Iron Oxide Nanocluster Assemblies. *J. Am. Chem. Soc.* **2018**.
168. Uhlir Jr, A., Electrolytic shaping of germanium and silicon. *Bell Syst. Tech. J.* **1956,** *35* (2), 333-347.
169. Canham, L. T., Silicon quantum wire array fabrication by electrochemical and chemical dissolution of wafers. *Appl. Phys. Lett.* **1990,** *57* (10), 1046-1048.
170. Canham, L. T., Bioactive silicon structure fabrication through nanoetching techniques. *Adv. Mater.* **1995,** *7* (12), 1033-1037.
171. Li, X.; John, J. S.; Coffer, J. L.; Chen, Y.; Pinizzotto, R. F.; Newey, J.; Reeves, C.; Canham, L. T., Porosified silicon wafer structures impregnated with platinum anti-tumor compounds: fabrication, characterization, and diffusion studies. *Biomed. Microdevices* **2000,** *2* (4), 265-272.
172. Proot, J. P.; Delerue, C.; Allan, G., Electronic structure and optical properties of silicon crystallites: Application to porous silicon. *Appl. Phys. Lett.* **1992,** *61* (16), 1948-1950.
173. Bimbo, L. M.; Sarparanta, M.; Santos, H. A.; Airaksinen, A. J.; Mäkilä, E.; Laaksonen, T.; Peltonen, L.; Lehto, V.-P.; Hirvonen, J.; Salonen, J., Biocompatibility of thermally hydrocarbonized porous silicon nanoparticles and their biodistribution in rats. *ACS Nano* **2010,** *4* (6), 3023-3032.
174. Kovalev, D.; Gross, E.; Diener, J.; Timoshenko, V. Y.; Fujii, M., Photodegradation of porous silicon induced by photogenerated singlet oxygen molecules. *Appl. Phys. Lett.* **2004,** *85* (16), 3590-3592.
175. Low, S. P.; Williams, K. A.; Canham, L. T.; Voelcker, N. H., Generation of reactive oxygen species from porous silicon microparticles in cell culture medium. *J. Biomed. Mater. Res., Part A* **2010,** *93* (3), 1124-1131.
176. Ainslie, K.; Tao, S.; Popat, K.; Desai, T., In vitro immunogenicity of silicon-based micro-and nanostructured surfaces. *ACS Nano* **2008,** *2* (5), 1076-1084.

177. Tzur-Balter, A.; Shatsberg, Z.; Beckerman, M.; Segal, E.; Artzi, N., Mechanism of erosion of nanostructured porous silicon drug carriers in neoplastic tissues. *Nat. Commun.* **2015,** *6*, 6208.
178. Zhang, C.; Ni, D.; Liu, Y.; Yao, H.; Bu, W.; Shi, J., Magnesium silicide nanoparticles as a deoxygenation agent for cancer starvation therapy. *Nat. Nanotechnol.* **2017,** *12* (4), 378.
179. Huo, M.; Wang, L.; Chen, Y.; Shi, J., Tumor-selective catalytic nanomedicine by nanocatalyst delivery. *Nat. Commun.* **2017,** *8* (1), 357.
180. Shahbazi, M.-A.; Fernández, T. D.; Mäkilä, E. M.; Le Guével, X.; Mayorga, C.; Kaasalainen, M. H.; Salonen, J. J.; Hirvonen, J. T.; Santos, H. A., Surface chemistry dependent immunostimulative potential of porous silicon nanoplatforms. *Biomaterials* **2014,** *35* (33), 9224-9235.
181. Meraz, I. M.; Melendez, B.; Gu, J.; Wong, S. T. C.; Liu, X.; Andersson, H. A.; Serda, R. E., Activation of the inflammasome and enhanced migration of microparticle-stimulated dendritic cells to the draining lymph node. *Mol. Pharmaceutics* **2012,** *9* (7), 2049-2062.
182. Xia, X.; Mai, J.; Xu, R.; Perez, J. E. T.; Guevara, M. L.; Shen, Q.; Mu, C.; Tung, H.-Y.; Corry, D. B.; Evans, S. E., Porous silicon microparticle potentiates anti-tumor immunity by enhancing cross-presentation and inducing type I interferon response. *Cell Rep.* **2015,** *11* (6), 957-966.
183. Bachmann, M. F.; Jennings, G. T., Vaccine delivery: a matter of size, geometry, kinetics and molecular patterns. *Nat. Rev. Immunol.* **2010,** *10* (11), 787.
184. Moyano, D. F.; Goldsmith, M.; Solfiell, D. J.; Landesman-Milo, D.; Miranda, O. R.; Peer, D.; Rotello, V. M., Nanoparticle hydrophobicity dictates immune response. *J. Am. Chem. Soc.* **2012,** *134* (9), 3965-3967.
185. Reddy, S. T.; Van Der Vlies, A. J.; Simeoni, E.; Angeli, V.; Randolph, G. J.; O'Neil, C. P.; Lee, L. K.; Swartz, M. A.; Hubbell, J. A., Exploiting lymphatic transport and complement activation in nanoparticle vaccines. *Nat. Biotechnol.* **2007,** *25* (10), 1159.
186. Ge, C.; Du, J.; Zhao, L.; Wang, L.; Liu, Y.; Li, D.; Yang, Y.; Zhou, R.; Zhao, Y.; Chai, Z., Binding of blood proteins to carbon nanotubes reduces cytotoxicity. *Proc. Natl. Acad. Sci. U. S. A.* **2011**.
187. Dobrovolskaia, M. A.; McNeil, S. E., Immunological properties of engineered nanomaterials. *Nat. Nanotechnol.* **2007,** *2* (8), 469.
188. Salvati, A.; Pitek, A. S.; Monopoli, M. P.; Prapainop, K.; Bombelli, F. B.; Hristov, D. R.; Kelly, P. M.; Åberg, C.; Mahon, E.; Dawson, K. A., Transferrin-functionalized nanoparticles lose their targeting capabilities when a biomolecule corona adsorbs on the surface. *Nat. Nanotechnol.* **2013,** *8* (2), 137.
189. Tenzer, S.; Docter, D.; Kuharev, J.; Musyanovych, A.; Fetz, V.; Hecht, R.; Schlenk, F.; Fischer, D.; Kiouptsi, K.; Reinhardt, C., Rapid formation of plasma protein corona critically affects nanoparticle pathophysiology. *Nat. Nanotechnol.* **2013,** *8* (10), 772.
190. Mo, J.; Xie, Q.; Wei, W.; Zhao, J., Revealing the immune perturbation of black phosphorus nanomaterials to macrophages by understanding the protein corona. *Nat. Commun.* **2018,** *9* (1), 2480.
191. Wang, C.; Mäkilä, E.; Bonduelle, C.; Rytkonen, J.; Raula, J.; Almeida, S.; Närvänen, A.; Salonen, J.; Lecommandoux, S.; Hirvonen, J., Functionalization of alkyne-terminated thermally hydrocarbonized porous silicon nanoparticles with targeting peptides and antifouling polymers: effect on the human plasma protein adsorption. *ACS Appl. Mater. Interfaces* **2015,** *7* (3), 2006-2015.
192. Bartneck, M.; Ritz, T.; Keul, H. A.; Wambach, M.; Bornemann, J. r.; Gbureck, U.; Ehling, J.; Lammers, T.; Heymann, F.; Gassler, N., Peptide-functionalized gold nanorods increase liver injury in hepatitis. *ACS Nano* **2012,** *6* (10), 8767-8777.
193. Wang, C.-F.; Mäkilä, E. M.; Kaasalainen, M. H.; Liu, D.; Sarparanta, M. P.; Airaksinen, A. J.; Salonen, J. J.; Hirvonen, J. T.; Santos, H. A., Copper-free azide–alkyne cycloaddition of targeting peptides to porous silicon nanoparticles for intracellular drug uptake. *Biomaterials* **2014,** *35* (4), 1257-1266.

194. Wang, C.-F.; Mäkilä, E. M.; Kaasalainen, M. H.; Hagström, M. V.; Salonen, J. J.; Hirvonen, J. T.; Santos, H. A., Dual-drug delivery by porous silicon nanoparticles for improved cellular uptake, sustained release, and combination therapy. *Acta Biomater.* **2015,** *16*, 206-214.
195. Martins, J. P.; D'Auria, R.; Liu, D.; Fontana, F.; Ferreira, M. P. A.; Correia, A.; Kemell, M.; Moslova, K.; Mäkilä, E.; Salonen, J., Engineered Multifunctional Albumin‐Decorated Porous Silicon Nanoparticles for FcRn Translocation of Insulin. *Small* **2018**, 1800462.
196. Tang, Z.; He, C.; Tian, H.; Ding, J.; Hsiao, B. S.; Chu, B.; Chen, X., Polymeric nanostructured materials for biomedical applications. *Prog. Polym. Sci.* **2016,** *60*, 86-128.
197. Sionkowska, A., Current research on the blends of natural and synthetic polymers as new biomaterials. *Prog. Polym. Sci.* **2011,** *36* (9), 1254-1276.
198. Tian, H.; Tang, Z.; Zhuang, X.; Chen, X.; Jing, X., Biodegradable synthetic polymers: preparation, functionalization and biomedical application. *Prog. Polym. Sci.* **2012,** *37* (2), 237-280.
199. Miao, T.; Wang, J.; Zeng, Y.; Liu, G.; Chen, X., Polysaccharide‐Based Controlled Release Systems for Therapeutics Delivery and Tissue Engineering: From Bench to Bedside. *Adv. Sci.* **2018,** *5* (4), 1700513.
200. Pan, H.; Jiang, H.; Chen, W., The biodegradability of electrospun Dextran/PLGA scaffold in a fibroblast/macrophage co-culture. *Biomaterials* **2008,** *29* (11), 1583-1592.
201. Jeanes, A.; Wilham, C. A., Periodate oxidation of dextran. *J. Am. Chem. Soc.* **1950,** *72* (6), 2655-2657.
202. Maia, J.; Carvalho, R. A.; Coelho, J. F. J.; Simões, P. N.; Gil, M. H., Insight on the periodate oxidation of dextran and its structural vicissitudes. *Polymer* **2011,** *52* (2), 258-265.
203. Zhang, X.; Yang, Y.; Yao, J.; Shao, Z.; Chen, X., Strong collagen hydrogels by oxidized dextran modification. *ACS Sustainable Chem. Eng.* **2014,** *2* (5), 1318-1324.
204. Wu, X.; He, C.; Wu, Y.; Chen, X.; Cheng, J., Nanogel‐Incorporated Physical and Chemical Hybrid Gels for Highly Effective Chemo–Protein Combination Therapy. *Adv. Funct. Mater.* **2015,** *25* (43), 6744-6755.
205. Lu, W.; Le, X.; Zhang, J.; Huang, Y.; Chen, T., Supramolecular shape memory hydrogels: a new bridge between stimuli-responsive polymers and supramolecular chemistry. *Chem. Soc. Rev.* **2017,** *46* (5), 1284-1294.
206. Agarwal, A.; Gupta, U.; Asthana, A.; Jain, N. K., Dextran conjugated dendritic nanoconstructs as potential vectors for anti-cancer agent. *Biomaterials* **2009,** *30* (21), 3588-3596.
207. Atanase, L. I.; Desbrieres, J.; Riess, G., Micellization of synthetic and polysaccharides-based graft copolymers in aqueous media. *Prog. Polym. Sci.* **2017,** *73*, 32-60.
208. Broaders, K. E.; Grandhe, S.; Fréchet, J. M. J., A biocompatible oxidation-triggered carrier polymer with potential in therapeutics. *Journal of the American Chemical Society* **2010,** *133* (4), 756-758.
209. Daw, R.; Finkelstein, J., Lab on a chip. *Nature* **2006,** *442* (7101), 367.
210. Mark, D.; Haeberle, S.; Roth, G.; Stetten, F. V.; Zengerle, R., Microfluidic Lab-on-a-Chip Platforms: Requirements, Characteristics and Applications. *Chem. Soc. Rev.* **2010,** *39* (3), 1153-1182.
211. Beebe, D. J.; And, G. A. M.; Walker, G. M., Physics and Applications of Microfluidics in Biology. *Annu. Rev. Biomed. Eng.* **2002,** *4* (4), 261.
212. Valencia, P. M.; Farokhzad, O. C.; Karnik, R.; Langer, R., Microfluidic technologies for accelerating the clinical translation of nanoparticles. *Nat. Nanotechnol.* **2012,** *7* (10), 623.
213. Park, J.; An, K.; Hwang, Y.; Park, J.-G.; Noh, H.-J.; Kim, J.-Y.; Park, J.-H.; Hwang, N.-M.; Hyeon, T., Ultra-large-scale syntheses of monodisperse nanocrystals. *Nat. Mater.* **2004,** *3* (12), 891.
214. Discher, D. E.; Eisenberg, A., Polymer vesicles. *Science* **2002,** *297* (5583), 967-973.

215. Jana, N. R.; Gearheart, L.; Murphy, C. J., Evidence for seed-mediated nucleation in the chemical reduction of gold salts to gold nanoparticles. *Chem. Mater.* **2001,** *13* (7), 2313-2322.
216. Song, Y.; Hormes, J.; Kumar, C. S. S. R., Microfluidic synthesis of nanomaterials. *Small* **2008,** *4* (6), 698-711.
217. Johnson, B. K.; Prud'homme, R. K., Mechanism for rapid self-assembly of block copolymer nanoparticles. *Phys. Rev. Lett.* **2003,** *91* (11), 118302.
218. Karnik, R.; Gu, F.; Basto, P.; Cannizzaro, C.; Dean, L.; Kyei-Manu, W.; Langer, R.; Farokhzad, O. C., Microfluidic platform for controlled synthesis of polymeric nanoparticles. *Nano Lett.* **2008,** *8* (9), 2906-2912.
219. Squires, T. M.; Quake, S. R., Microfluidics: Fluid physics at the nanoliter scale. *Rev. Mod. Phys.* **2005,** *77* (3), 977.
220. Atencia, J.; Beebe, D. J., Controlled microfluidic interfaces. *Nature* **2004,** *437* (7059), 648.
221. Martin, J. D.; Hudson, S. D., Mass transfer and interfacial properties in two-phase microchannel flows. *New J. Phys.* **2009,** *11* (11), 115005.
222. Prengle, H. W.; Palm, G., Thermodynamics of Solutions. *Ind. Eng. Chem* **1957,** *49* (10), 1769-1774.
223. Gravesen, P.; Branebjerg, J.; Jensen, O. S., Microfluidics-a review. *J. Micromech. Microeng.* **1993,** *3* (4), 168.
224. Peng, X. F.; Peterson, G. P.; Wang, B. X., Frictional flow characteristics of water flowing through rectangular microchannels. *Exp. Heat Transfer* **1994,** *7* (4), 249-264.
225. Mala, G. M.; Li, D., Flow characteristics of water in microtubes. *Int. J. Heat Fluid Flow* **1999,** *20* (2), 142-148.
226. Sharp, K. V.; Adrian, R. J., Transition from laminar to turbulent flow in liquid filled microtubes. *Exp. Fluids* **2004,** *36* (5), 741-747.
227. Lim, J.-M.; Swami, A.; Gilson, L. M.; Chopra, S.; Choi, S.; Wu, J.; Langer, R.; Karnik, R.; Farokhzad, O. C., Ultra-high throughput synthesis of nanoparticles with homogeneous size distribution using a coaxial turbulent jet mixer. *ACS Nano* **2014,** *8* (6), 6056-6065.
228. Liu, D.; Cito, S.; Zhang, Y.; Wang, C. F.; Sikanen, T. M.; Santos, H. A., A versatile and robust microfluidic platform toward high throughput synthesis of homogeneous nanoparticles with tunable properties. *Adv. Mater.* **2015,** *27* (14), 2298-2304.
229. Jahn, A.; Stavis, S. M.; Hong, J. S.; Vreeland, W. N.; DeVoe, D. L.; Gaitan, M., Microfluidic mixing and the formation of nanoscale lipid vesicles. *ACS Nano* **2010,** *4* (4), 2077-2087.
230. Kim, Y.; Fay, F.; Cormode, D. P.; Sanchez-Gaytan, B. L.; Tang, J.; Hennessy, E. J.; Ma, M.; Moore, K.; Farokhzad, O. C.; Fisher, E. A., Single step reconstitution of multifunctional high-density lipoprotein-derived nanomaterials using microfluidics. *ACS Nano* **2013,** *7* (11), 9975-9983.
231. Stroock, A. D.; Dertinger, S. K. W.; Ajdari, A.; Mezić, I.; Stone, H. A.; Whitesides, G. M., Chaotic mixer for microchannels. *Science* **2002,** *295* (5555), 647-651.
232. Feng, Q.; Sun, J.; Jiang, X., Microfluidics-mediated assembly of functional nanoparticles for cancer-related pharmaceutical applications. *Nanoscale* **2016,** *8* (25), 12430-12443.
233. Lasic, D. D., *Liposomes: from physics to applications*. Elsevier Science Ltd: 1993.
234. Patil, Y. P.; Jadhav, S., Novel methods for liposome preparation. *Chem. Phys. Lipids* **2014,** *177*, 8-18.
235. Kim, H.; Sung, J.; Chang, Y.; Alfeche, A.; Leal, C., Microfluidics Synthesis of Gene Silencing Cubosomes. *ACS Nano* **2018**.
236. Hong, C.-C.; Choi, J.-W.; Ahn, C. H., A novel in-plane passive microfluidic mixer with modified Tesla structures. *Lab Chip* **2004,** *4* (2), 109-113.
237. Feng, Q.; Zhang, L.; Liu, C.; Li, X.; Hu, G.; Sun, J.; Jiang, X., Microfluidic based high throughput synthesis of lipid-polymer hybrid nanoparticles with tunable diameters. *Biomicrofluidics* **2015,** *9* (5), 052604.

238. Chen, D.; Love, K. T.; Chen, Y.; Eltoukhy, A. A.; Kastrup, C.; Sahay, G.; Jeon, A.; Dong, Y.; Whitehead, K. A.; Anderson, D. G., Rapid discovery of potent siRNA-containing lipid nanoparticles enabled by controlled microfluidic formulation. *J. Am. Chem. Soc.* **2012,** *134* (16), 6948-6951.
239. Abate, A. R.; Lee, D.; Do, T.; Holtze, C.; Weitz, D. A., Glass coating for PDMS microfluidic channels by sol–gel methods. *Lab Chip* **2008,** *8* (4), 516-518.
240. Chaudhuri, R. G.; Paria, S., Core/Shell Nanoparticles: Classes, Properties, Synthesis Mechanisms, Characterization, and Applications. *Chem. Rev.* **2012,** *112* (4), 2373.
241. Wang, Y.; Gao, S.; Ye, W. H.; Yoon, H. S.; Yang, Y. Y., Co-delivery of drugs and DNA from cationic core-shell nanoparticles self-assembled from a biodegradable copolymer. *Nat. Mater.* **2006,** *5* (10), 791-6.
242. Joo, J.; Kwon, E. J.; Kang, J.; Skalak, M.; Anglin, E. J.; Mann, A. P.; Ruoslahti, E.; Bhatia, S. N.; Sailor, M. J., Porous silicon-graphene oxide core-shell nanoparticles for targeted delivery of siRNA to the injured brain. *Nanoscale Horiz.* **2016,** *1* (5), 407.
243. Valencia, P. M.; Basto, P. A.; Zhang, L.; Rhee, M.; Langer, R.; Farokhzad, O. C.; Karnik, R., Single-step assembly of homogenous lipid− polymeric and lipid− quantum dot nanoparticles enabled by microfluidic rapid mixing. *ACS Nano* **2010,** *4* (3), 1671-1679.
244. Sun, J.; Zhang, L.; Wang, J.; Feng, Q.; Liu, D.; Yin, Q.; Xu, D.; Wei, Y.; Ding, B.; Shi, X., Tunable rigidity of (polymeric core)–(lipid shell) nanoparticles for regulated cellular uptake. *Adv. Mater.* **2015,** *27* (8), 1402-1407.
245. Abou‐Hassan, A.; Bazzi, R.; Cabuil, V., Multistep Continuous‐Flow Microsynthesis of Magnetic and Fluorescent γ‐Fe2O3@ SiO2 Core/Shell Nanoparticles. *Angew. Chem.* **2009,** *121* (39), 7316-7319.
246. Liu, D.; Zhang, H.; Cito, S.; Fan, J.; Mäkilä, E. M.; Salonen, J. J.; Hirvonen, J.; Sikanen, T. M.; Weitz, D. A.; Santos, H. A., Core/Shell Nanocomposites Produced by Superfast Sequential Microfluidic Nanoprecipitation. *Nano Lett.* **2017,** *17* (2), 606.
247. Pagels, R. F.; Edelstein, J.; Tang, C.; Prud'homme, R. K., Controlling and Predicting Nanoparticle Formation by Block Copolymer Directed Rapid Precipitations. *Nano Lett.* **2018,** *18* (2), 1139-1144.
248. Zhang, H.; Liu, D.; Wang, L.; Liu, Z.; Wu, R.; Janoniene, A.; Ma, M.; Pan, G.; Baranauskiene, L.; Zhang, L., Microfluidic Encapsulation of Prickly Zinc‐Doped Copper Oxide Nanoparticles with VD1142 Modified Spermine Acetalated Dextran for Efficient Cancer Therapy. *Adv. Healthcare Mater.* **2017,** *6* (11), 1601406.
249. Gindy, M. E.; Panagiotopoulos, A. Z.; Prud'Homme, R. K., Composite block copolymer stabilized nanoparticles: simultaneous encapsulation of organic actives and inorganic nanostructures. *Langmuir the Acs Journal of Surfaces & Colloids* **2008,** *24* (1), 83.
250. Jalkanen, T.; Mäkilä, E.; Sakka, T.; Salonen, J.; Ogata, Y. H., Thermally promoted addition of undecylenic acid on thermally hydrocarbonized porous silicon optical reflectors. *Nanoscale Res. Lett.* **2012,** *7* (1), 311.
251. Shrestha, N.; Araújo, F.; Shahbazi, M. A.; Mäkilä, E.; Gomes, M. J.; Herranz‐Blanco, B.; Lindgren, R.; Granroth, S.; Kukk, E.; Salonen, J., Thiolation and Cell‐Penetrating Peptide Surface Functionalization of Porous Silicon Nanoparticles for Oral Delivery of Insulin. *Adv. Funct. Mater.* **2016,** *26* (20), 3405-3416.
252. Salonen, J.; Laine, E.; Niinistö, L., Thermal carbonization of porous silicon surface by acetylene. *J. Appl. Phys.* **2002,** *91* (1), 456-461.
253. Dudutienė, V.; Zubrienė, A.; Smirnov, A.; Timm, D. D.; Smirnovienė, J.; Kazokaitė, J.; Michailovienė, V.; Zakšauskas, A.; Manakova, E.; Gražulis, S., Functionalization of fluorinated benzenesulfonamides and their inhibitory properties toward carbonic anhydrases. *ChemMedChem* **2015,** *10* (4), 662-687.
254. Brunauer, S.; Copeland, L. In *Physical adsorption of gases and vapors on solids*, 1963; ASTM International.
255. Kong, F.; Zhang, X.; Zhang, H.; Qu, X.; Chen, D.; Servos, M.; Mäkilä, E.; Salonen, J.; Santos, H. A.; Hai, M., Inhibition of Multidrug Resistance of Cancer Cells by Co‐Delivery of DNA Nanostructures and Drugs Using Porous Silicon Nanoparticles@ Giant Liposomes. *Adv. Funct. Mater.* **2015,** *25* (22), 3330-3340.

256. Williams, J. W.; Morrison, J. F., The kinetics of reversible tight-binding inhibition. In *Methods Enzymol.*, Elsevier: 1979; Vol. 63, pp 437-467.
257. Keshishian, H.; Burgess, M. W.; Specht, H.; Wallace, L.; Clauser, K. R.; Gillette, M. A.; Carr, S. A., Quantitative, multiplexed workflow for deep analysis of human blood plasma and biomarker discovery by mass spectrometry. *Nat. Protoc.* **2017,** *12* (8), 1683.
258. Liu, Z.; Liu, S.; Wang, X.; Li, P.; He, Y., A novel quantum dots-based OFF–ON fluorescent biosensor for highly selective and sensitive detection of double-strand DNA. *Sensor. Actuat. B-Chem.* **2013,** *176*, 1147-1153.
259. She, J.; Mo, L. E.; Kang, T. B.; Song ZhJ, L. N. C., Preparation of water-soluble quercetin derivatives and their biological activities. *Chin. J. Med. Chem.* **1998,** *8* (4), 287-289.
260. Fan, F.; He, Z.; Kong, L.-L.; Chen, Q.; Yuan, Q.; Zhang, S.; Ye, J.; Liu, H.; Sun, X.; Geng, J., Pharmacological targeting of kinases MST1 and MST2 augments tissue repair and regeneration. *Sci. Transl. Med.* **2016,** *8* (352), 352ra108-352ra108.
261. Friess, W.; Lee, G.; Groves, M. J., Insoluble collagen matrices for prolonged delivery of proteins. *Pharm. Dev. Technol.* **1996,** *1* (2), 185-193.
262. Lee, R. J.; Springer, M. L.; Blanco-Bose, W. E.; Shaw, R.; Ursell, P. C.; Blau, H. M., VEGF gene delivery to myocardium: deleterious effects of unregulated expression. *Circulation* **2000,** *102* (8), 898-901.
263. Thapa, B. R.; Walia, A., Liver function tests and their interpretation. *Indian J. Pediatr.* **2007,** *74* (7), 663-671.
264. Wu, E. C.; Park, J.-H.; Park, J.; Segal, E.; Cunin, F.; Sailor, M. J., Oxidation-triggered release of fluorescent molecules or drugs from mesoporous Si microparticles. *ACS Nano* **2008,** *2* (11), 2401-2409.
265. Wang, L.; Li, J.; Pan, J.; Jiang, X.; Ji, Y.; Li, Y.; Qu, Y.; Zhao, Y.; Wu, X.; Chen, C., Revealing the binding structure of the protein corona on gold nanorods using synchrotron radiation-based techniques: understanding the reduced damage in cell membranes. *J. Am. Chem. Soc.* **2013,** *135* (46), 17359-17368.
266. Corbo, C.; Molinaro, R.; Parodi, A.; Toledano Furman, N. E.; Salvatore, F.; Tasciotti, E., The impact of nanoparticle protein corona on cytotoxicity, immunotoxicity and target drug delivery. *Nanomedicine* **2016,** *11* (1), 81-100.
267. Lohmann, N.; Schirmer, L.; Atallah, P.; Wandel, E.; Ferrer, R. A.; Werner, C.; Simon, J. C.; Franz, S.; Freudenberg, U., Glycosaminoglycan-based hydrogels capture inflammatory chemokines and rescue defective wound healing in mice. *Sci. Transl. Med.* **2017,** *9* (386), eaai9044.
268. Li, S.; Nih, L. R.; Bachman, H.; Fei, P.; Li, Y.; Nam, E.; Dimatteo, R.; Carmichael, S. T.; Barker, T. H.; Segura, T., Hydrogels with precisely controlled integrin activation dictate vascular patterning and permeability. *Nat. Mater.* **2017,** *16* (9), 953.
269. Deng, Z. J.; Liang, M.; Monteiro, M.; Toth, I.; Minchin, R. F., Nanoparticle-induced unfolding of fibrinogen promotes Mac-1 receptor activation and inflammation. *Nat. Nanotechnol.* **2011,** *6* (1), 39.
270. Qin, Z.; Mustafa, R.; Yu, C.; Yuka, S.; Tolga, S.; Wolfgang, J.; Karim, B.; Kiyoshi, I.; Hauser, C. J., Circulating mitochondrial DAMPs cause inflammatory responses to injury. *Nature* **2010,** *464* (7285), 104-107.
271. Krysko, D. V.; Patrizia, A.; Olga, K.; Garg, A. D.; Claus, B.; Lambrecht, B. N.; Peter, V., Emerging role of damage-associated molecular patterns derived from mitochondria in inflammation. *Trends Immunol.* **2011,** *32* (4), 157-164.
272. Takafumi, O.; Shungo, H.; Osamu, Y.; Manabu, T.; Toshihiro, T.; Takahito, T.; Jota, O.; Tomokazu, M.; Hiroyuki, N.; Kazuhiko, N., Mitochondrial DNA that escapes from autophagy causes inflammation and heart failure. *Nature* **2012,** *485* (7397), 251-5.
273. Zou, H.; Henzel, W. J.; Liu, X.; Lutschg, A.; Wang, X., Apaf-1, a Human Protein Homologous to C. elegans CED-4, Participates in Cytochrome c–Dependent Activation of Caspase-3. *Cell* **1997,** *90* (3), 405-13.